博士学位論文

Two-step Energy Gap Formation Mechanism of Topological Kondo Insulator $\mathrm{Yb_{1-x}R_xB_{12}}$

(トポロジカル近藤絶縁体 $\mathrm{Yb_{1-x}R_xB_{12}}$ における２段エネルギーギャップ形成機構)

令和04年03月

茨城大学大学院理工学研究科
量子線科学専攻

19ND107X
松浦 航

Abstract

Two-step Energy Gap Formation Mechanism of Topological Kondo Insulator $Yb_{1-x}R_xB_{12}$

Dept. of Quantum Beam Sci., Grad. Sch. of Sci. & Eng., Ibaraki Univ.
19ND107X
Wataru Matsuhra

YbB_{12}, which has attracted attention as an unconventional strongly correlated insulator, has a two-step energy gap structure (ΔE_1, ΔE_2) with an in-gap state. These characteristics cannot be explained by a simple c-f hybridization gap model. To clarify the difference between the ground states in the Kondo insulator phase and in the dilute Kondo metal, I have studied the nonmagnetic ion substitution effect on electrical conductivity σ, magnetic susceptibility χ, and specific heat divided by temperature $C\,/\,T$ measurements of the Kondo insulator $Yb_{1-x}R_xB_{12}$ ($R = Ca^{2+}$, Lu^{3+}, Y^{3+}, and Zr^{4+}). It is found that there are a sensitive substitution effect in the ΔE_2-dominant temperature region ($T < 15$ K) and an insensitive one in the ΔE_1-dominant region (15 K $< T <$ 100 K). Here, on the basis of Schlottmann's model I have proposed a novel density of states (DOS) model constructed from the x dependences of σ, χ, and $C\,/\,T$ with a boundary of $x_0 \simeq 0.1$. I conclude that our three-band DOS model can also be applied to YbB_{12} by taking into account a small amount of defects or disorder.

Contents

1 Introduction

Rare-earth compounds with non-closed $4f$ electron orbitals in the inner shell can exhibit strong magnetization due to the magnetic moment of the localized $4f$ electrons. However, the localization of the $4f$ electrons is no longer stable due to the interaction with conduction electrons. Rare-earth compounds exhibit a variety of interesting physical phenomena due to the localization and itinerancy of the $4f$ electrons. In this chapter, I will introduce the model and experimental results of the c-f interaction, an important interaction in rare-earth compounds that leads to the Kondo effect and Rudermann-Kittel-Kasuya-Yosida (RKKY) interaction. In addition, I present experimental results and theories of $\mathrm{SmB_6}$ and $\mathrm{YbB_{12}}$, which are unique materials in Kondo lattice and representative of Kondo insulators. Topological insulators and unconventional quantum oscillations, which are important topics related to Kondo insulators, will be introduced.

1.1 Anderson impurity Hamiltonian and c-f interaction

In the field of modern solid state physics, the most important issue on physical properties is understanding contribution of complex many-body effects. In a group of materials containing d- and f-electrons, the interaction between the magnetic moment of ions and electrons contributes to the various physical properties. In compounds including $3d$ transition metal, $3d$ orbitals form bonding orbitals with surrounding ligands and exhibit only spin angular momentum. The interaction between the spin momentum and conduction electrons (s-d interaction) leads to various phenomena such as Kondo effect, which will be discussed later.

On the other hand, the $4f$ orbitals in rare-earth ions exhibit both orbital and spin angular momentum because $4f$ electrons are located in the inner shell and have small overlap of wave functions with conduction electrons in crystal. In this case, total angular momentum J of $4f$ electrons is a good quantum number due to strong LS coupling. The interaction between the magnetic moment and conduction electron is called c-f interaction. Hamiltonian of the Anderson impurity model with s-d (c-f) interaction is

$$\begin{aligned}\mathcal{H}_{AM} = \Sigma_k \Sigma_\sigma \epsilon_{k\sigma} c_{k\sigma}^\dagger c_{k\sigma} + \Sigma_\sigma E_f f_\sigma^\dagger f_\sigma + U n_{f\uparrow} n_{f\downarrow} \\ + V_{cf} \Sigma_{k\sigma} \left(c_{k\sigma}^\dagger f_{k\sigma} + f_{k\sigma}^\dagger c_{k\sigma} \right)\end{aligned} \tag{1}$$

where the first term and second term are the energy level of conduction electron and f-electron, respectively[1, 2]. Third term is Coulomb energy between f-electrons. Fourth term is exchange interaction between f-electron and conduction electron. For simplicity, ignore orbital degrees of freedom of f-electrons. Here, based on Anderson's method, the Hartree-Fock approximation (molecular field approximation) is applied to the third term as follows:

$$U n_{f\uparrow} n_{f\downarrow} = U[< n_{f\uparrow} > + (n_{f\uparrow} - < n_{f\uparrow} >)][< n_{f\downarrow} > + (n_{f\downarrow} - < n_{f\downarrow} >)] \tag{2}$$

In this mean-field approximation, the interaction elevate the f-level by U $<$ n$_f$ $>$ (Hartree-Fock shifted). In this case, the Hamiltonian is as follows:

$$\mathcal{H}_{MF} = \Sigma_k \Sigma_\sigma \epsilon_{k\sigma} c_{k\sigma}^\dagger c_{k\sigma} + \Sigma_\sigma E_{f\sigma} f_\sigma^\dagger f_\sigma + V_{cf} \Sigma_{k\sigma} \left(c_{k\sigma}^\dagger f_{k\sigma} + f_{k\sigma}^\dagger c_{k\sigma} \right) \tag{3}$$

In a model where the degree of freedom of f-orbitals are restricted to spin, the effective Hamiltonian can be obtained by a second-order perturbation on hybridization as follow.

$$\mathcal{H} = \mathcal{H}_{imp} + \mathcal{H}_{cf}$$
$$\mathcal{H}_{imp} = - < |V|^2 > [\frac{1}{E_f + U - \epsilon_F} - \frac{1}{2} n_f \left(\frac{1}{E_f + U - \epsilon_F} + \frac{1}{\epsilon_F - E_f} \right)] \times \frac{1}{N_0} \Sigma_{kk'} c^{\dagger}_{k'\sigma} c_{k\sigma}$$
$$\mathcal{H}_{cf} = J_{cf} \frac{1}{2N_0} \Sigma_{kk'} [\left(c^{\dagger}_{k'\uparrow} c_{k\uparrow} - c^{\dagger}_{k'\downarrow} c_{k\downarrow} \right) S_z + c^{\dagger}_{k'\downarrow} c_{k\uparrow} S_+ + c^{\dagger}_{k'\uparrow} c_{k\downarrow} S_-] \tag{4}$$

where ϵ_{F} is Fermi level. The magnitude of the *c*-*f* interaction is given by

$$J_{cf} = 2 < |V_{cf}|^2 > \left(\frac{1}{E_f + U - \epsilon_F} + \frac{1}{\epsilon_F - E_f} \right) \tag{5}$$

The effective Hamiltonian of the *c*-*f* interaction in Eq. (4) is also starting point for the scaling law of Kondo effect, which will be discussed in next section. In the following, I will introduce two important interactions derived from this *c*-*f* interaction.

1.2 Impurity Kondo effect

Various interesting physical properties originating from the Kondo effect have given rise to important topics in strongly correlated electron systems. The Kondo effect, in which the interaction between magnetic moments and conduction electrons causes an increase in electrical resistivity with decreasing temperature, was found in nonmagnetic metals containing small amounts of magnetic $3d$-transition metal impurities. The first theoretical analysis of this effect was performed by Kondo in 1964 [3]. Based on the *s*-*d* interaction model for dilute magnetic alloys, scattering probability of conduction electrons was calculated in the second Born approximation. As a result, a singular term involving $\log T$ dependent on density of state at Fermi level $D_c(\epsilon_{\mathrm{F}})$ was obtained as follows.

$$\rho(T) = \rho_B (1 + 2J_{cf} D_c(\epsilon_F) log \frac{W}{k_B T}) \tag{6}$$

where W is the bandwidth and k_{B} is the Boltzmann factor. The interaction J_{cf} between magnetic moments of conduction electrons and magnetic impurity is positive in the ferromagnetic case, and negative in the antiferromagnetic case. When J_{cf} is negative, this electrical resistivity increases with decreasing temperature[3], as shown in Fig. 1.

$$k_{\mathrm{B}} T_{\mathrm{K}} = W \exp(-\frac{1}{J_{cf} D_c(\epsilon_{\mathrm{F}})}) \tag{7}$$

When T is less than the temperature T_{K} as defined in equation (7), the second term in equation (6) eliminating factor 2, becomes equal to the first term. The electrical resistivity including higher order terms diverges to infinity below T_{K}, because the simple perturbation calculation breaks down. Similarly, anomaly in calculated magnetic susceptibility χ below T_{K} appears as divergence to -∞. Yoshida proposed that the ground state at absolute zero is a non-magnetic singlet state called the Kondo singlet[4]. In the 1970s, the physics below T_{K} was explained by Anderson's scaling theory[5] and Wilson's numerical renormalization group theory[6]. Following Anderson's poor man's scaling theory[5] and considering the anisotropy of J_{cf}, equation (4) can be written as follows

$$\mathcal{H}_{cf} = \frac{1}{2N_0} \Sigma_{kk'} [J_z \left(c^{\dagger}_{k'\uparrow} c_{k\uparrow} - c^{\dagger}_{k'\downarrow} c_{k\downarrow} \right) S_z + J_{\perp} \left(c^{\dagger}_{k'\downarrow} c_{k\uparrow} S_+ + c^{\dagger}_{k'\uparrow} c_{k\downarrow} S_- \right)]. \tag{8}$$

Consider the bandwidth W of quasiparticle state. In the low temperature state, higher energy processes are eliminated and W becomes smaller. In the scaling theory, magnitude of the interaction (J_z and $J_{\perp}$) are a function of W so that Hamiltonian remains invariant at low temperatures. In the case where the interaction is antiferromagnetic, it is found that the coupling constant is infinitely strong in limit of $T \to 0$ while it is weak at room temperature. This indicates a continuous connection between the Kondo singlet ground state at low temperature and the free spin state at room temperature.

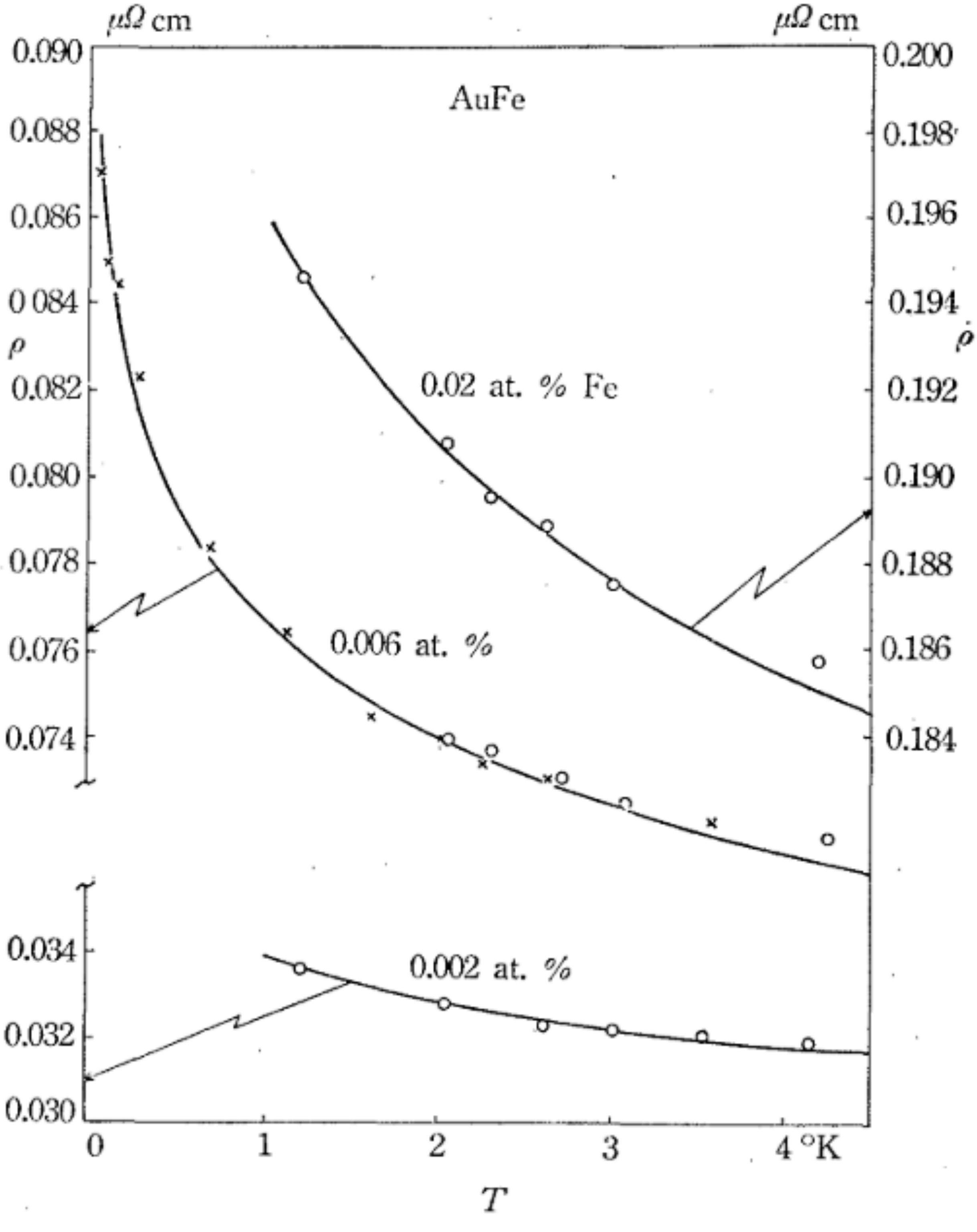

Fig.1: Comparison of experimental and theoretical ρ-T curves for diluted AuFe alloys from [3].

1.3 RKKY interaction

When the concentration of rare-earth elements increases, magnetic ordering generally occurs with Rudermann-Kittel-Kasuya-Yosida (RKKY) interaction in materials containing $4f$ rare-earth metals, in which conduction electrons align the direction of the $4f$ magnetic moments of successive rare-earth ions parallel or anti-parallel. In considering the RKKY interaction, consider internal field mediated by conduction electrons, since there is no direct interaction between localized spins in AM. When local magnetic field $-J_{cf} < S_i >$ is applied to site i for conduction electrons, the polarization of s_j is as follows

$$< s_j^{\alpha} >= -J_{cf} \Sigma_{\beta=x,y,z} \chi^{\alpha,\beta}(j,i) < S_i^{\beta} > . \tag{9}$$

Furthermore, assuming that there is a localized spin at site j, the energy of the spin when it points in a certain direction is

$$-J_{cf}^2 \Sigma_{\alpha,\beta} < S_j^{\alpha} > \chi^{\alpha,\beta}(j,i) < S_i^{\beta} > . \tag{10}$$

Summing this for each lattice point yields the following effective Hamiltonian.

$$\mathcal{H}_{RKKY} = -J_{cf}^2 \Sigma_{<i,j>} \Sigma_{\alpha,\beta} < S_j^{\alpha} > \chi^{\alpha,\beta}(j,i) < S_i^{\beta} > \tag{11}$$

The magnitude of this interaction oscillates and decreases with the distance between the two spins. This oscillation is called the Friedel oscillation.

$$F(2k_F r) \sim \frac{-2k_F r \cos(2k_F r) + \sin(2k_F r)}{(2k_F r)^4} \tag{12}$$

Since the magnitude of the interaction is proportional to the Friedel oscillation, the magnetic order temperature (and its characteristic energy scale) is also given by

$$k_B T_{RKKY} \sim |J_{cf}|^2 D(\epsilon_F) F(2k_F r) sS. \tag{13}$$

The direction of spin acts in direction of decreasing energy and thus changes according to sign of Friedel oscillation. As mentioned above, both the Kondo effect and the RKKY interaction have an energy scale that depends on $J_{cf}D_c(\epsilon_{\rm F})$, but difference is that Kondo effect is an on-site interaction and RKKY interaction is an inter-site interaction.

1.4 Kondo lattice

A system with a high concentration of magnetic impurities, especially with magnetic ions at each lattice point, is called a Kondo lattice. In Kondo lattice, magnetic ions also have translational symmetry, allowing band-like picture. The following is Hamiltonian of the periodic Anderson model(PAM), which is an extension of the Anderson impurity model.

$$\mathcal{H}_{PAM} = \Sigma_k \Sigma_\sigma \epsilon_{k\sigma} c^\dagger_{k\sigma} c_{k\sigma} + \Sigma_{i\sigma} E_f f^\dagger_{i\sigma} f_{i\sigma} + V_{cf} \Sigma_{k\sigma} \left(c^\dagger_{k\sigma} f_{k\sigma} + f^\dagger_{k\sigma} c_{k\sigma} \right) + U \Sigma_{ik} n_{if\uparrow} n_{if\downarrow} \tag{14}$$

A similar translation for the Anderson impurity model can be used to derive the Kondo lattice model(KLM) from the PAM.

$$\mathcal{H}_{KLM} = \Sigma_k \Sigma_\sigma \epsilon_{k\sigma} c^\dagger_{k\sigma} c_{k\sigma} + \Sigma_i (2J_z S^z_{f,i} s^z_{c,i} + J_\perp (S^+_{f,i} s^-_{c,i} + S^-_{f,i} s^+_{c,i})) \tag{15}$$

The two important effects in the Kondo lattice, which will be introduced in following sections, both originate from interaction of second term of this Hamiltonian.

Nevertheless, Kondo lattices, especially those containing Ce, Yb, and Sm, tend to show a similar Kondo effect without magnetic ordering even at lower temperatures, as shown in Fig. 2. While the RKKY interaction aligns spins of magnetic ions, Kondo effect is an interaction in which spins of conduction electrons shield one of magnetic ions, as illustrated in Fig. 3. Owing to this interaction, conduction electrons behave as quasiparticles with heavy effective masses, and these nonmagnetic ground states are called heavy electrons or Fermi liquids in a Kondo lattice. In these compounds, the effective mass of a conduction electron increases by up to 100–1000 times, resulting in various interesting physical phenomena (unconventional superconductivity[8, 9], multipole ordering[10], quantum critical phenomena[11], and valence fluctuation[12]). The Kondo effect and the RKKY interaction originate from interaction between conduction electrons and magnetic moments, but these ground states differ between the nonmagnetic Kondo singlet and magnetic order. A phase diagram (Fig. 4) with the characteristic temperatures of each interaction, T_{K} and T_{RKKY}, was presented by Doniach[13]. When the f-electron level and Fermi level (ϵ_{F}) become close to each other, these behaviors shift to valence fluctuation in the Kondo lattice. For $T > T_{\mathrm{K}}$, a nonmagnetic Kondo insulator should be on the right side of the Doniach phase diagram from the magnetic aspect. However, Kondo insulators below T_{K} behave like insulator, unlike Fermi liquids and heavy fermion systems, and cannot be explained by the phase diagram for metal, so they must be treated differently.

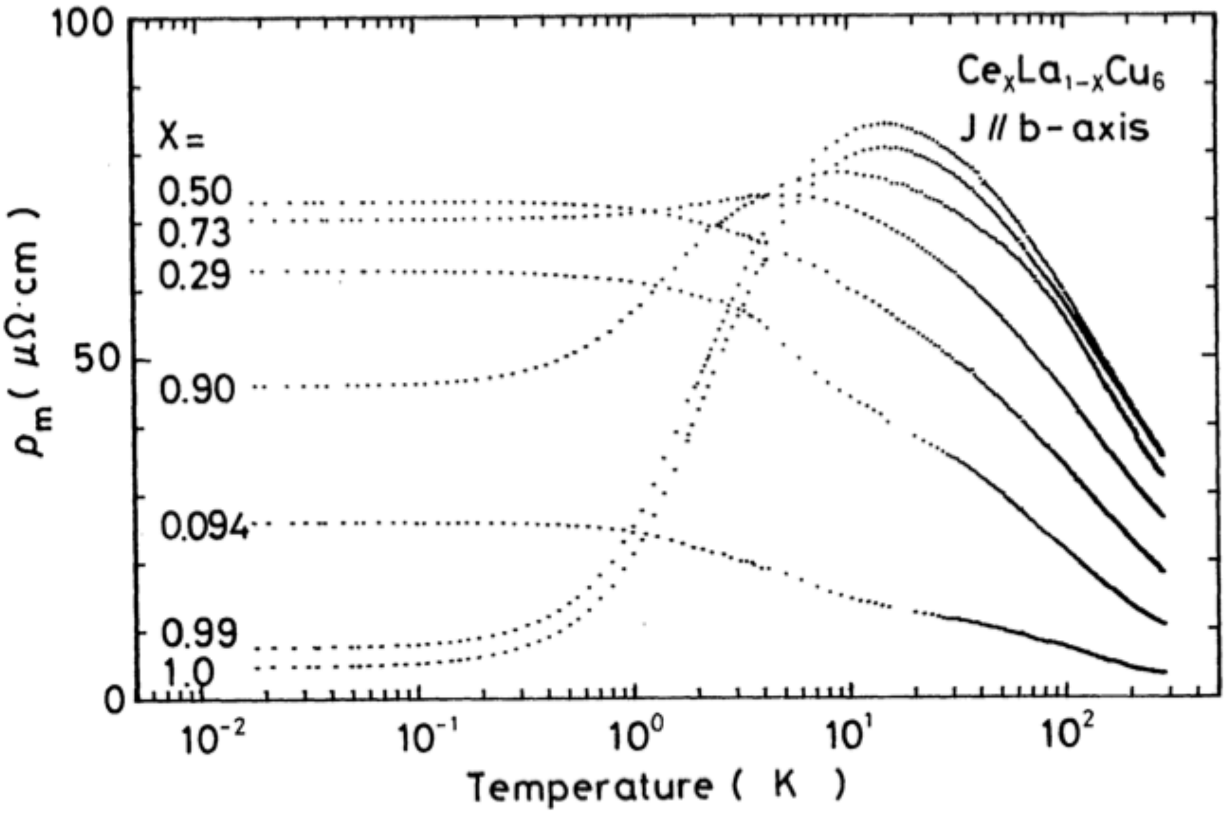

Fig.2: ρ-T curves of $(\mathrm{La,Ce})\mathrm{Cu_6}$ from Ref. [7]

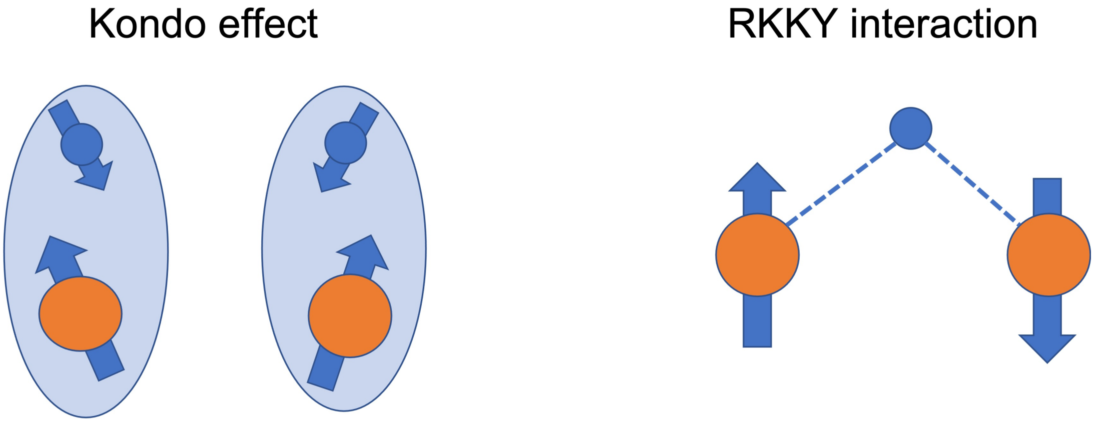

Fig.3: Schematic of RKKY interaction and Kondo effect. While Kondo effect screens magnetic moment on-site, RKKY interaction aligns magnetic moments of neighboring lattice points.

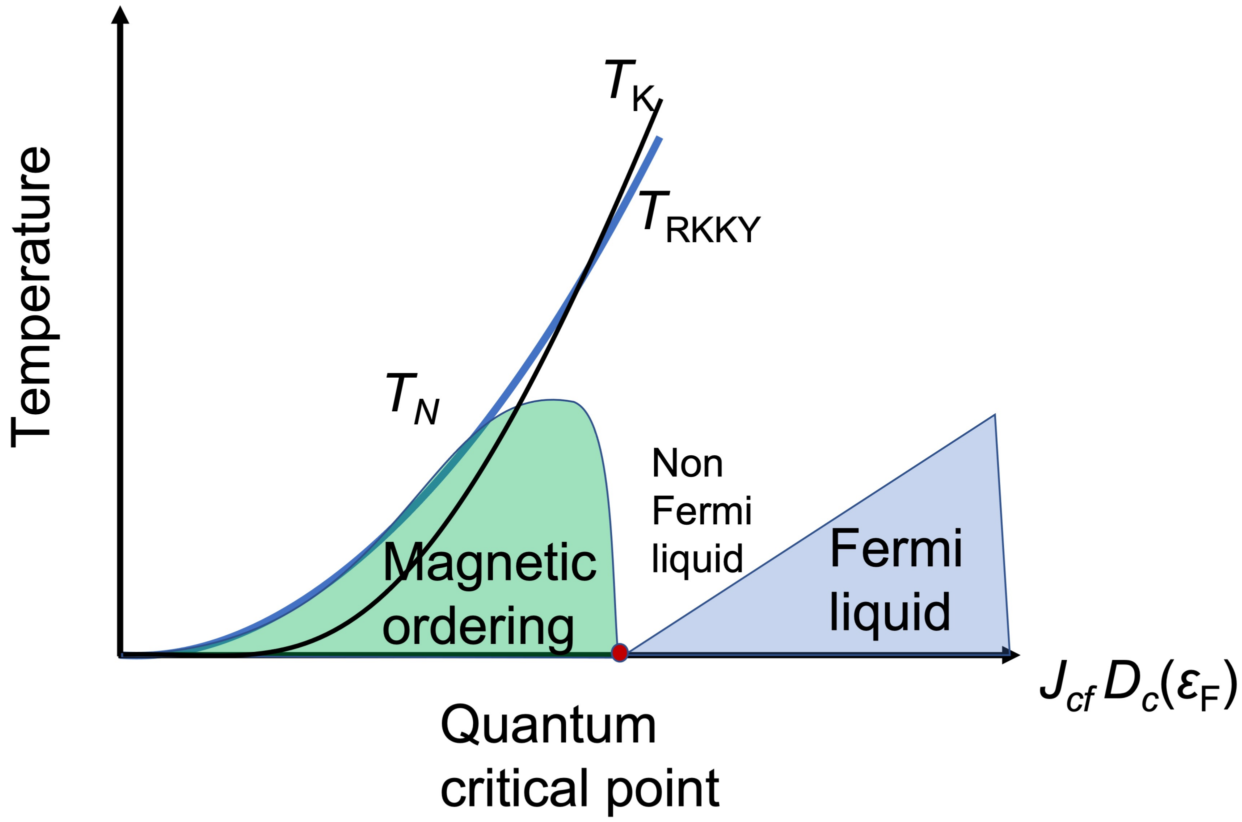

Fig.4: Doniach phase diagram[13]. Kondo effect and RKKY interaction are placed on this diagram depending on $J_{cf}D_c(\epsilon_F)$.

1.5 Kondo insulator YbB_{12}

In 1969 SmB_6 was reported as a valence fluctuating semiconductor[14]. Furthermore YbB_{12} was also found as an anomalous Kondo lattice (Kondo temperature: $T_K = 250$ K) [15] exhibiting both valence fluctuation and semiconducting behavior in 1983. In YbB_{12} and SmB_6, Kondo effect was found to be dominant in both magnetism and electrical transport, and then the name of Kondo insulator (KI) has been given by various research for YbB_{12} and SmB_6.

The magnetic susceptibility χ of YbB_{12} follows a Curie–Weiss law derived from the localized $4f$ moment of the Yb ion ($T > T_K$). Nevertheless, the magnetic moment below T_K is screened by the Kondo effect and χ decreases with the opening of an energy gap below 100 K[16]. Thus,

χ of YbB_{12} shows a broad maximum at the peak temperature (T_χ^{max}= 80 K). The valence of the Yb ion in YbB_{12} was evaluated to be about 2.9 from X-ray photoemission spectroscopy[17] and X-ray L_{III} absorption measurements[15], as shown in Fig. 6 and Fig. 7, respectively. Its crystal structure is Fm$\overline{3}$m with RB_{12}-type structure and lattice constant of 7.469 Å as shown in Fig. 5 .

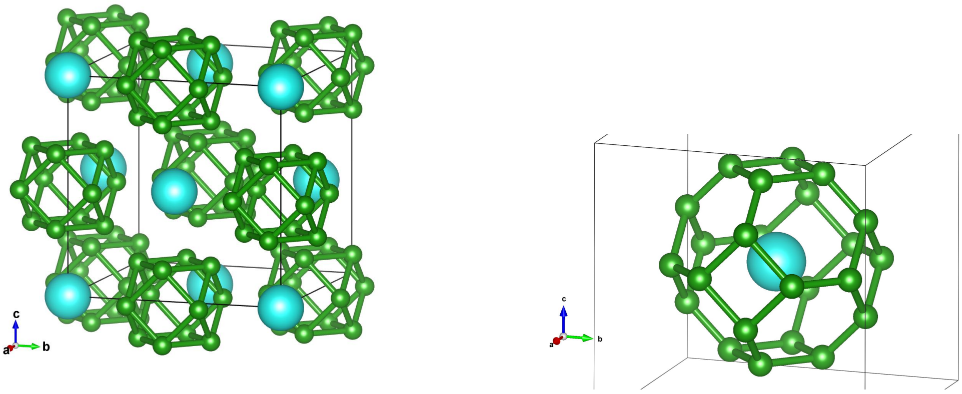

(a) **(b)**

Fig.5: (a) Crystal structure of YbB_{12}. The lattice constant is 7.469 Å, and Yb and B form a NaCl structure. (b) B cage with Yb ions.

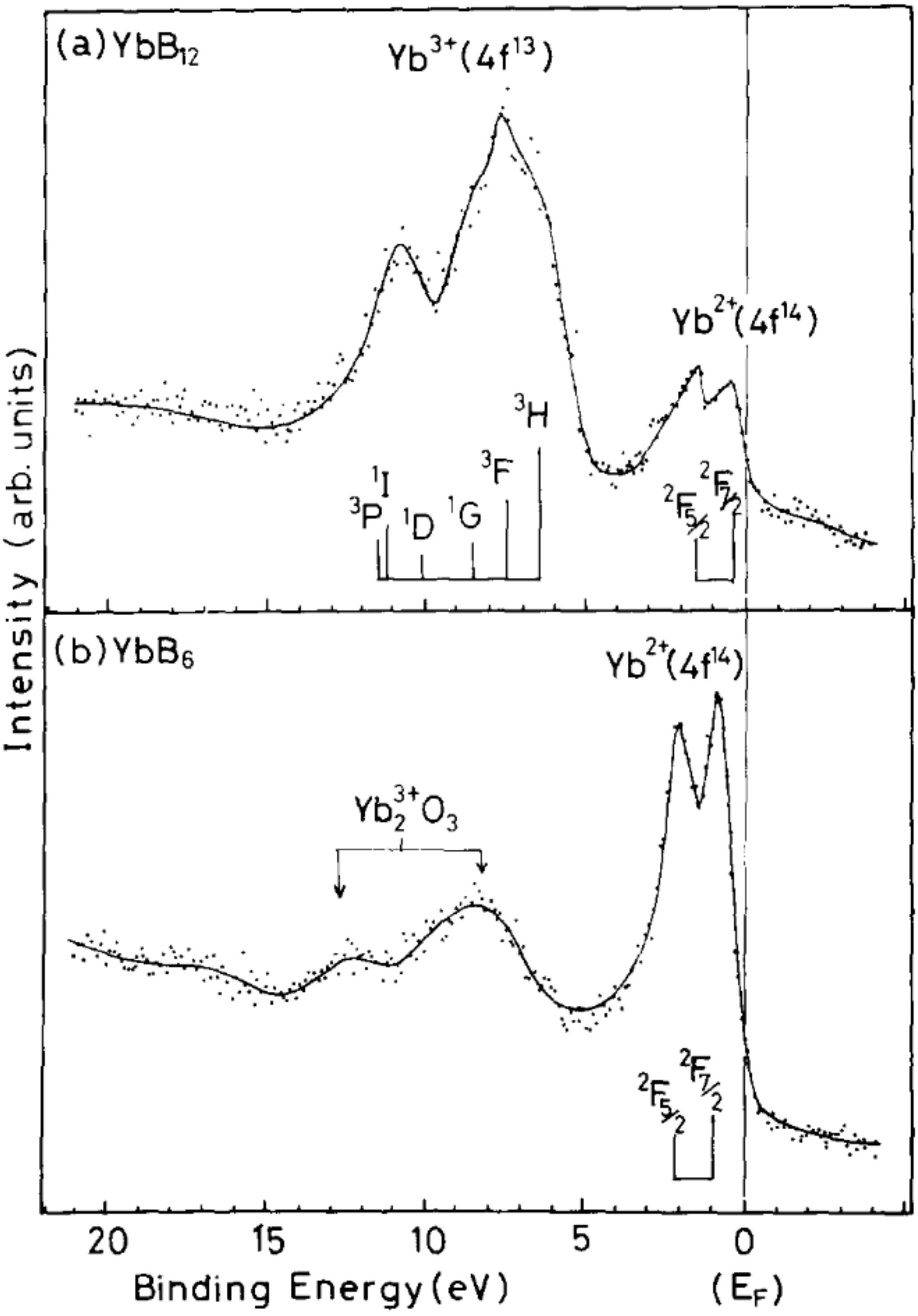

Fig.6: The $4f$ multiplets and the valence band for YbB_{12}(a) and YbB_6(b) from Ref. [17].

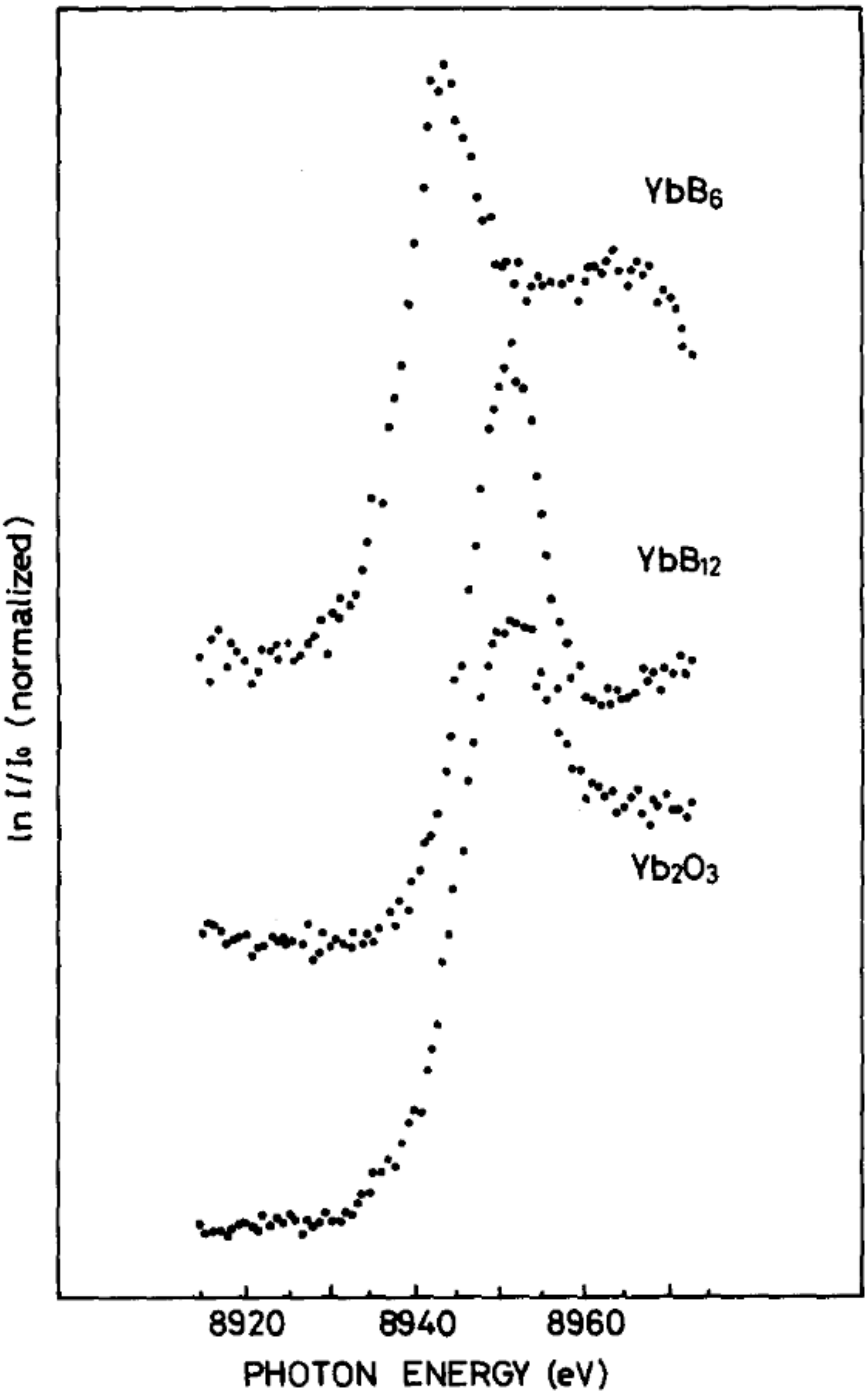

Fig.7: X-ray L_{III} absorption spectra for YbB_{12} and YbB_6 from Ref. [15].

From electrical conduction measurements, the gradual opening of an energy gap in YbB_{12} is seen below 100 K[18]. The formation mechanism of the energy gap has been explained by the coherent Kondo singlet mechanism[19, 20] and the c-f hybridization mechanism[21, 22]. In the former mechanism, the energy gap corresponding to the binding energy ($k_{\mathrm{B}}T_{\mathrm{K}}$) of the Kondo singlet is formed by development of the coherence of Kondo singlets at each lattice rare-earth ion site. In the latter mechanism, the conduction electrons and f-electrons have the same number of orbital degeneracies and form an energy gap as a result of hybridization with band inversion. This means that Kondo lattices with no excess of orbital degeneracy can become Kondo insulators. To investigate the detailed mechanism of energy gap formation, the temperature dependence and shape of the density of states (DOS) and the magnitude of the energy gap have been evaluated by various experimental techniques. To investigate both the charge and the spin gap, our group have measured the electrical resistivity[15, 18, 23], Hall effect[15, 18], specific heat[18], optical conductivity [16], photoemission spectrum[24, 25], inelastic neutron scattering[26, 27, 28, 29, 30], nuclear magnetic resonance (NMR)[18, 31], and high-field magnetization [32, 33, 34]. The magnitudes of the charge and spin gap are comparable within small deviation according to the results of experiments and analysis. In the following paragraphs, I explain the magnitude of the energy gap and its dependence on the temperature and magnetic field.

First, I mention the size and development of the charge gap. The thermally activated energy $\Delta E^{c} = E_{g}^{c} \,/\, 2k_{\mathrm{B}}$ of YbB_{12} was evaluated from electrical resistivity $\rho\,(T)$ and Hall resistivity $R_{\mathrm{H}}(T)$ measurements[18, 23]. In general, thermally activated energy is evaluated from the slope of the Arrhenius plot (log ρ *vs* $1/T$). The Arrhenius plots of $\rho\,(T)$ and $R_{\mathrm{H}}(T)$ for YbB_{12} have a bending point at 15 K, and two thermally activated energies can be evaluated, as shown in Fig. 8. The thermally activated energies evaluated above and below 15 K are called $k_{\mathrm{B}}\Delta E_{1}^{c}$ and $k_{\mathrm{B}}\Delta E_{2}^{c}$, respectively. I define this bending point as $T_0 = 15$ K. The temperature region above T_0 is ΔE_1^c-dominant and the region below T_0 is ΔE_2^c-dominant. From $\rho\,(T)$, $\Delta E_1^c = 68$ K and $\Delta E_2^c = 25$ K, and from $R_{\mathrm{H}}(T)$, $\Delta E_1^c = 90$ K and $\Delta E_2^c = 28$ K.

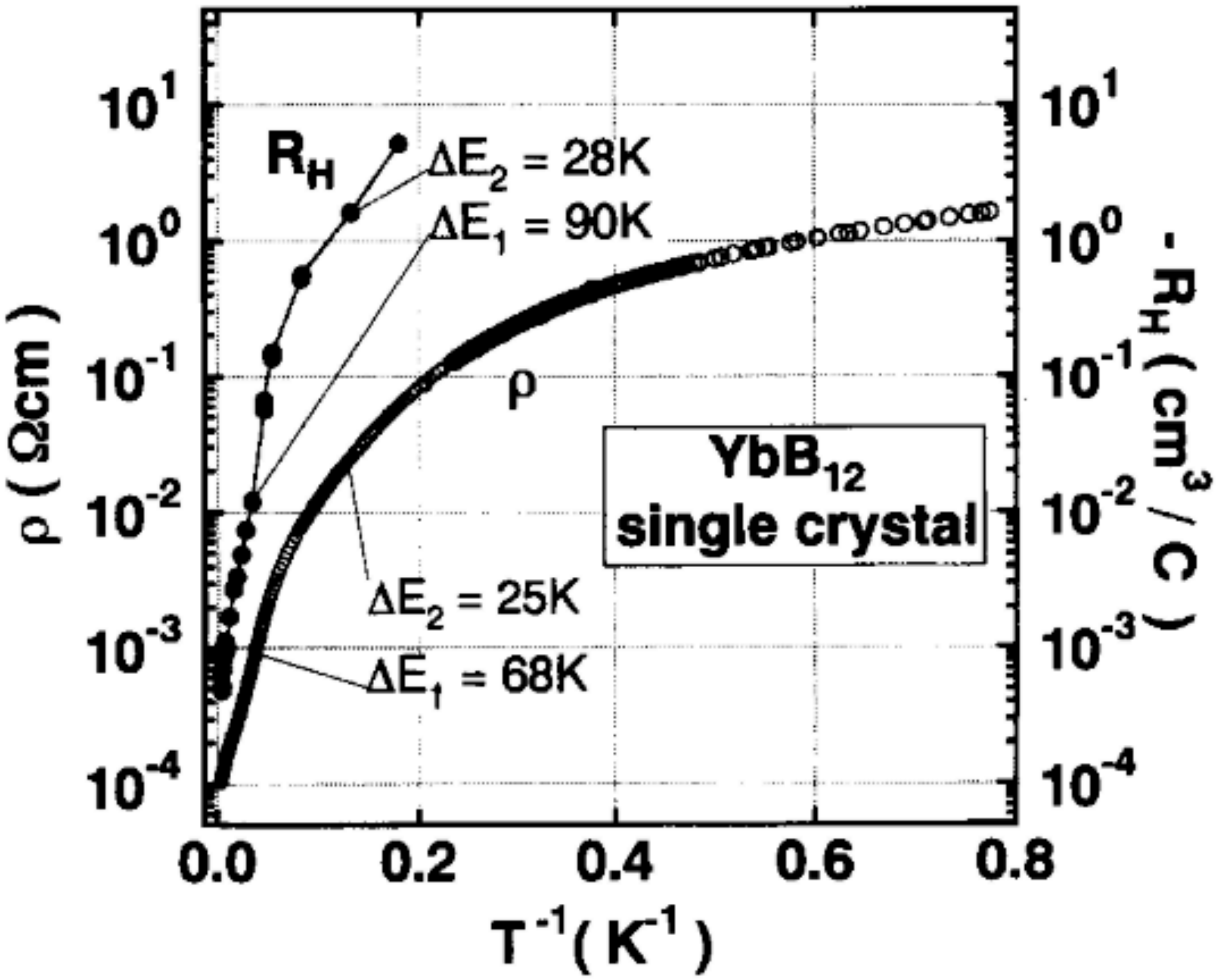

Fig.8: Temperature dependence of electrical resistivity $\rho\,(T)$ and Hall coefficient $R_{\mathrm{H}}(T)$ for a single crystal sample of YbB_{12} from [23].

The optical conductivity $\sigma\,(\omega,\,T)$ and reflectivity of YbB_{12} induce the temperature-dependent behavior of the energy gap[16], which shows a gradual decrease with decreasing temperature below 100 K, as shown in Fig. 9. $\sigma\,(\omega,\,T)$ at 20 K rises from about 14–20 meV, and there is a shoulder at 37 meV. The magnitude of the energy gap estimated from the results of photoemission spectroscopy[24, 25] is comparable to the energy position of the onset in $\sigma\,(\omega,\,T)$.

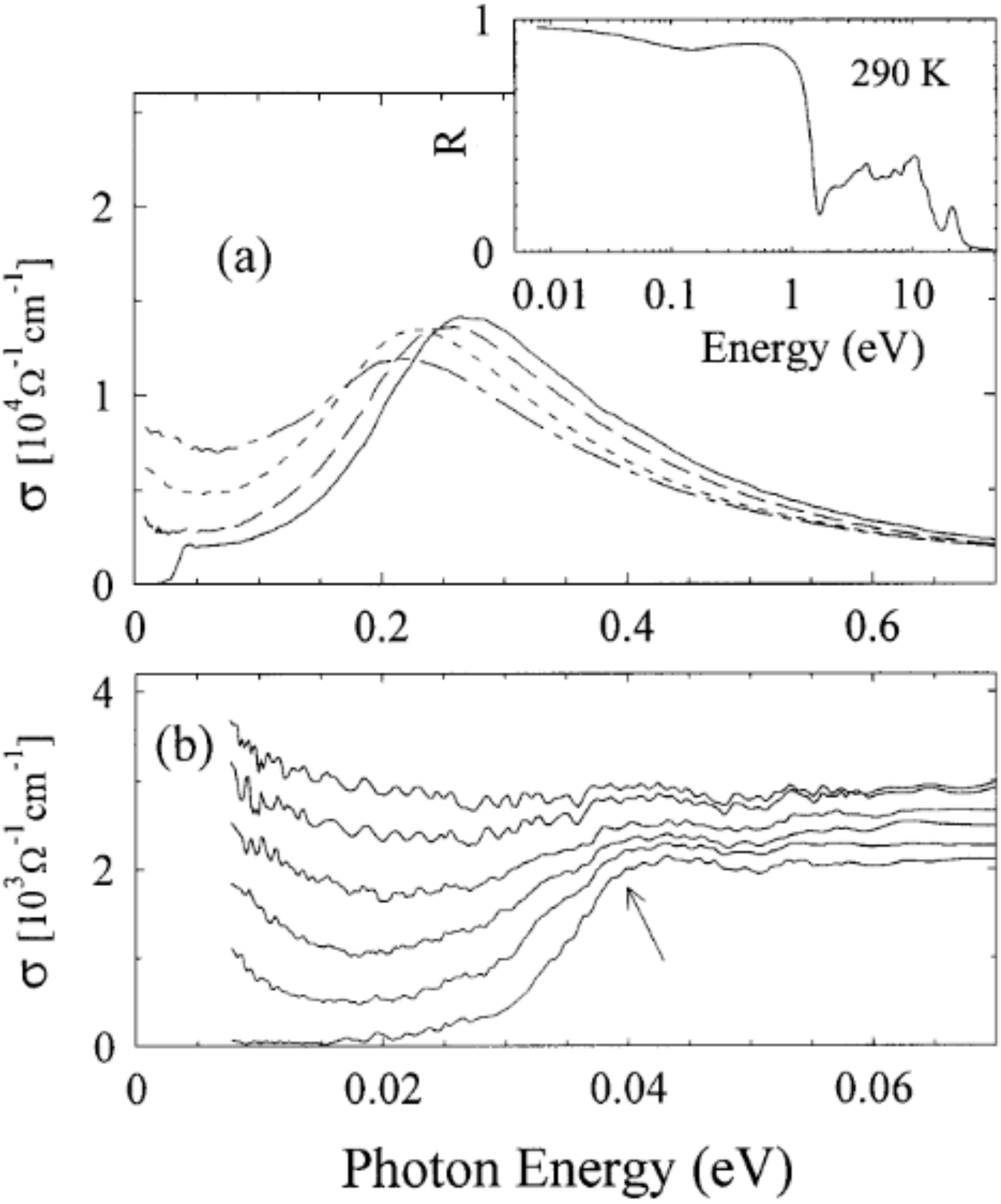

Fig.9: (a) Optical conductivity $\sigma(\omega, T)$ of YbB_{12} single crystal at 290 K (dotted-dashed curve), 160 K (dotted), 78 K (dashed) and 20 K (solid) from Ref. [16]. The inset shows the reflectivity at 290K. (b) $\sigma(\omega, T)$ of YbB_{12} at (from top to bottom) 78, 70, 60 50, 40, and 20 K. The arrow indicates the "shoulder" discussed in the text.

Next, the evaluation of the spin gap $E_g^s = 2k_B\Delta E^s$ is described. The nuclear spin-lattice relaxation rates $1/T_1$ of ^{11}B and ^{171}Yb in NMR [31] is shown in Fig. 10. $1/T_1$ of ^{11}B and ^{171}Yb show thermally activated temperature dependence with $\Delta E^s = 70$ and 87 K, respectively. In addition, $1/T_1$ of ^{11}B-NMR for YbB$_{12}$ has a minimum around $T_0 = 15$ K and a peak at 6 K, similarly to the ^{11}B-NMR results for SmB$_6$. The origin of this peak was interpreted to be relaxation due to a low density of defects at the Yb site[35].

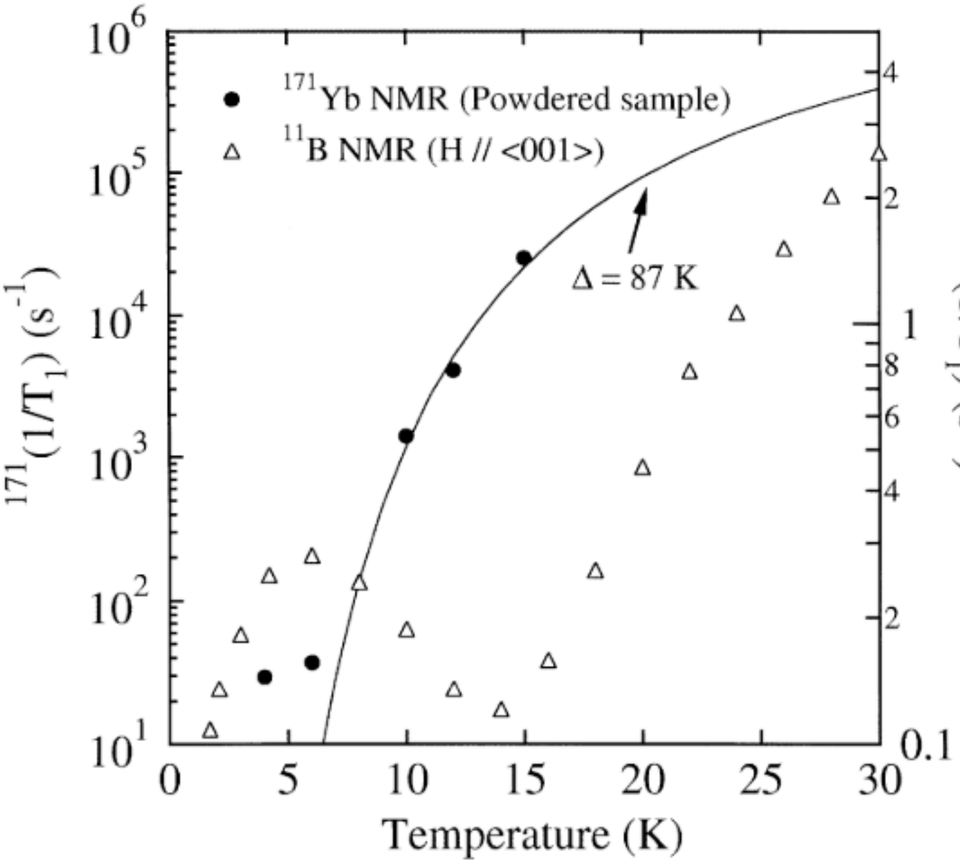

Fig.10: Temperature dependence of $1/T_1$ at low temperature in YbB$_{12}$ from Ref. [31]. The solid curve represents the activation-type behavior with an activation energy of 87 K. Solid circles show temperature dependence of ^{171}Yb $1/T_1$ in the sample powdered by crushing the single crystal. Open triangles show ^{11}B $1/T_1$ at H‖<001> in the single crystal.

The magnetic specific heat shows Schottky-type behavior with a peak around 40 K [36]. $\Delta E^s = 70$ K was obtained from the fitting of the magnetic specific heat of YbB_{12} after deducting the phonon contribution to the specific heat for YbB_{12}, which was calculated using the specific heat for LuB_{12}. The temperature dependence of magnetic specific heat for YbB_{12} is shown in Fig. 11.

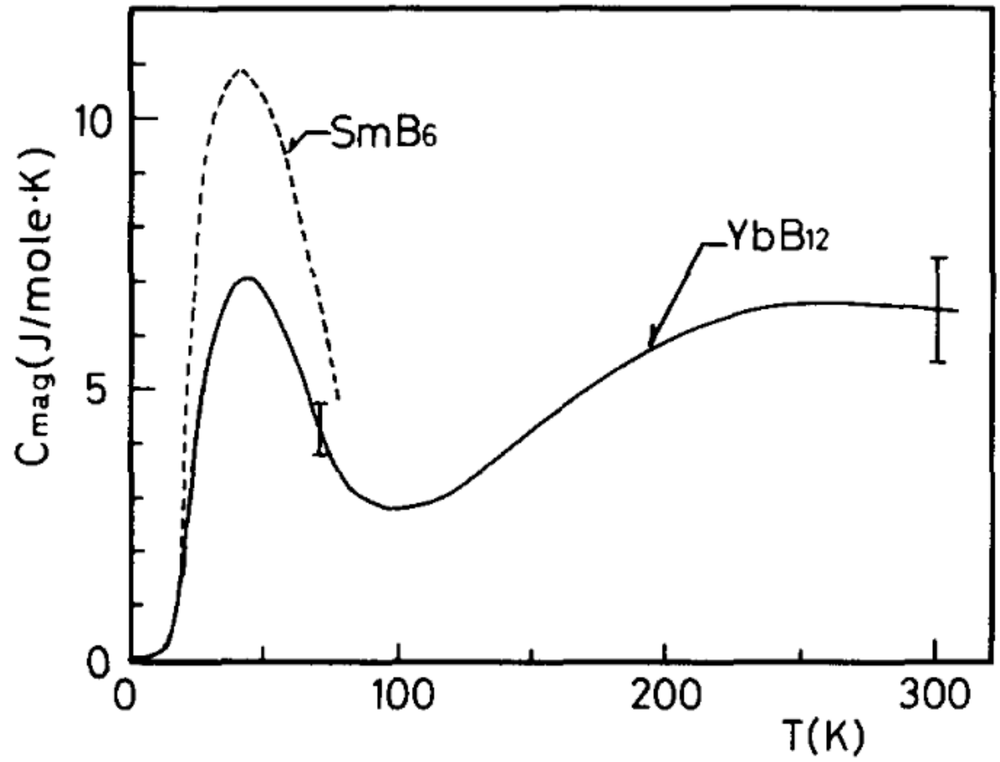

Fig.11: Magnetic specific heat of YbB_{12} (defined as the difference from the adjusted value in LuB_{12}) from Ref. [36].

To study the spin gap of YbB_{12}, high-field magnetization measurements have been performed, and a metamagnetic transition occurs at a high field of about 50 T, where electrical conduction changes from insulator to metal[32]. Recently, the magnetization of YbB_{12} at high magnetic fields up to 120 T has been measured and it has been found that an additional small transition occurs at 102 T, as shown in Fig.12. The magnetization of YbB_{12} was found to saturate around 112 T. A rigid band DOS model has been proposed using the shapes of the field derivative of the magnetization dM/dB around these two transitions[34], as shown in Fig. 13. A symmetric DOS model based on the dM/dB geometry is used to explain the mechanism of the two metamagnetic transitions at $B_{c1} = 50$ T and $B_{c2} = 102$ T due to Zeeman splitting.

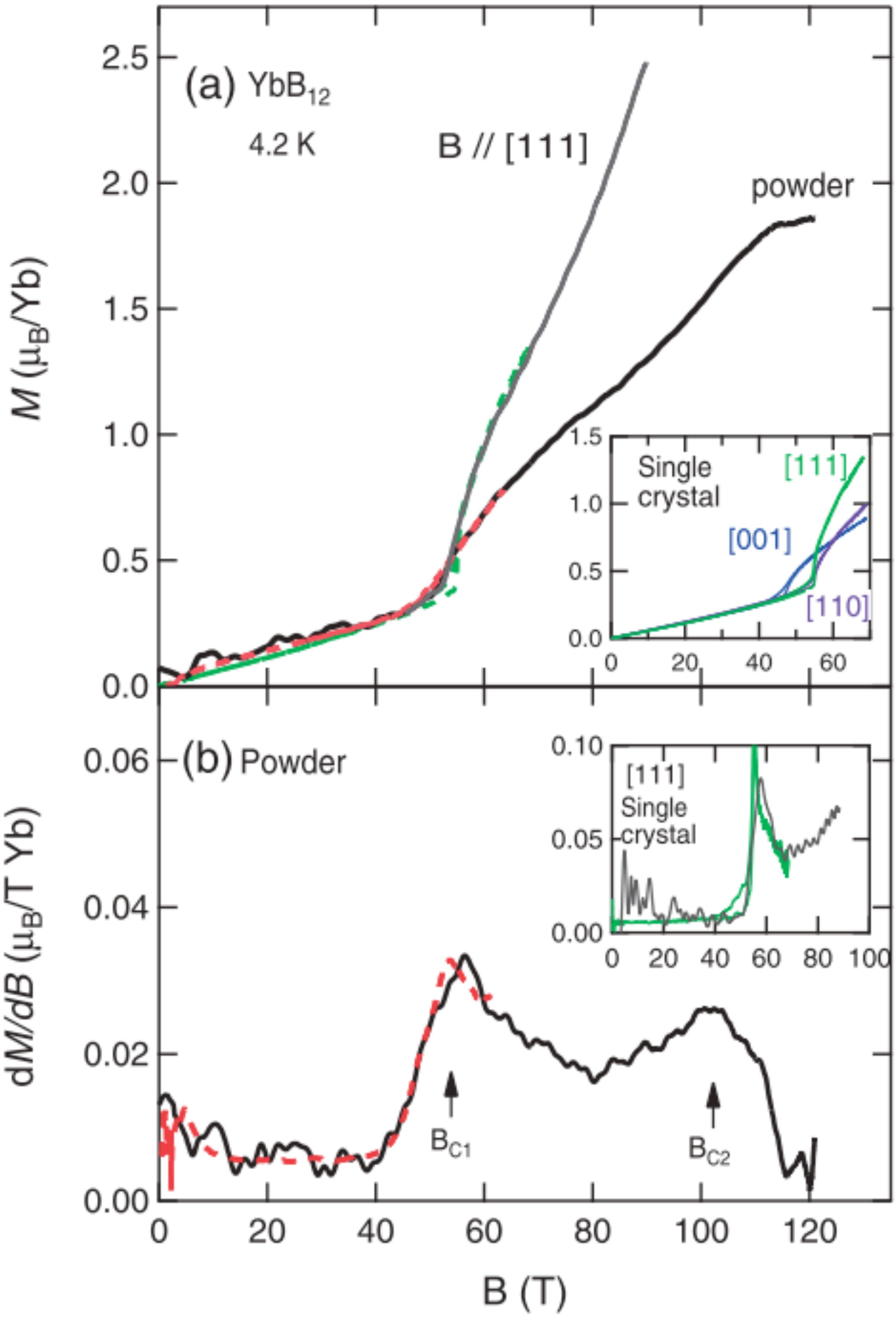

Fig.12: (a) Magnetic field dependence of the magnetization of YbB12. (b) The field derivative of the magnetization (dM/dB) curves. (a), (b) are taken from Ref. [32]

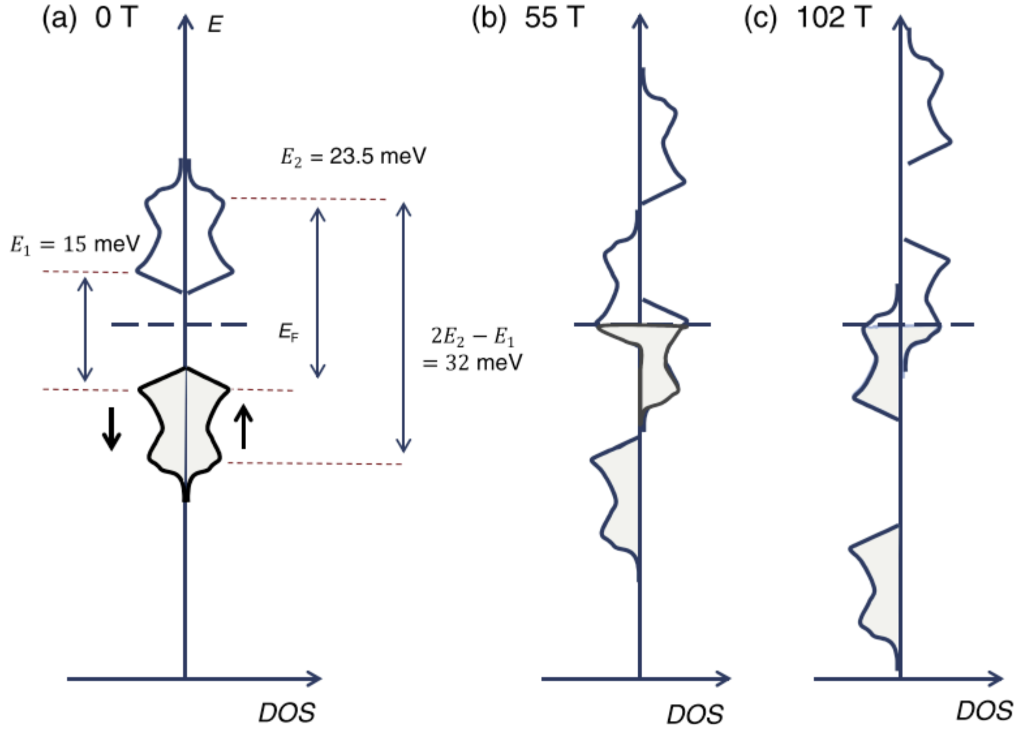

Fig.13: (a) Schematic of assumed density of states (DOS) at 0T defined from Fig.12 (b). (b) DOS expected in magnetic fields where the I-M transition takes place at B_{c1}. (c) DOS expected in magnetic fields where the second metamagnetism takes place at B_{c2}.

The investigation of the formation mechanism of energy gap in YbB_{12} has also been approached by numerical methods. In the local density approximation (LDA) method, the energy gaps does not open and YbB_{12} becomes half-metallic, but in the LDA+U method, the gap of about 200 K opens[37]. The difference between the results of LDA and LDA+U method is due to the shift of the 4f level, the shift caused by the introduction of the Coulomb repulsion energy between f-electrons and the artificial shift (about 0.3 Ryd($\sim$ 4.1 eV)), which causes the overlap of the 5d conduction band and the 4f level. Without this artificial shift, no gap is yielded, which is interpreted to be due to the over-counting of the exchange energy of the 4f electrons of the heavy Yb atoms compared to the 2p electrons of the light B atoms, because the 4f electrons are located around the core-electrons which contribute the LDA potential.

In the band structure and the calculated DOS shown in Fig. 14 and 15, a gap of about 0.0013 Ryd ($\sim$ 205 K (17.7 meV)) is formed at ϵ_F due to the hybridization of the $4f$ Γ_8 state and the conduction band.

The formation of the band gap was also confirmed by the tight-binding model using the $5d$ and $4f$ orbitals of Yb atoms, and the shift of the $4f$ level was also carried out in the LDA+U method. Here, the dispersion with an indirect gap of 0.003 Ryd is shown in Fig. 16. The DOS generated by tight-binding model is shown in Fig. 17. The current band calculation shows that the energy gap is formed by the hybridization of conduction bands with the same number of degeneracies as the Γ_8 ground state, although the size depends on the magnitude of the $4f$ level shift.

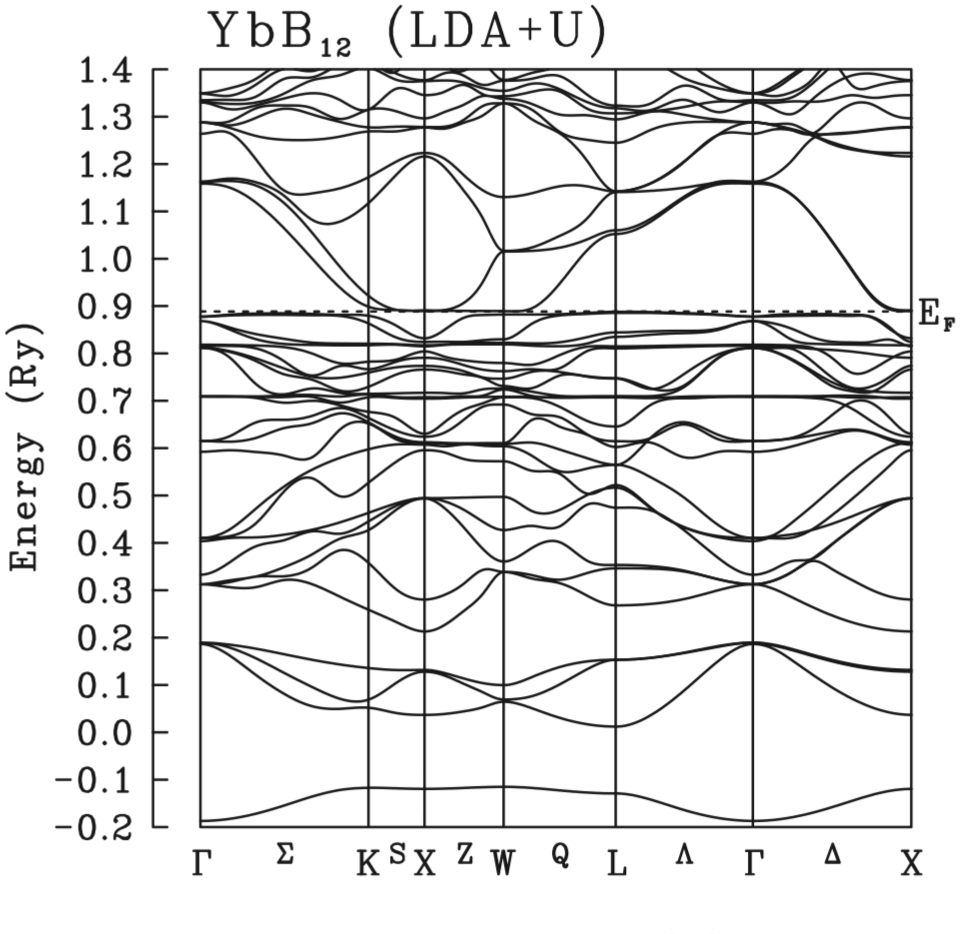

Fig.14: LDA+U band calculation for YbB_{12}[37].The three flat bands correspond to the $4f$ $\Gamma_x (x = 6,7,$ and $8)$.

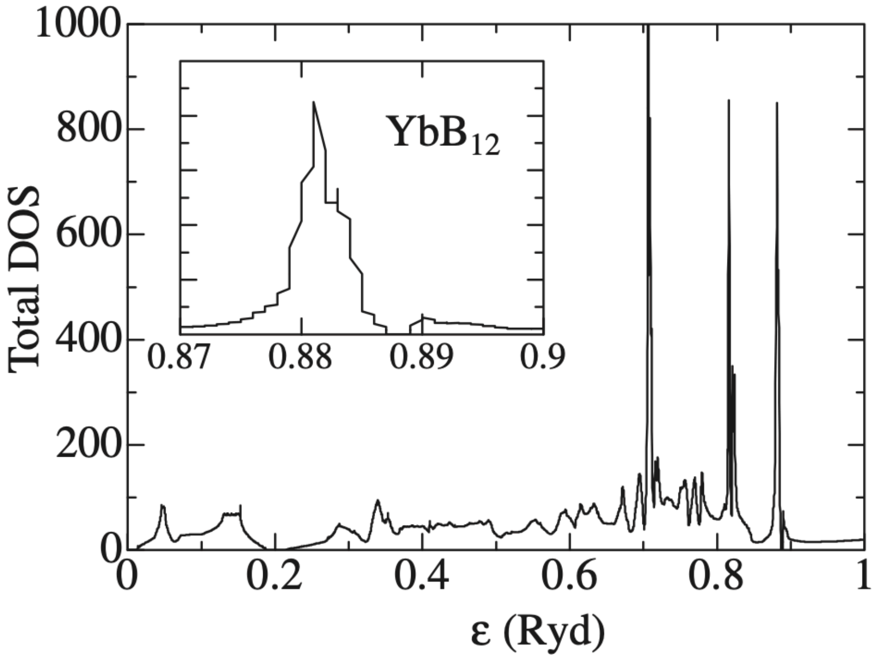

Fig.15: The density of states of YbB_{12} calculated by the LDA+U method[37].

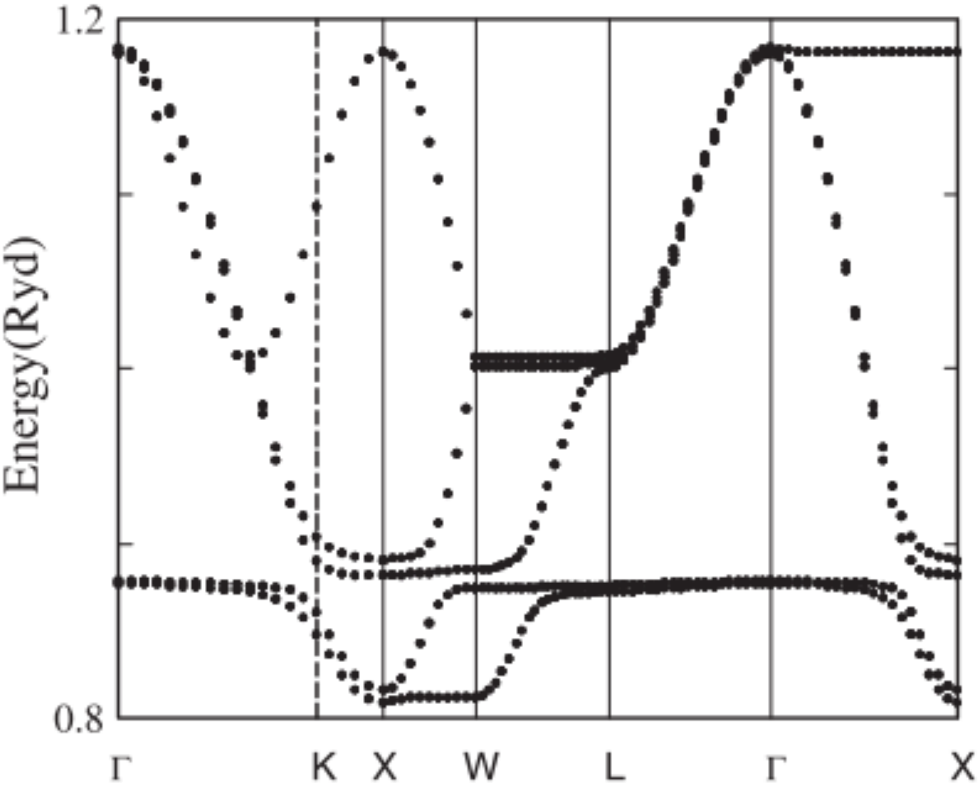

Fig.16: Energy dispersion of the tight-binding model fo the YbB_{12}[37].

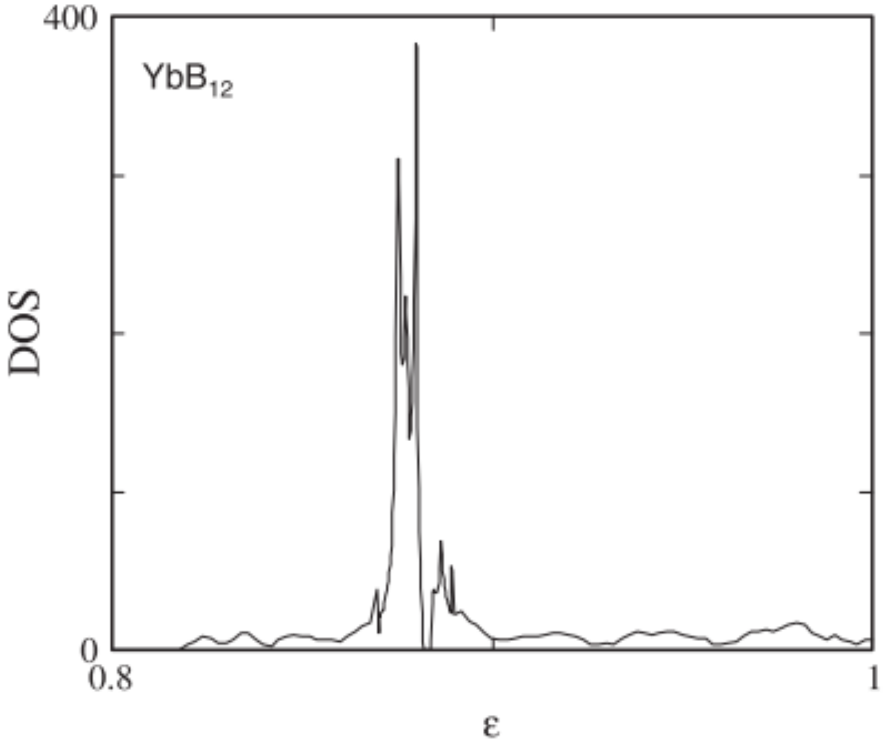

Fig.17: DOS of the tight-binding model for the YbB_{12}[37].

1.5.1 Topological insulator YbB_{12}

SmB_6 and YbB_{12} are Kondo insulators but their conduction at low temperatures is finite and they show metallic behavior. This metallic conduction at low temperatures is theoretically due to surface conduction in a topological insulator (TI)[38, 39, 40].

Since TI has a combined resistivity due to this thickness-independent surface conduction and thickness-dependent bulk insulator region, the resistivity at low temperatures ($T < 3$ K) of SmB_6 shows thickness dependence[42]. To confirm the spin polarization of the topological surface state (TSS) band of SmB_6, angle-resolved photoemission spectroscopy (ARPES) measurements were carried out[43]. The spins of surface electrons are locked perpendicular to momentum direction on the surface of TI and the observed surface band of SmB_6 shows the same feature as referred in the TI theory. ARPES measurements on YbB_{12}

have been also carried out to observe TSS [44]. Fermi surface was not observed in bulk band but presented surrounding the $\overline{\Gamma}$ point on the surface, as shown in Fig. 18 (b). ARPES circular-dichroism plot also show a sign reversal around the $\overline{\Gamma}$ point in the surface Brillouin zone (SBZ) of the (001) plane suggesting a spiral spin-orbit polarization structure, as shown in Fig. 19. This result confirms that the surface state of YbB_{12} is nontrivial. The TSS significantly appears below T_0 as seen in ARPES and $\rho\,(T)$ measurements.

As mentioned above, theory and experiment suggest that there is a topological surface conduction state in YbB_{12}, although there is uncertainty about the degree of shift of the f-levels in the band calculation. On the other hand, the relationship between the bulk in-gap state and the surface state is still unclear.

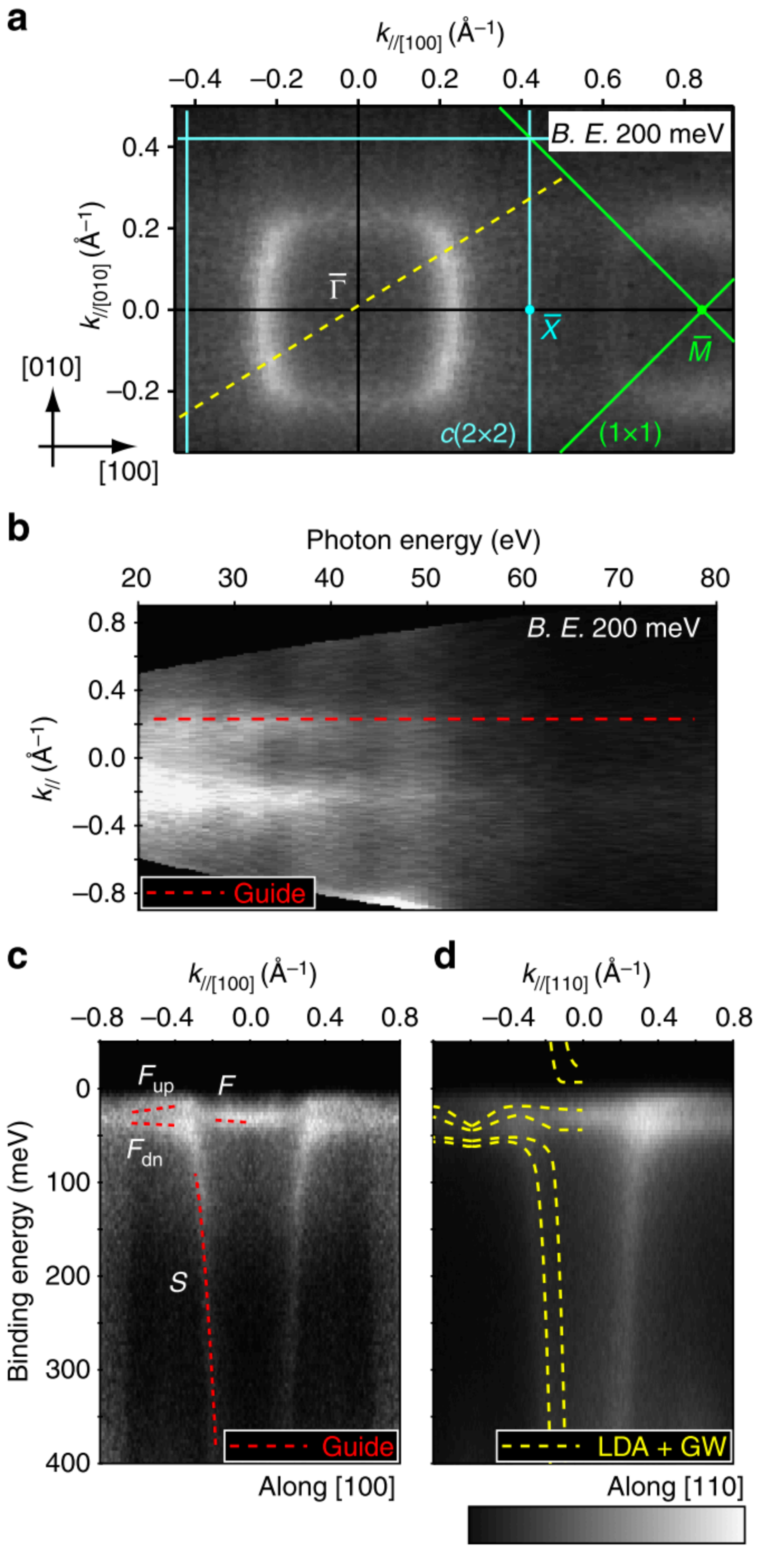

Fig.18: ARPES data of YbB_{12} taken below 20 K. (a) Constant energy contours (ECs). Thin lines represent the SBZ boundary. (b) Energy and momentum distribution curves (MCDs) along a dashed line in (a).(c,d) ARPES intensity maps. (a), (b), (c) are taken from [44]

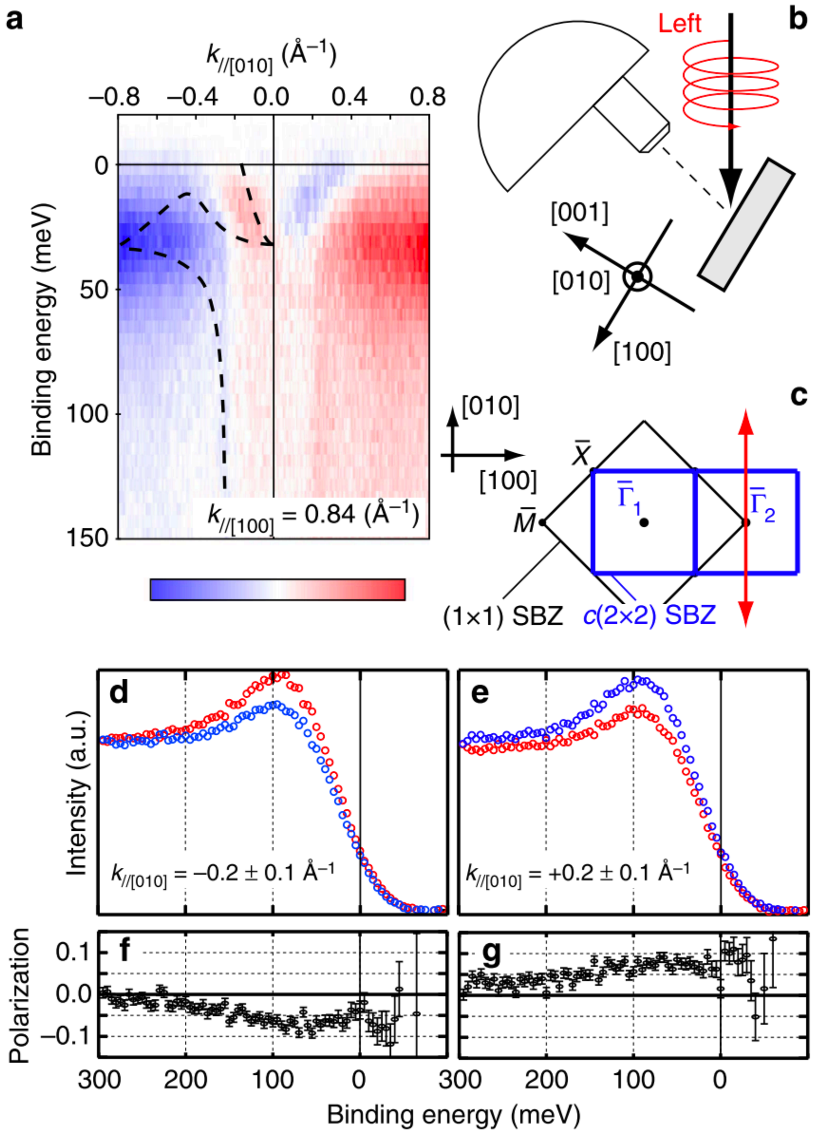

Fig.19: Orbital and spin polarization at the surface. (a) Circular dichroism plot with a 50 eV photon at 10 K. (b) Sample and photon incidence directions. (c) Surface Brillouin zone. (d,e) Spin-resolved ARPES energy distribution curve (EDC) obtained at 20 K. (f,g) Spin polarization of the EDCs shown in (d,e), respectively[44].

1.5.2 Unconventional Quantum oscillation for YbB_{12}

On the other hand, de Haas–van Alphen (dHvA) oscillations have recently been observed in the bulk insulator region of SmB_6[45, 46] and YbB_{12}[47, 48]. The dHvA and Shuvnikov-de Haas (SdH) oscillations are quantum oscillation (QO) which is driven by Landau quantization of energy levels contributed by some kinds of Fermion under high-magnetic field. The SdH effect which is oscillation of electrical resistivity in magnetic field was also reported by Xiang *et al.* (2018) in YbB_{12}[48]. Fig. 20 shows oscillation of electrical resistivity in magnetic fields in YbB_{12}. The amplitude of SdH oscillations have showed angular dependence that can only be explained by a 3D Fermi surface, whereas the amplitude of the dHvA oscillations have showed an angular dependence on magnetic field suggestive of a 2D Fermi surface, as shown in Fig. 21. The amplitudes of these oscillations follow the Lifshitz-Kosevich formula well and it suggests that they are caused by some kinds of Fermion.

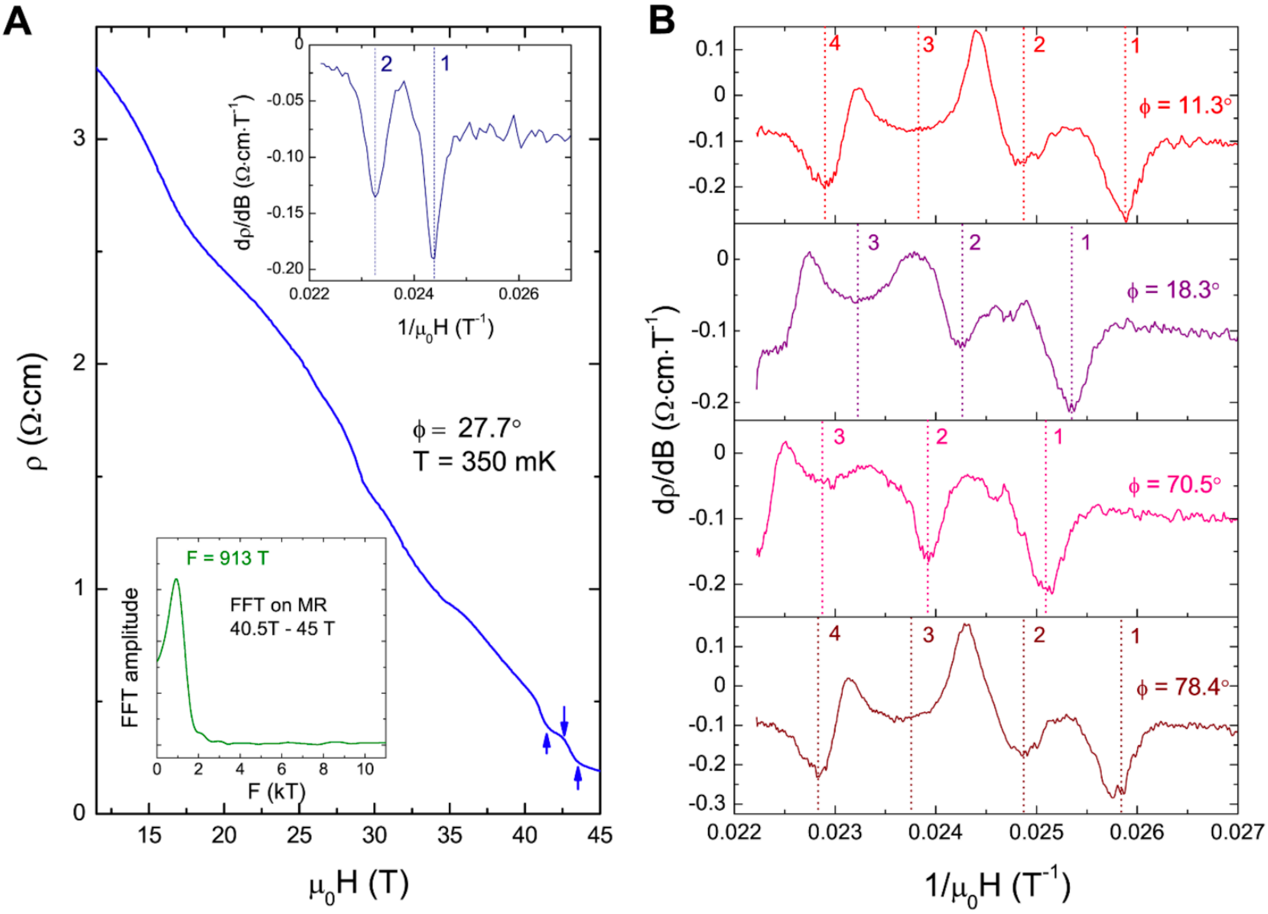

Fig.20: Oscillation of electrical resistivity in magnetic fields in YbB$_{12}$[48]. (A) Resistivity of YbB$_{12}$ as a function of magnetic field measured up to 45 T taken at $T = 350$ mK. (B) Field deviation of sample resistivity at four different tilt angles.

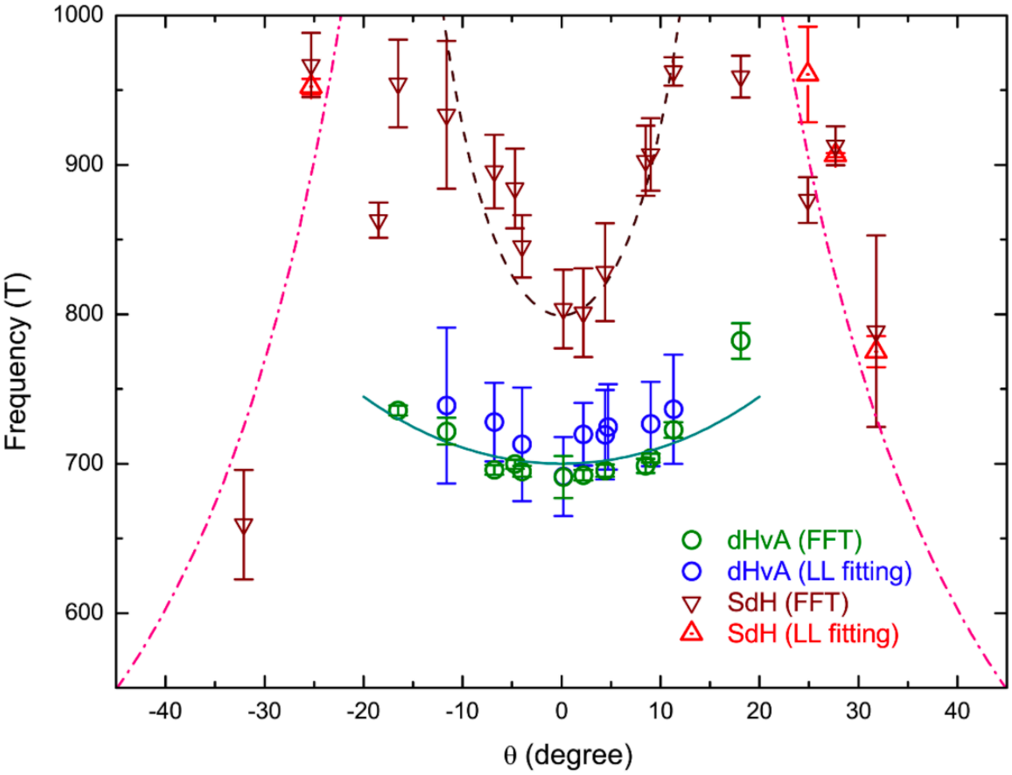

Fig.21: Angle dependence to magnetic field of quantum oscillation frequency of YbB_{12}[48]. Circles are dHvA frequencies obtained from FFT. The solid line is a calculation using two-dimensional Fermi surface model. Triangles are SdH frequencies.

In this context, the extrapolation to the absolute zero temperature of the non-phonon part of the thermal conductivity suggests the existence of gapless fermionic excitations[49]. Violation of Wiedemann-Franz law including information of electronic thermal conductivity and electrical resistivity in YbB_{12} suggests that thermally gapless excitations originated by some bands other than surface metallic conduction bands [49]. Furthermore, the frequency and effective mass deduced from the SdH vibration in the insulating and magnetic-field-induced metallic phases are invariant[50]. This suggests that the QO in both KI and Kondo metal (KM) phases has a common origin.

The origins of this in-gap state are still under debate, and additional studies are being actively conducted.

1.5.3 Nonmagnetic impurity dope effect in $\mathrm{Yb}_{1-x}\mathrm{R}_x\mathrm{B}_{12}$

As mentioned above, it has been argued that the Fermi surface exists even in a bulk KI layer. In YbB_{12}, conduction discontinuity and QO continuity coexist before and after the insulator-to-metal (IM) transition. In alloys, the transition process from KI to KM can be studied by controlling the substitution rate, which may provide information on these attractive effects.

With respect to substituted and impurity doping in KI, Schlottmann predicted the formation of an "impurity" band in the energy gap by breaking the coherence of the Kondo singlet, the so-called Kondo holes, using a numerical calculation based on the periodic Anderson model[51]. The calculated DOS is shown in Fig. 22. This prediction suggests an enhancement of low-temperature charge susceptibility and specific heat divided by temperature C/T by impurity band formation in the insulating phase. Similarly, Mutou's numerical analysis of symmetric bands based on PAM (KLM) showed that impurity bands are formed inside the energy gap in Kondo insulators, leading to an increase in spin susceptibility at low temperatures[52, 53], as shown in Figs. 23 and 24.

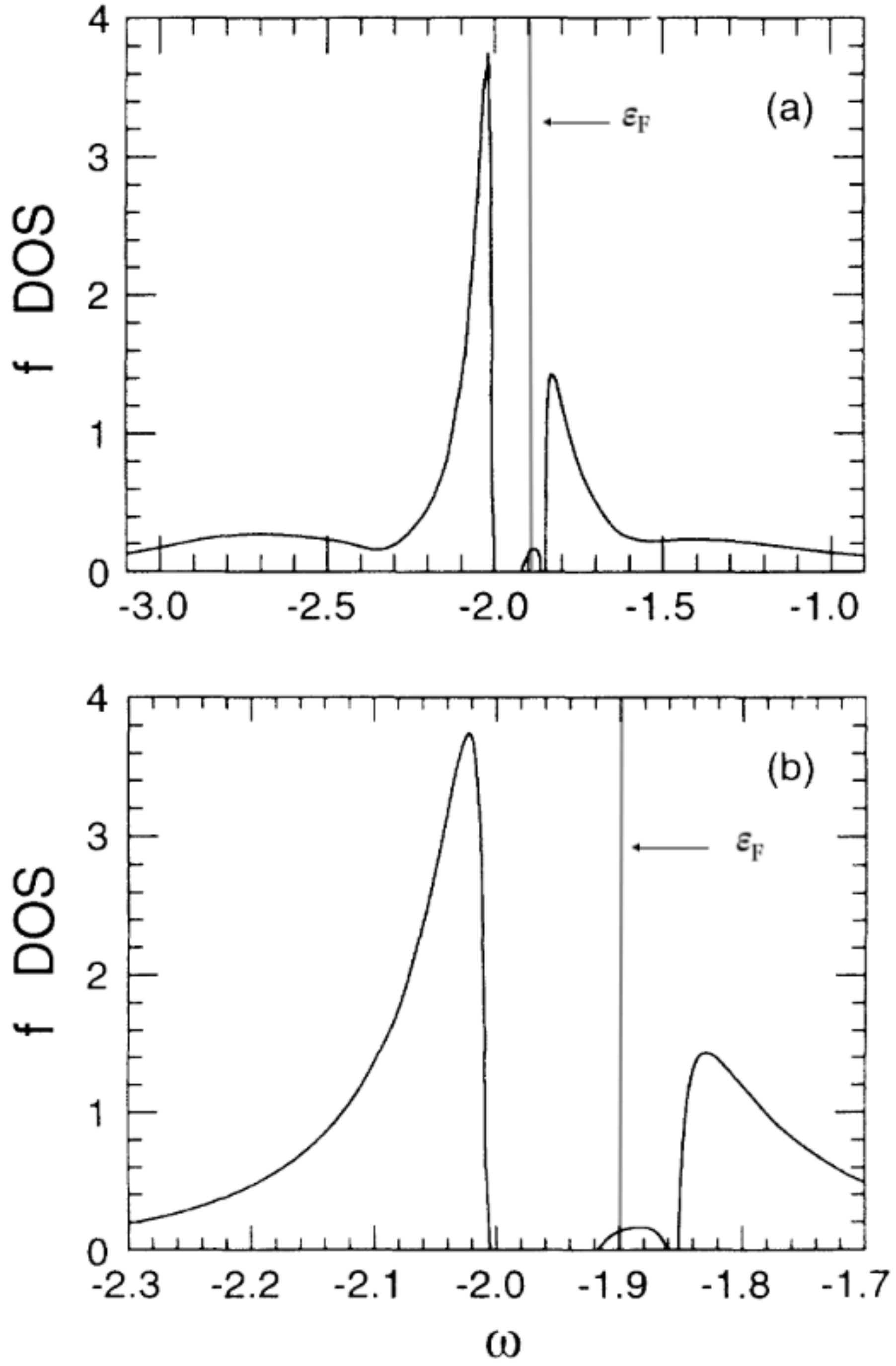

Fig.22: Calculated density of state based on periodic Anderson model with Kondo hole[51]. (a)f density of state (Hartree-Fock shifted). In this figure, ϵ_F is pinned in the impurity band (ϵ_F = -1.9). (b)Expanded view of the hybridization gap and impurity band.

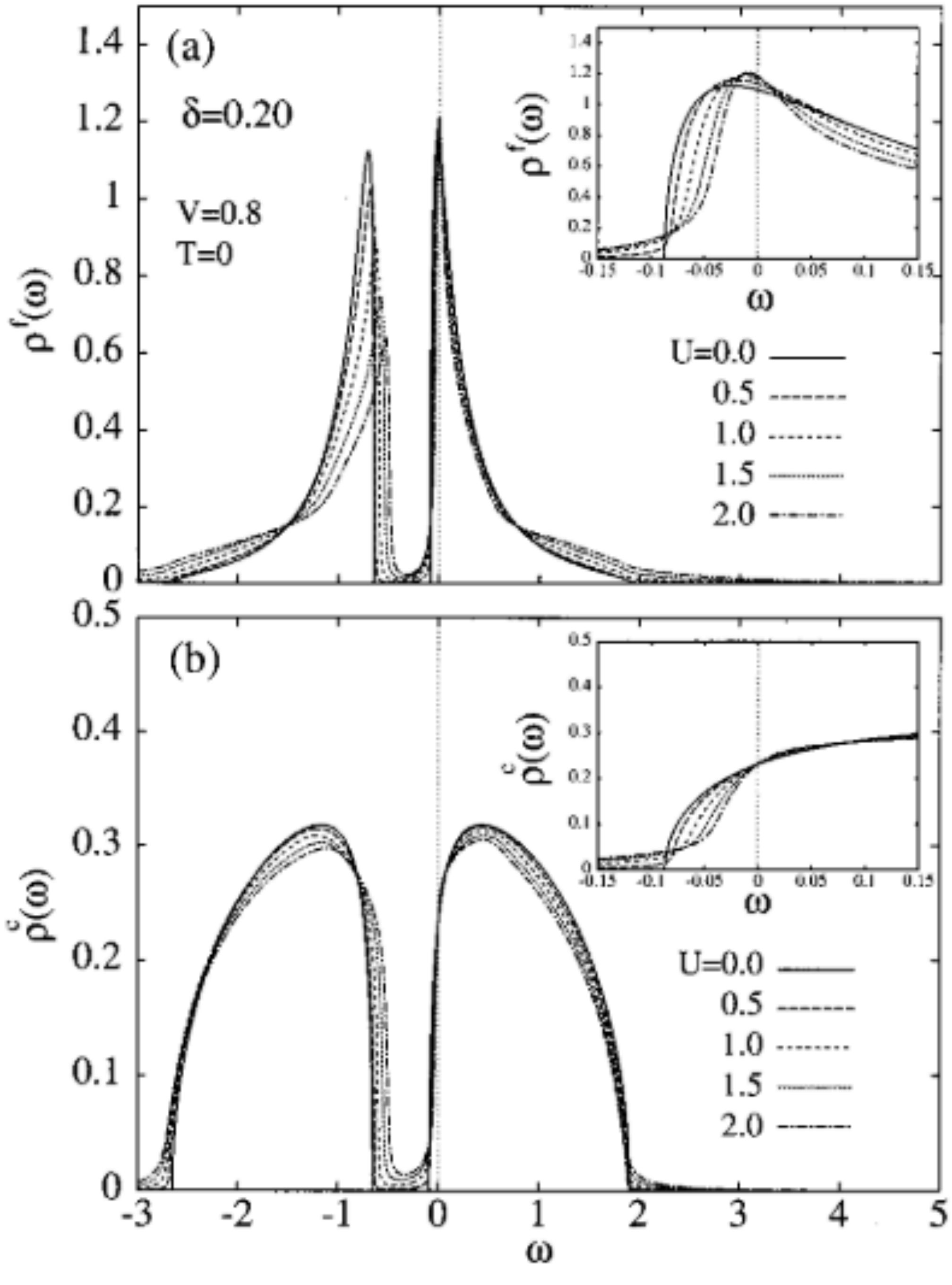

Fig.23: Calculated density of state based on Kondo lattice model with Kondo hole[52], where U is the Coulomb energy between f-electrons and the ϵ_F is $\omega = 0$.

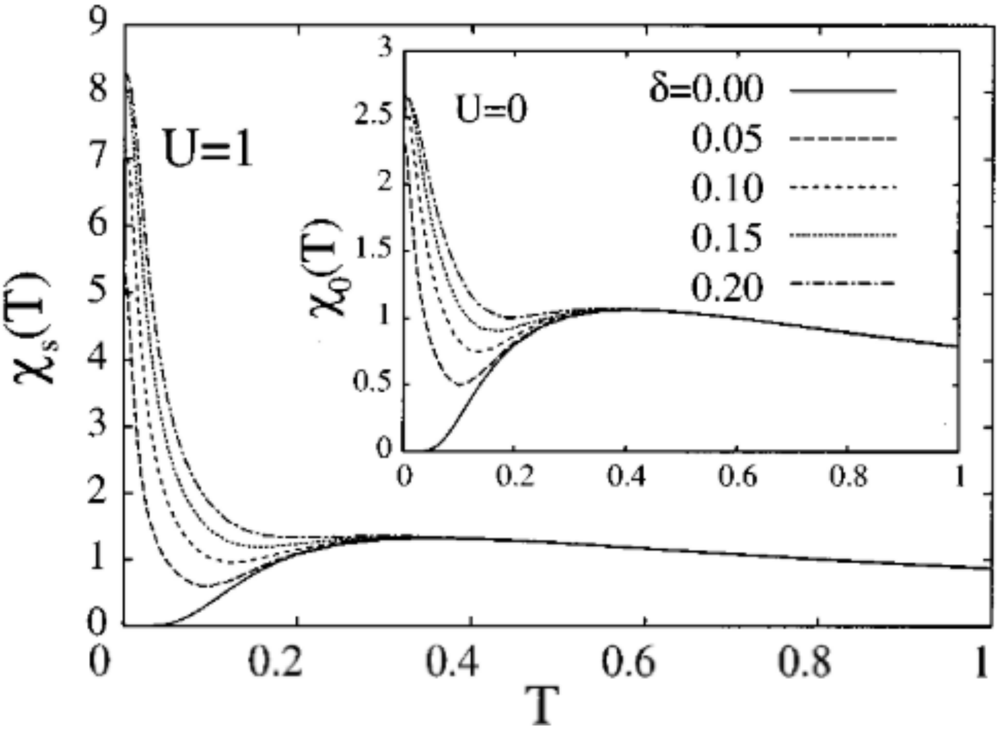

Fig.24: Impurity concentration δ-dependencies of spin susceptibility [52](U=1). Inset shows temperature dependence of the susceptibility for U = 0.

The conductivity and magnetic properties of $\mathrm{Yb}_{1-x}\mathrm{R}_x\mathrm{B}_{12}$ (R = $\mathrm{Lu}^{3+}, \mathrm{Y}^{3+}$, and Zr^{4+}) have been investigated. Here, R ion is not a rare earth, but a symbol for a nonmagnetic substitution ion. In order to evaluate the x dependence of the energy gap, the electrical resistivity[54, 55], specific heat[36, 56], and optical conductivity[57, 58] have been measured mainly for Lu-substituted alloys.

Since YbB_{12} has been attracting attention as a valence fluctuation material with an energy gap, the continuous transformation process from a valence fluctuation semiconductor to a dilute Kondo metal was investigated by nonmagnetic Lu substitution. $\rho(T)$ of polycrystalline $\mathrm{Yb}_{1-x}\mathrm{Lu}_x\mathrm{B}_{12}$ shows a decreasing behavior with substitution, and χ above 20 K also decreases with Yb ion dilution. However, χ below 20 K shows a rise due to the dilution of Yb ions as shown in Fig. 27, which is interpreted as the contribution of impurity at that time. This rise in χ in the low temperature region (below 20 K) is also observed in single crystal samples, as shown in Fig. 28, and the origin of this phenomenon has been unknown for a long time.

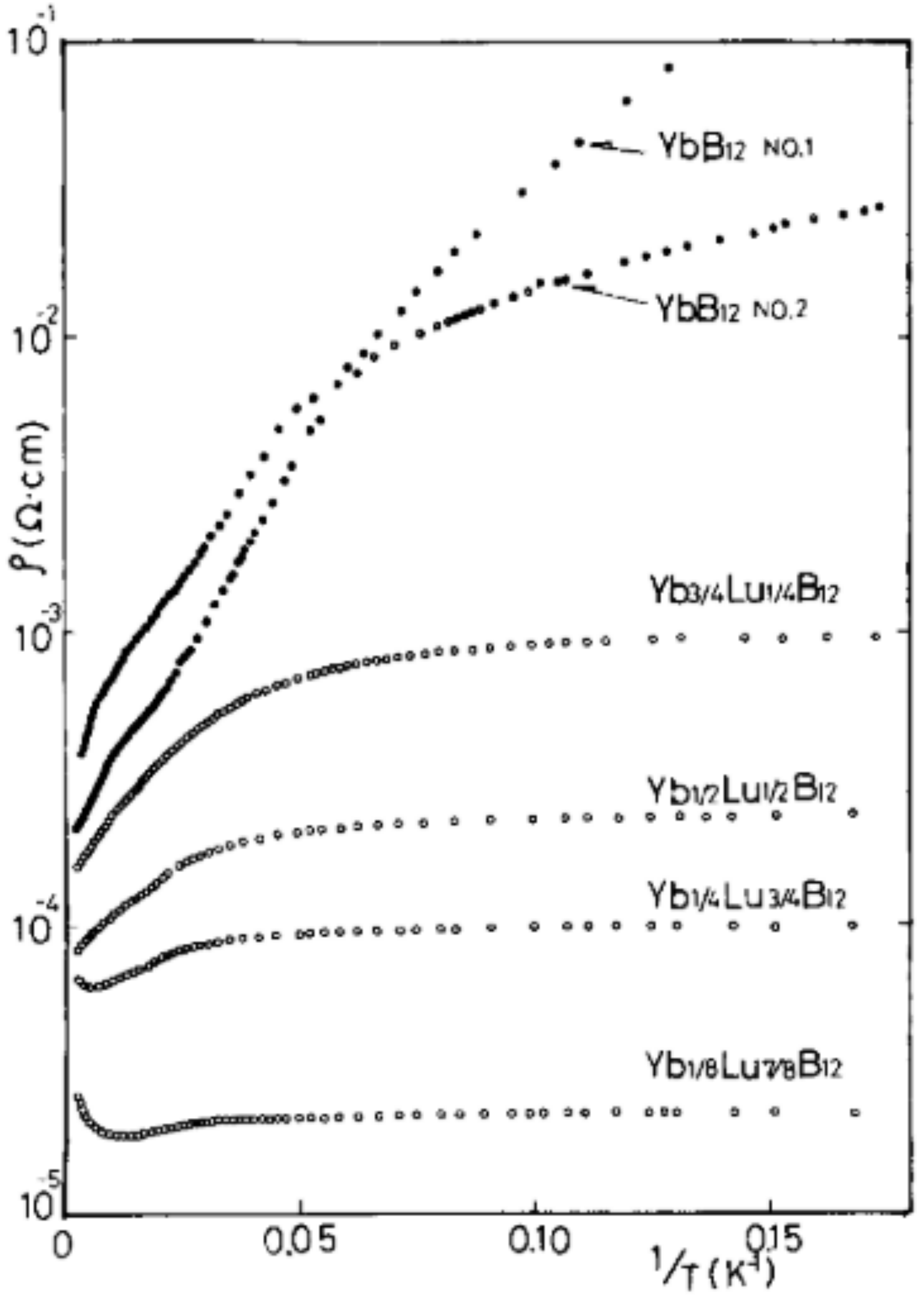

Fig.25: $1/T$ dependence of electrical resistivity ρ for polycrystalline $Yb_xLu_{1-x}B_{12}$[54].

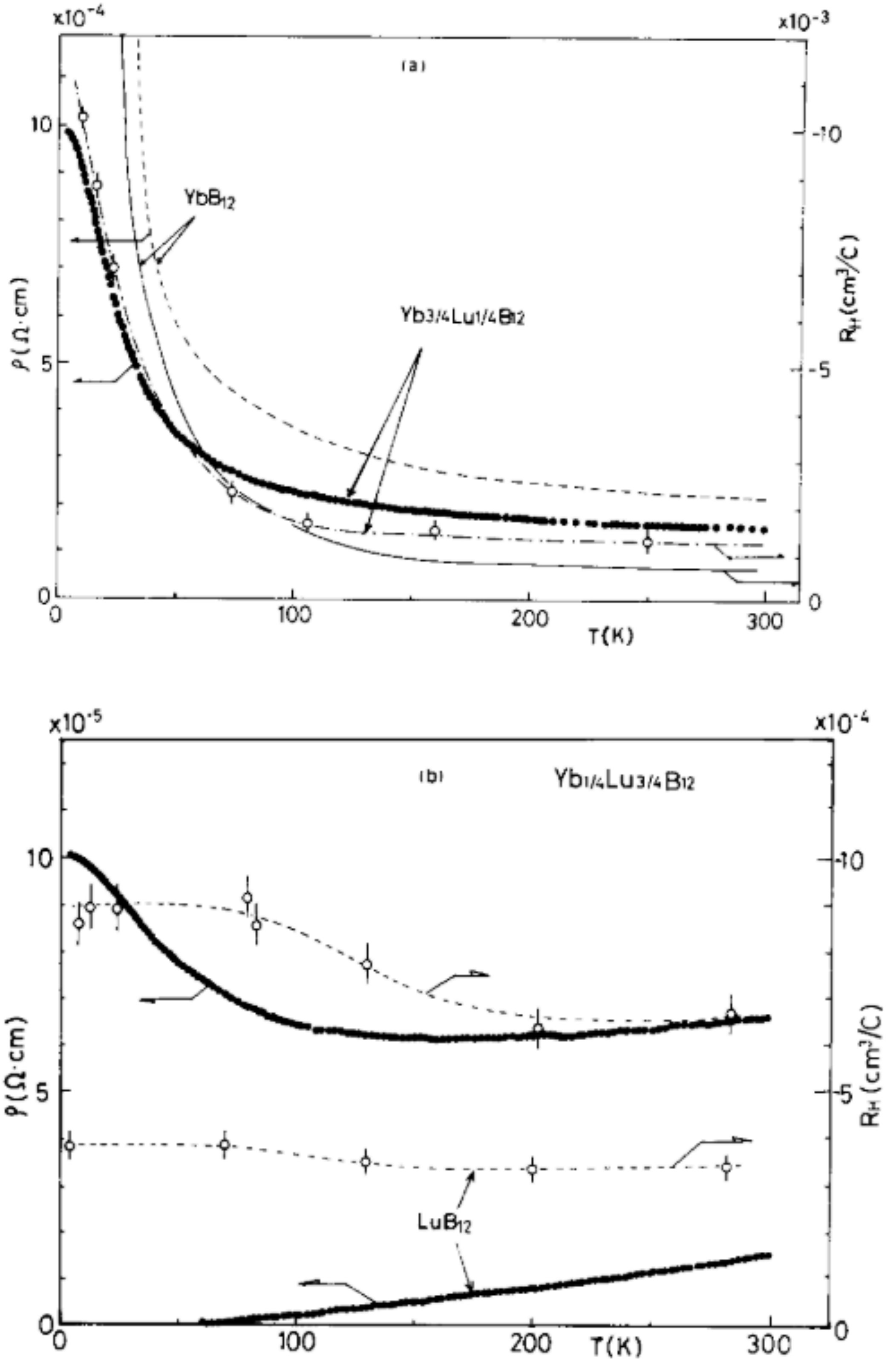

Fig.26: Temperature dependence of electrical resistivity ρ and Hall constant R_H for polycrystalline $Yb_xLu_{1-x}B_{12}$ (Yb concentration $x = 3/4$(a), 1/4(b), and 0(b))[54].

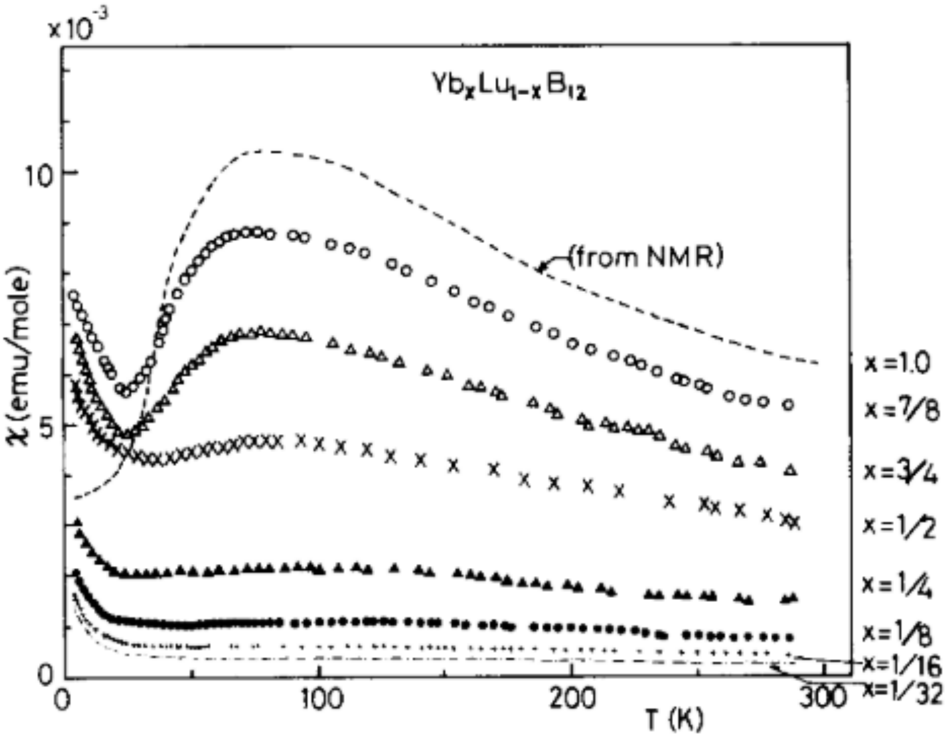

Fig.27: $\chi(T)$ for polycrystalline Yb$_x$Lu$_{1-x}$B$_{12}$[54]. In this figure, data for $x = 1$ (YbB$_{12}$) is obtained from NMR. The increase in the low temperature region ($T < 15$ K) is also present in χ for polycrystalline YbB$_{12}$.

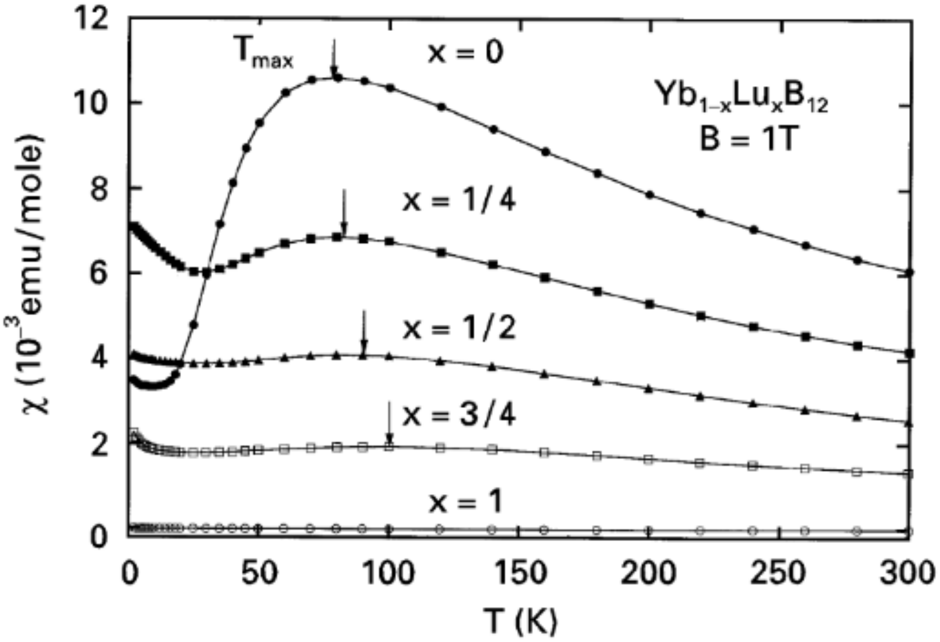

Fig.28: $\chi(T)$ for single crystals of Yb$_{1-x}$Lu$_x$B$_{12}$[55]. The increase of χ in the low-temperature region ($T < 15$ K) was suppressed, but not disappeared, by the single crystalization.

Okamura and coworkers have reported $\sigma(\omega, T)$ of $\mathrm{Yb}_{1-x}\mathrm{Lu}_x\mathrm{B}_{12}$, indicating that the position of the 40 meV shoulder observed in YbB_{12} does not change with increasing Lu concentration but that the number of thermal excitations inside the shoulder increases[57, 58]. $\sigma(\omega, T)$ suggests the formation of the impurity band in the energy gap by doping with nonmagnetic ions, as mentioned above.

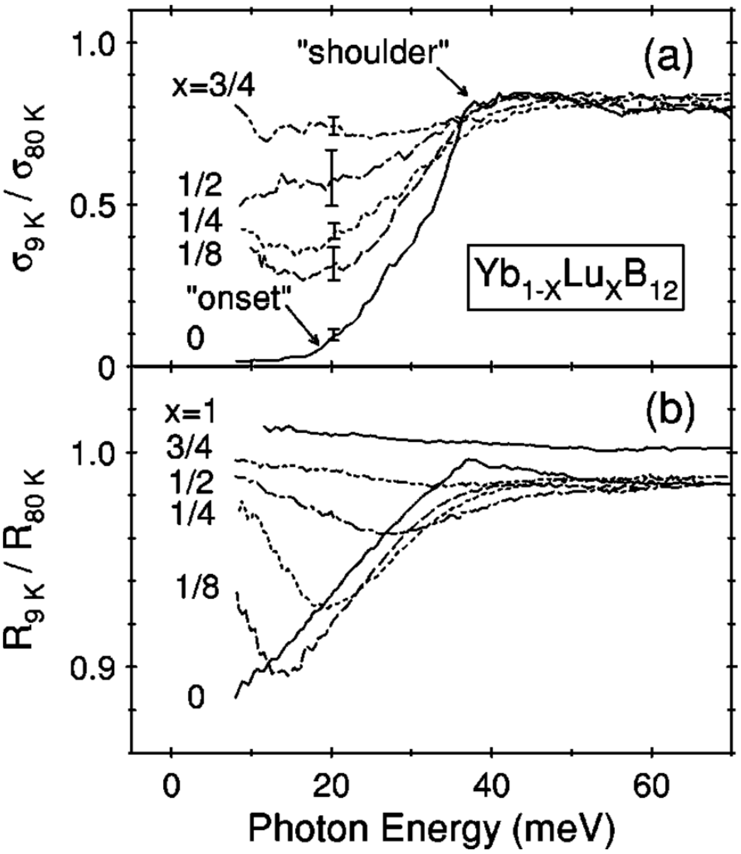

Fig.29: (a) Optical conductivity $\sigma(\omega, T)$ and (b) reflectivity of $\mathrm{Yb}_{1-x}\mathrm{Lu}_x\mathrm{B}_{12}$ at 9 K normalized by those at 80 K[57].

Y^{3+} (6-coordinated, 0.9Å) has a larger ionic radius than Yb^{3+} (6-coordinated, 0.868Å) and Lu^{3+} (6-coordinated, 0.861Å) ions, and a negative chemical pressure effect was expected. In fact, $\rho(T)$ is highly dependent on the valence of the substituted ion, and the temperature dependence of $\rho(T)$ of Lu, Y, and Sc are evaluated to be comparable at the same x[59], as shown in Fig. 30. In the case of Sc^{3+} (6-coordinated, 0.745Å) substitution, positive chemical pressure effect was also expected, but the substitution effect in $\rho(T)$ was comparable to that of the Y^{3+} substituted system. $\rho(T)$ of $Yb_{1-x}R_xB_{12}$ (R = Sc and Y) are shown in Fig. 31. This suggests that in nonmagnetic ion substituted alloys, the effect of valence difference on conduction and magnetism is larger than the chemical pressure effect due to the difference in ionic radius.

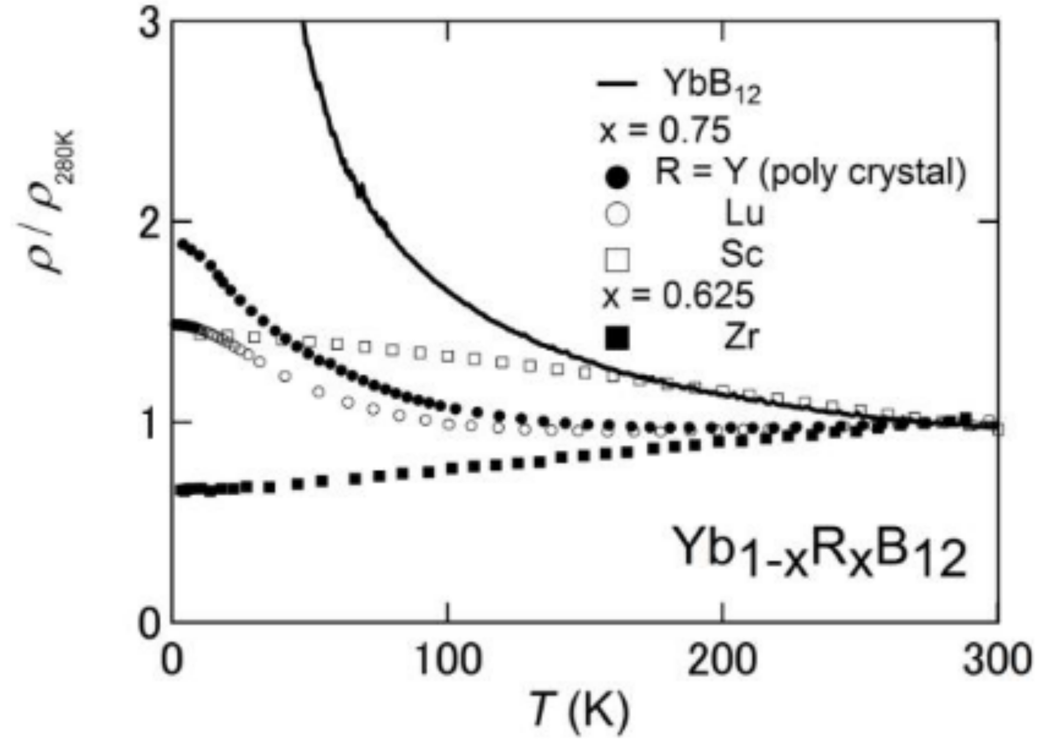

Fig.30: $\rho(T)$ for $Yb_{0.25}R_{0.75}B_{12}$ (R = Y, Lu, Sc, Zr) normalized at 280 K[59].

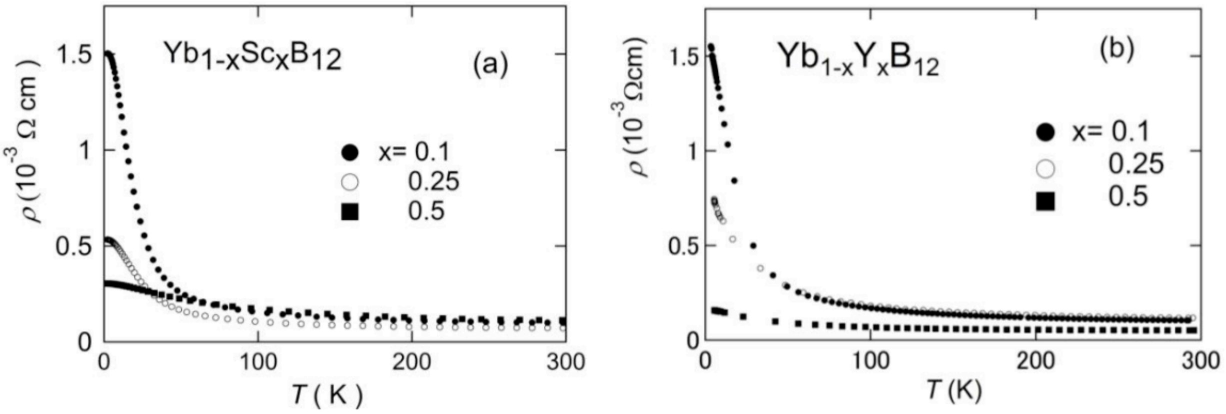

Fig.31: $\rho(T)$ for $Yb_{1-x}R_xB_{12}$ (R = Sc(a) and Y(b))[59].

On the other hand, $\rho(T)$ of the Zr^{4+} ion (6-coordinated, 0.73Å) substitution alloy decreases significantly, as shown in Fig. 30. Furthermore, the increase in T_{χ}^{max} was more rapid than that of the trivalent Lu and Y substitutions, indicating that the valence of the substituted ion has a significant effect not only on conduction but also on magnetism. In common with all substitution alloys, T_{χ}^{max} increases in the dilute region for $x > 0.5$, but it's extrapolation to $x = 0$ is found to be 25 K[60], independent of valence.

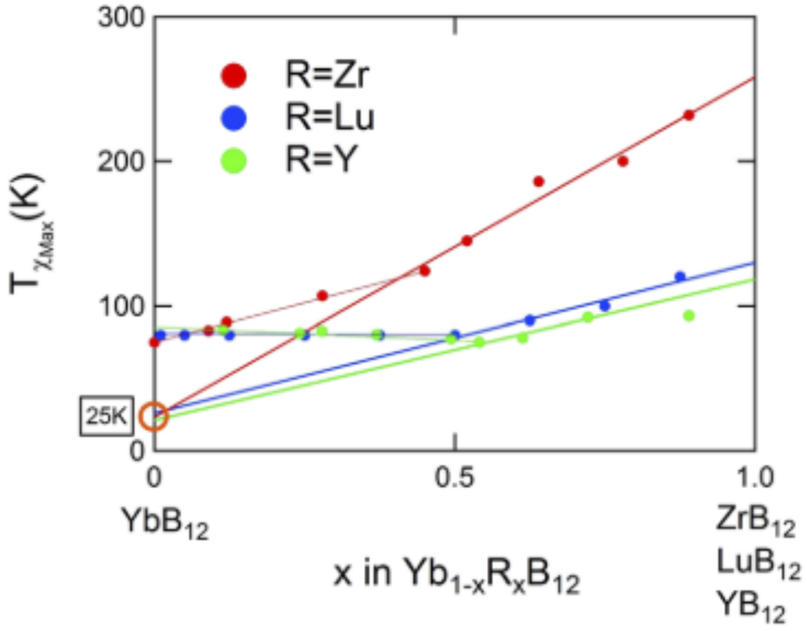

Fig.32: x-dependence of T_{χ}^{max} for $Yb_{1-x}R_xB_{12}$ (R = Zr, Lu, and Y)[60]. In this figure, x is the value determined experimentally by x-ray fluorescence analysis.

In the Lu-substituted alloys, the substitution of nonmagnetic trivalent Lu ions breaks the coherence of the Kondo singlet and forms the impurity band. *Tetravalent* Zr-substitution also breaks the coherence of the Kondo singlet but dopes one more electron than that in the case of Lu substitution. The results of bulk-sensitive hard X-ray photoemission spectroscopy (HAXPES) in Zr-substituted systems showed that the valence of Yb decreases with increasing Zr concentration[61]. The change in the valence of Yb is understood by the elevation of ϵ_{F}, that is, the decrease in excitation energy to the $4f^{14}$ band.

As mentioned above, the study of nonmagnetic ion-substituted alloys has led to a rough understanding of the transition between KM and KI, and the behavior of T_{χ}^{max}, a measure of T_{K}, has been shown to increase with substitution. The substitution of tetravalent Zr ions causes the energy gap to disappear rapidly, and the electrical resistivity shifts to a metallic temperature dependence, suggesting ϵ_{F} tuning effect. On the other hand, the origin of the increase in magnetic susceptibility and specific heat below 20 K is unclear, and there has been little discussion of the disappearance of ΔE_2^c and the mechanism of two-step energy gap formation.

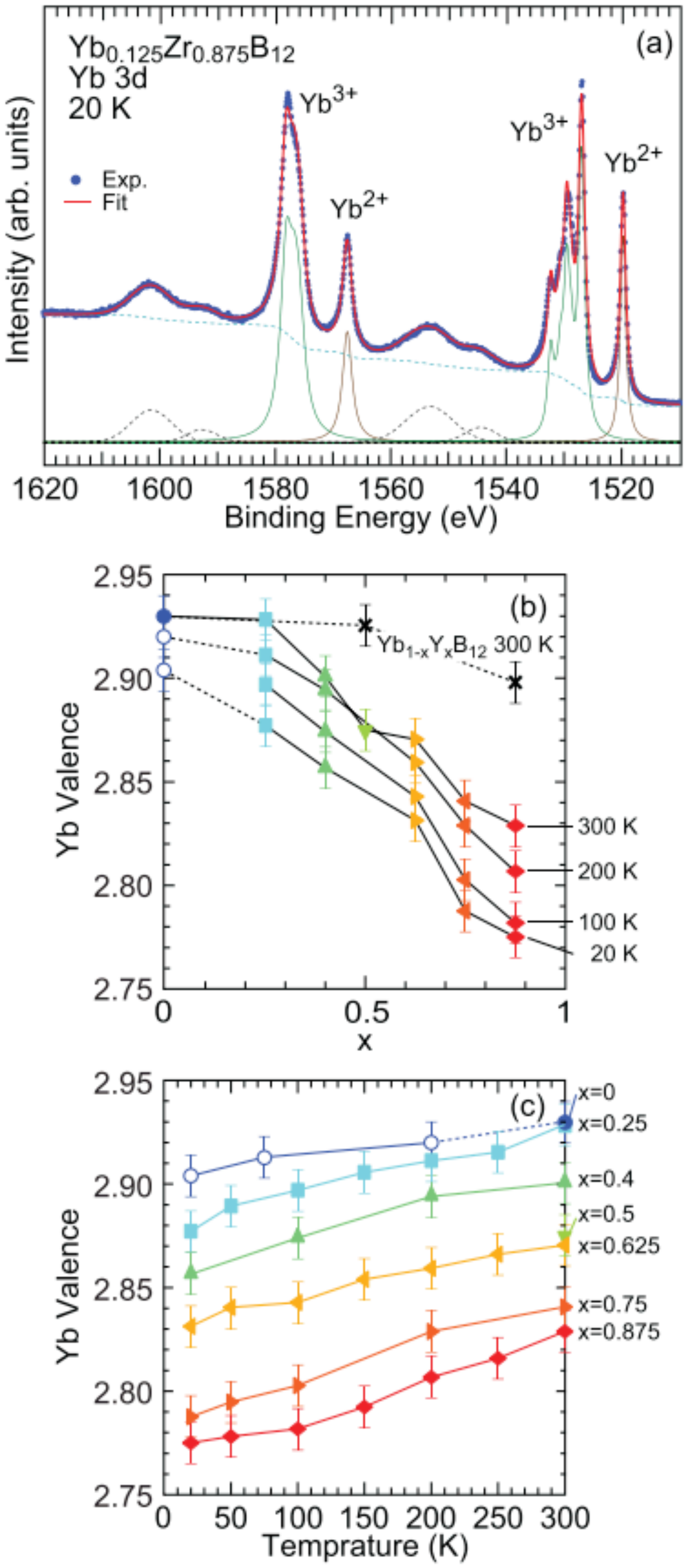

Fig.33: (a) Fit of Yb 3d HAXPES spectrum of $Yb_{0.125}Zr_{0.875}B_{12}$ measured at 20 K. (b) Yb valences of $Yb_{1-x}Zr_xB_{12}$ as a function of Zr concentration. For comparison, the results of $Yb_{1-x}Y_xB_{12}$ are plotted with crosses as a function of Y concentration. (c) Yb valences of $Yb_{1-x}Zr_xB_{12}$ as a function of temperature[61].

2 Purposes

The Kondo insulator (KI) at room temperature is a heavy fermion metal on the Doniach phase diagram, but at low temperature changes to strongly correlated insulator due to the temperature dependence of the c-f hybridization and coincidence of the orbital degeneracy numbers of conduction and $4f$- electrons.

Although interesting phenomena such as unconventional quantum oscillations, the appearance of a nontrivial surface state at low temperatures ($T < T_0$ =15 K), and valence fluctuations have been found in the KI YbB_{12}, the formation mechanisms of the *in-gap state* and *two-step energy gap structure* have not yet been clarified.

Schlottmann and Mutou have predicted the formation of in-gap state by substituted nonmagnetic ions or defects on rare-earth sites of KI. In the nonmagnetic ion-substituted alloy $\mathrm{Yb}_{1-x}\mathrm{R}_x\mathrm{B}_{12}$, the transition from KI to Kondo metal (KM) can be studied by controlling x. In fact, the existence of the in-gap state is suggested by the optical conductivity of $\mathrm{Yb}_{1-x}\mathrm{Lu}_x\mathrm{B}_{12}$. The collapse of ΔE_2^c, however, due to nonmagnetic ion substitution has not been noticed, its boundary concentration is unknown, and the relationship between the *in-gap state* and *two-step energy gap structure* has not been discussed up to now. Furthermore, the enhancements of magnetic susceptibility χ and specific heat divided by temperature C/T below 20 K in $\mathrm{Yb}_{1-x}\mathrm{R}_x\mathrm{B}_{12}$ by the impurity band are suggested by numerical calculations, but discussion of the enhancement in the experimental results is insufficient.

In this thesis, I investigate the growth of impurity bands in $\mathrm{Yb}_{1-x}\mathrm{R}_x\mathrm{B}_{12}$ and their effect for electrical conductivity σ $(= 1/\rho)$, χ and C/T to clear the origin of the *in-gap state* and the *two-step energy gap structure*. I also focused on R ion's valence dependence of the in-gap state and the boundary concentration where ΔE_2^c dissappearance in each substitutional system. In this study, polycrystalline divalent substituted alloy $\mathrm{Yb}_{1-x}\mathrm{Ca}_x^{2+}\mathrm{B}_{12}$ were prepared and compared with trivalent substituted alloy $\mathrm{Yb}_{1-x}\mathrm{Lu}_x^{3+}\mathrm{B}_{12}$, $\mathrm{Yb}_{1-x}\mathrm{Y}_x^{3+}\mathrm{B}_{12}$, and tetravalent substituted alloy $\mathrm{Yb}_{1-x}\mathrm{Zr}_x^{4+}\mathrm{B}_{12}$. In particular, I prepared some samples near critical x where ΔE_2^c disappears.

3 Sample preparation

3.1 Single crystal growth using traveling solvent floating zone method

I prepared samples of $\mathrm{YbB_{12}}$ with the non-magnetic ion substituted. In this thesis, I show experimental measurement data of $\mathrm{Yb_{1-x}R_xB_{12}}$ ($\mathrm{R} = \mathrm{Ca^{2+}}, \mathrm{Lu^{3+}}, \mathrm{Y^{3+}}$, and $\mathrm{Zr^{4+}}$). The x values are nominal for Ca-, Lu-, and Y-substituted alloys, and analysis value by X-ray Fluorescence analysis (XRF) for Zr-substituted alloys. For the growth of single crystals, the following two steps are used. First, polycrystalline samples for the growth of substituted single-crystal alloys were synthesized by high-frequency induction heating in vacuum. The reactions are as follows.

$$(1-x)\mathrm{Yb_2O_3} + x\mathrm{Lu_2O_3} + 27\mathrm{B} \rightarrow 2\mathrm{Yb_{1-x}Lu_xB_{12}} + 3\mathrm{BO}\uparrow \tag{16}$$

$$(1-x)\mathrm{Yb_2O_3} + x\mathrm{Y_2O_3} + 27\mathrm{B} \rightarrow 2\mathrm{Yb_{1-x}Y_xB_{12}} + 3\mathrm{BO}\uparrow \tag{17}$$

$$\begin{aligned}(1-x)\mathrm{Yb_2O_3} + 2x\mathrm{ZrO_2} + (27+x)\mathrm{B}\\ \rightarrow 2\mathrm{Yb_{1-x}Zr_xB_{12}} + (3+x)\mathrm{BO}\uparrow\end{aligned} \tag{18}$$

The mixed powder of these raw materials was isostatically pressed into rods of 8 mm diameter and 100 mm length. The pressed rods were set in a carbon cylinder heater with an inner boron nitride (BN) tube. Then, the carbon heater was set in a high-frequency induction coil with a quartz tube, which was pumped out for about 30 min until the vacuum level was of the order of 1 Pa. The magnetic field induced by the coil generated current in the carbon heater. Then, the sample space was heated by Joule heating.

The single crystallization step involved use of the traveling solvent floating zone (TSFZ) method[23] with an image furnace using four Xe lamps (Crystal Systems Inc.), as shown in Fig. 34. This method is applied to the single-crystal growth of incongruent melting materials. When melted YbB_{12} was cooled, YbB_6 and YbB_{66} also separated from the melted zone. Thus, I used a solvent with high B concentration (YbB_{12}+2B). Since no crucible is needed in the TSFZ method, there are no impurities from a crucible. By focusing light with an arc-spot size of about 6 mm ϕ from four Xe lamps, this furnace can generate a maximum temperature of 2800 °C. I set two sintered sample rods (feed and receiver) in the furnace along the sample rotation axis. The feed rod was hung by Mo wires on the upper side of the furnace. The receiver rod was placed on the lower side. I flowed Ar inert gas to avoid the adhesion of the rare-earth boride vapor to the quartz tube, as shown in Fig. 34.

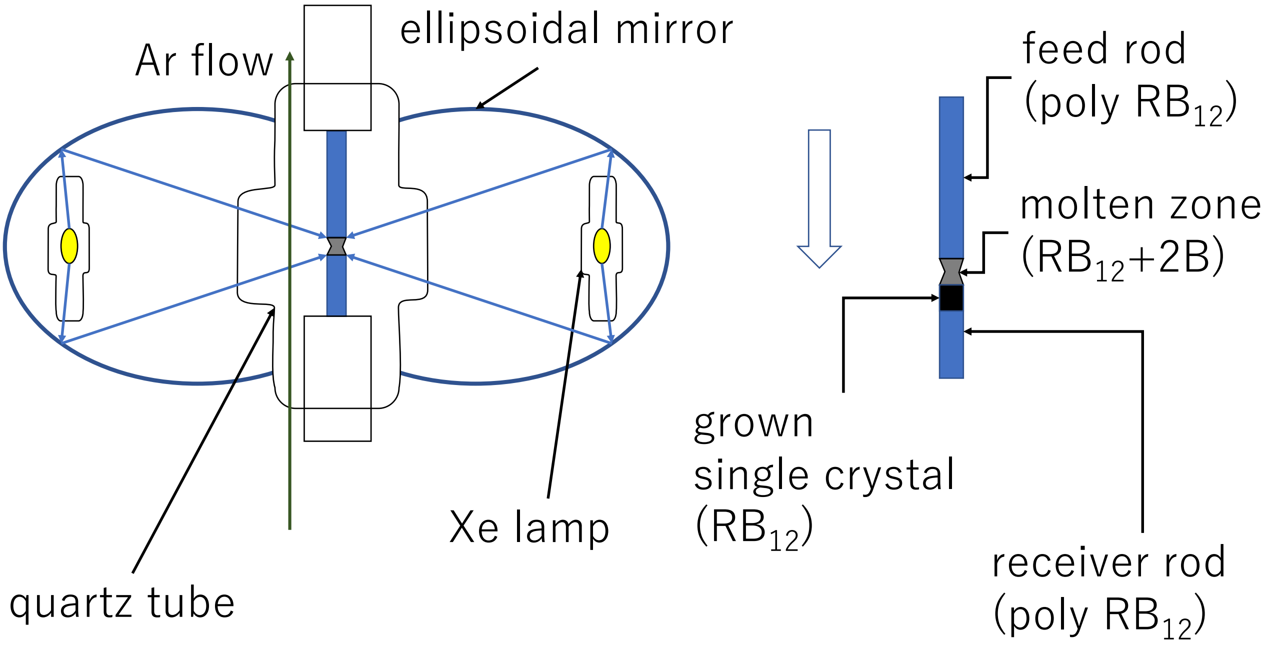

Fig.34: Side view of an image furnace. Polycrystalline rods are set on both the upper and lower sides of the furnace so that light spots of Xe lamps are focused on the molten zone between the upper and lower rods. The focused spot size of a Xe lamp is about 6–8 mm, and therefore a rod of this size is suitable for crystal growth by the floating zone method. Ar gas is flowed inside the quartz tube to eliminate evaporated rare-earth compounds.

3.2 High pressure synthesis using MaVo press

Divalent Ca-substituted samples cannot be synthesized at atmospheric pressure because the Ca ionic radius is larger than the Yb ionic one. Thus, I synthesized polycrystalline $Yb_{1-x}Ca_xB_{12}$ by high-pressure synthesis according to eq. (19). High pressure of 12–18 GPa for the synthesis of $Yb_{1-x}Ca_xB_{12}$ was generated by MaVo press equipment (Max Voggenreiter Co.), as shown in Fig. 35. In a multi-anvil 6-8 system, uniaxial pressure is transmitted to the six first-stage anvils which press eight second-stage anvils forming a cubic cell. At the center of the cubic cell (second-stage anvils), I placed a Cr-containing MgO octahedral pressure medium, where the sample and Joule heater were set. The Joule heat generated by the $(\mathrm{La, Sr})\mathrm{CrO_3}$ heater enveloping a BN cell was used for the reaction. Powder raw materials, YbB_{12}, CaB_6, and 6B, were sealed in a BN cell.

$$(1-x)\mathrm{YbB_{12}} + x\mathrm{CaB_6} + 6x\mathrm{B} \rightarrow \mathrm{Yb_{1-x}Ca_xB_{12}} \tag{19}$$

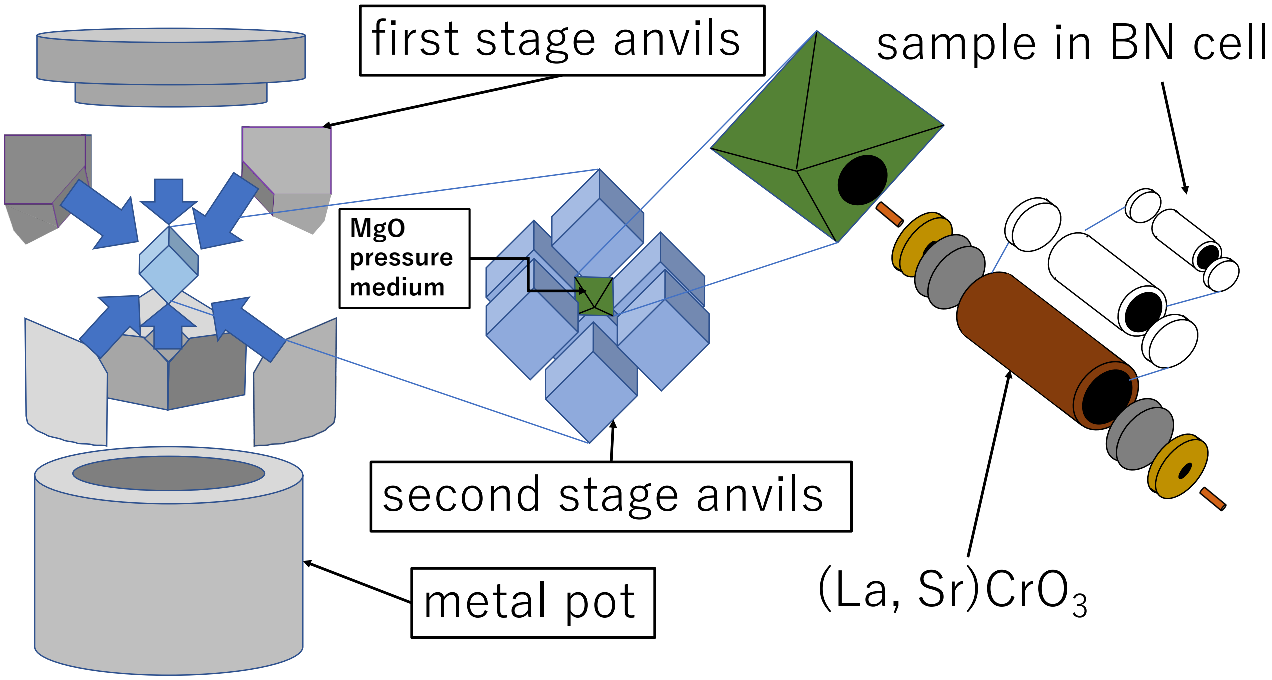

Fig.35: Schematic of the multi-anvil 6-8 system (Kawai-type apparatus) used to synthesize polycrystalline $Yb_{1-x}Ca_xB_{12}$. MaVo press equipment for high-pressure synthesis can generate up to 1000 tons of hydraulic pressure. The load is applied to the second-stage anvils at the center through first-stage anvils (Walker module) placed inside a metal pot. The eight second-stage anvils pressurize the central sample cell from eight directions to realize pseudo-isotropic pressure. $(La, Sr)CrO_3$ heaters are used to generate the high temperature for the reaction. A BN sample cell is used because of its inertness reaction with the sample.

4 Experimental methods

4.1 Electrical resistivity

Electrical resistivity measurements were performed by a conventional four-probe DC method using quantum design physical property measurement system (PPMS) in the temperature range from 1.8 K (or 0.4 K for only $\mathrm{YbB_{12}}$) to 300 K. Electrical resistivity is measured in four-probe method by applying a constant current between I terminals located on outsides, and measuring potential difference between V terminals located on inside.

$$R = \frac{V}{I} \tag{20}$$

$$\rho = R\frac{s}{l} \tag{21}$$

Resistance value is obtained by (20), and electrical resistivity ρ is obtained by dividing electrical resistance value R by length l between V terminals and multiplying by cross-sectional area s.

4.2 Specific heat

The specific heat was also measured by the thermal relaxation method using PPMS.

The specific heat $C(T)$ can be obtained using the heat flow Q into the sample and the small change in temperature dT as follows

$$Q = C(T)dT \tag{22}$$

$$C(T) = \frac{dQ}{dT} \tag{23}$$

The measurement is based on the thermal relaxation method.

$$Q = -\kappa\Delta T \tag{24}$$

A heating heater is used to heat the sample to the maximum temperature T_H in a given temperature range, and then the heater is stopped. Next, the sample temperature T is then measured versus time until the temperature of the sample reaches the temperature of the heat bath T_L.

$$\tau = \frac{T_L - T_H}{\Delta t} = \frac{dT}{dt} \tag{25}$$

The relaxation time depends on the material and temperature as well as the specific heat. In addition, the specific heat can be obtained by calculating the time variation of heat flow, $\frac{dQ}{dt}$, from the thermal conductivity of the material used in the thermal contact as follows

$$C = \frac{\frac{dQ}{dt}}{\tau} = \frac{dQ}{dT} \tag{26}$$

Therefore, what is needed for the measurement is the thermal conductivity of the heat-contacting material κ and the sample-derived relaxation time τ. However, the above method is a simple model with only the sample, the thermal contact material, and the heat bath, and it does not separate the thermal relaxation of the material used for the sample holder from that of the sample. In the actual measurement, the sample holder and the apiezone-N grease used for the thermal contact are combined to form a 1τ model (the model described above), and the thermal relaxation measurement is performed. To correctly measure the thermal relaxation of the sample only, the measurement is performed using a 2τ model, and the thermal relaxation is subtracted as background.

4.3 Magnetic susceptibility

Magnetic susceptibility measurements have been done by Quantum design magnetic property measurement system (MPMS) with the Superconducting quantum interference device (SQUID) magnetometer from 2 to 300 K under 1 T.

4.3.1 Josephson effect

A device with two superconductors (1 and 2) and an insulator between them is called a Josephson junction. When the insulator is sufficiently thin under zero magnetic and electric fields, the current flowing in the junction depends on the phase difference of the wave functions of the superconductors and is shown as follows:

$$J = J_0 \sin\delta = J_0 \sin(\theta_2 - \theta_1). \tag{27}$$

In this case, a constant current that depends on the phase difference flows, and this is called the DC Josephson effect. On the other hand, when an electric field is applied, it oscillates at a frequency ($\omega = \frac{2eV}{\hbar}$) that depends on the electric field, as shown below, and this is called AC Josephson effect.

$$J = J_0 \sin(\delta - \frac{2eV}{\hbar}t) \tag{28}$$

4.3.2 SQUID magnetometor

A magnetic probe called superconducting quantum interferometer exists as an application of the Josephson effect. Consider a closed circuit (superconducting quantum interference device (SQUID)) containing two Josephson junctions. The total magnetic flux passing through superconducting ring is quantized, and following relationship between total flux Φ and total phase difference δ_{tot} is established.

$$\delta_{tot} = \frac{2e}{\hbar}\Phi. \tag{29}$$

Assuming that the phase difference at each Josephson junction is δ_1 and δ_2, δ_{tot} can be written as

$$\delta_{tot} = \delta_2 - \delta_1 = \frac{2e}{\hbar}\Phi. \tag{30}$$

It can also be written as follows.

$$\delta_2 = \delta_0 - \frac{e}{\hbar}\Phi,\ \delta_1 = \delta_0 + \frac{e}{\hbar}\Phi \tag{31}$$

Since the total current is expressed as the sum of the currents through each junction, it depends on the magnetic flux through the loop as follows:

$$J_{total} = J_0(\sin(\delta_0 + \frac{e}{\hbar}) + \sin(\delta_0 - \frac{e}{\hbar})) = 2(J_0 \sin\delta_0)\cos\frac{e\Phi}{\hbar}. \qquad (32)$$

By measuring the magnitude of the current flowing through the SQUID, Φ through the device can be measured with high sensitivity. Since the SQUID device needs to be kept in a superconducting state, magnetic flux around sample is observed by a magnetic transformer called a pickup coil. The pickup coil is set at a region 15 mm above and below the measurement center, and can eliminate noise associated with a uniform magnetic field change in the space around the sample.

5 Results

5.1 Electrical conductivity $\sigma(T)=\frac{1}{\rho\,(T)}$

First, temperature dependence of electrical resistivity $\rho\,(T)$ of $\mathrm{Yb}_{1-x}\mathrm{R}_x\mathrm{B}_{12}$ ($\mathrm{R}=\mathrm{Ca}^{2+}$, Lu^{3+} and Zr^{4+}) is shown in Fig. 36, 37, 38, respectively. Next, temperature dependence of ratio of electrical conductivity to 300 K ($\sigma(T)\ /\ \sigma(300\,\mathrm{K})$) of $\mathrm{Yb}_{1-x}\mathrm{R}_x\mathrm{B}_{12}$ ($\mathrm{R}=\mathrm{Ca}^{2+}$, Lu^{3+} and Zr^{4+}) is shown in Fig. 39(a), 39(b) and 39(c), respectively. Electrical resistivity $\rho\,(T)$ is shown as electrical conductivity $\sigma(T)=1/\rho\,(T)$ to discuss the effect of the impurity band formation on electrical conductivity $\sigma(T)$ as well as on optical conductivity $\sigma(\omega,\,T)$. The $x=0$ data in each figure corresponds to $\sigma(T)$ of a single crystal of YbB_{12}. $\sigma(T)$ of YbB_{12} decreases significantly below 100 K owing to the gradual opening of an energy gap, and the ratio $\sigma(T)\ /\ \sigma(300\,\mathrm{K})$ is more than five orders of magnitude at 2 K. Despite the presence of the energy gap, $\sigma\,(T)$ is almost constant below 3 K, indicating metallic conduction.

The temperature dependence of $\sigma(T)\ /\ \sigma(300\ \mathrm{K})$ becomes metallic, as x and the valence of the substituted ion increase. In the Lu ($0.5 < x < 0.75$) and Zr ($0.15 < x < 0.25$)-substituted systems, the conduction changes to the Kondo metal(KM) as x increases. Thus, the boundary concentration between KM and Kondo insulator(KI) shifts to the lower-x side as the valence of the substituted ion increases. Furthermore, the conduction of the Zr-rich sample ($0.25 < x$) changes to metallic without -log$T$ dependence, and the Kondo effect seems to be smeared out by doped carriers, as shown in Fig. 38 for $x=0.5$ and 0.625. $\sigma(T)\ /\ \sigma(300\,\mathrm{K})$ of each alloy tends to increase with x in the ΔE_1^c-dominant temperature region ($T_0 = 15$ K $< T <$ 40 K). The trend is especially marked in the ΔE_2^c-dominant region ($T < T_0$), suggesting that ΔE_2^c is more substitution-sensitive than ΔE_1^c. These x dependences of $\sigma(T)$ / $\sigma(300\,\mathrm{K})$ below T_0 may indicate that ΔE_2^c is filled by Kondo holes[51] as shown for the optical conductivity $\sigma(\omega, T)$[57, 58].

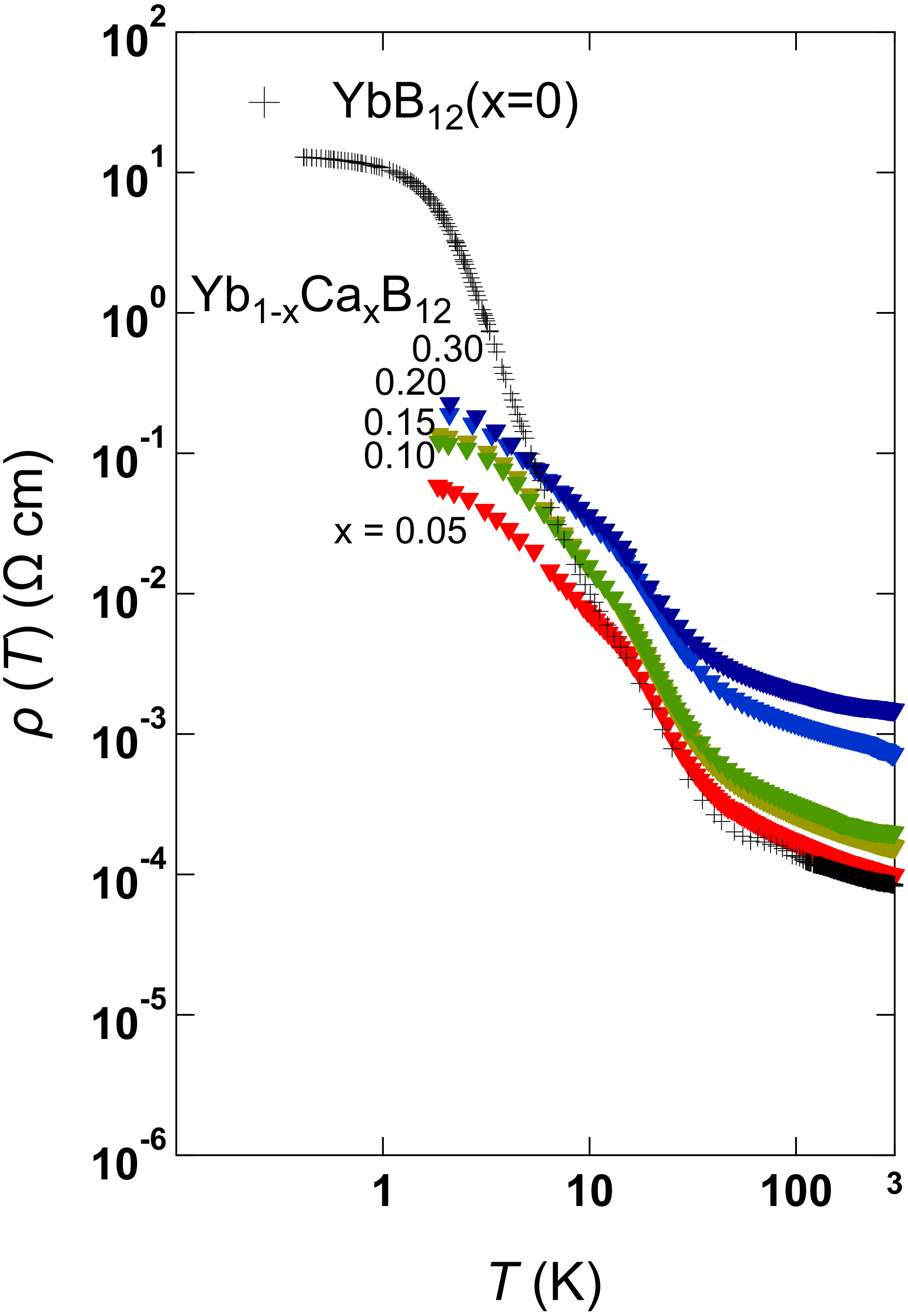

Fig.36: Temperature dependence of $\rho\,(T)$ of $\mathrm{Yb}_{1-x}\mathrm{Ca}_x\mathrm{B}_{12}$

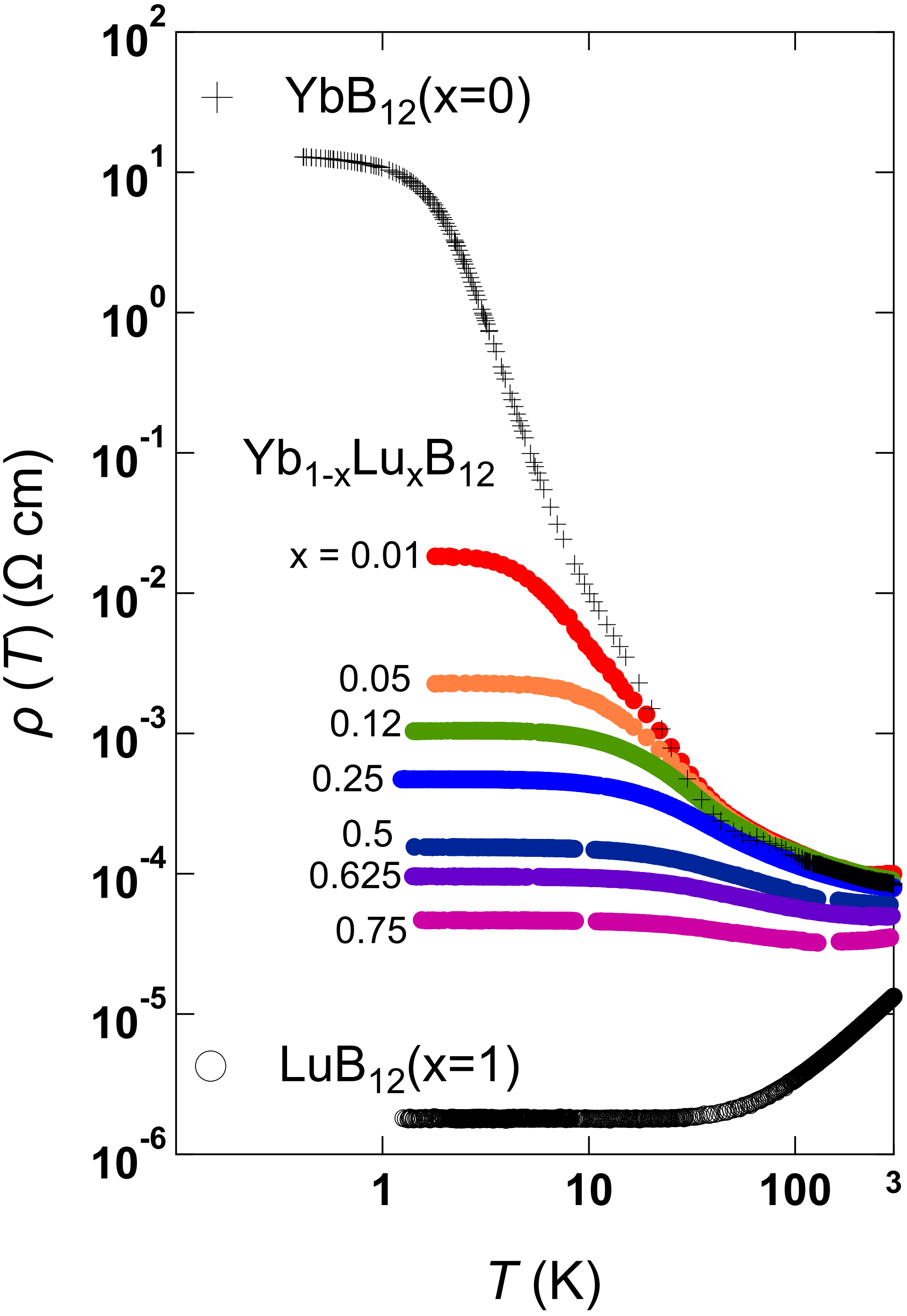

Fig.37: Temperature dependence of $\rho\,(T)$ of $\mathrm{Yb}_{1-x}\mathrm{Lu}_x\mathrm{B}_{12}$

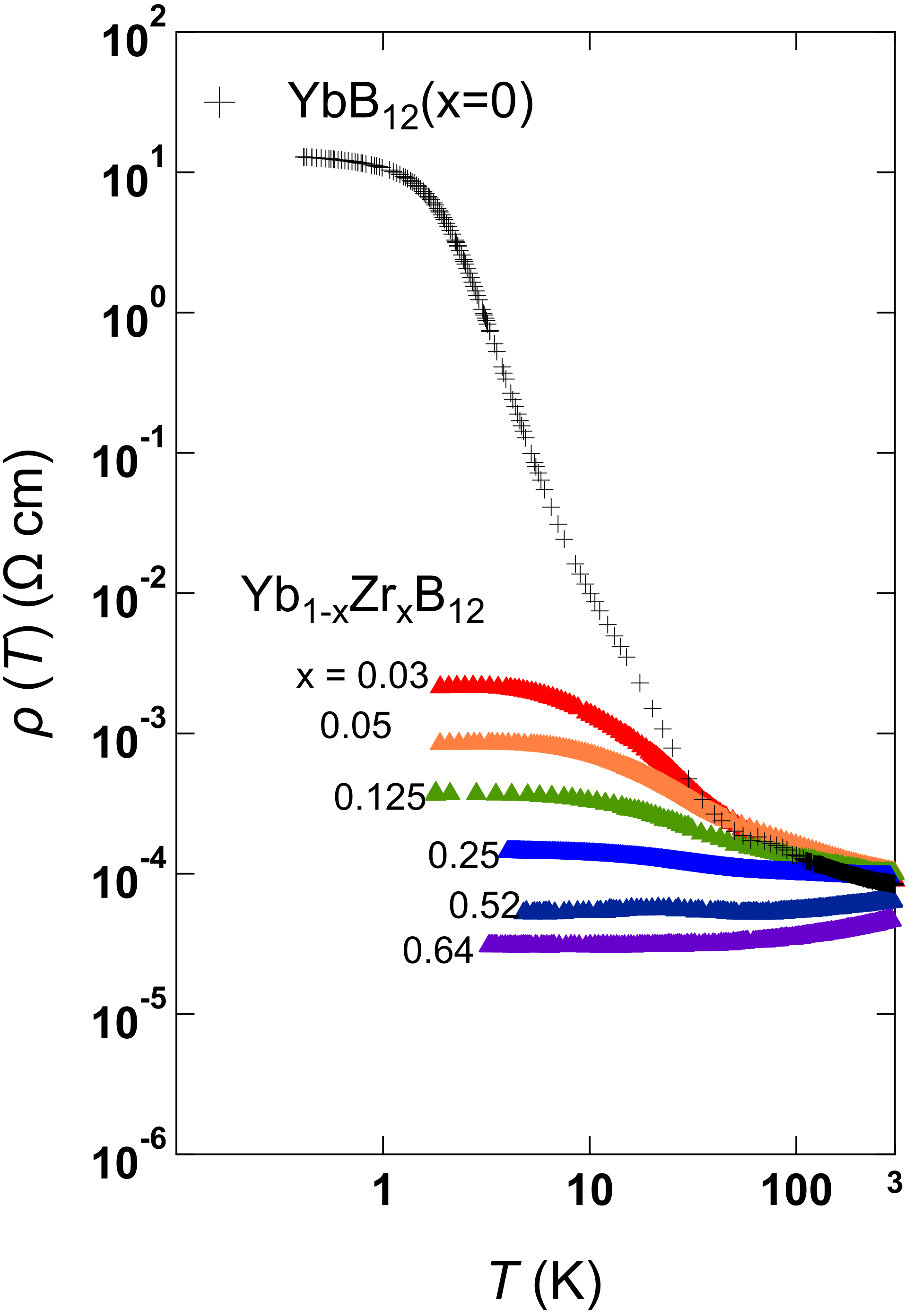

Fig.38: Temperature dependence of $\rho\,(T)$ of $\mathrm{Yb}_{1-x}\mathrm{Zr}_x\mathrm{B}_{12}$

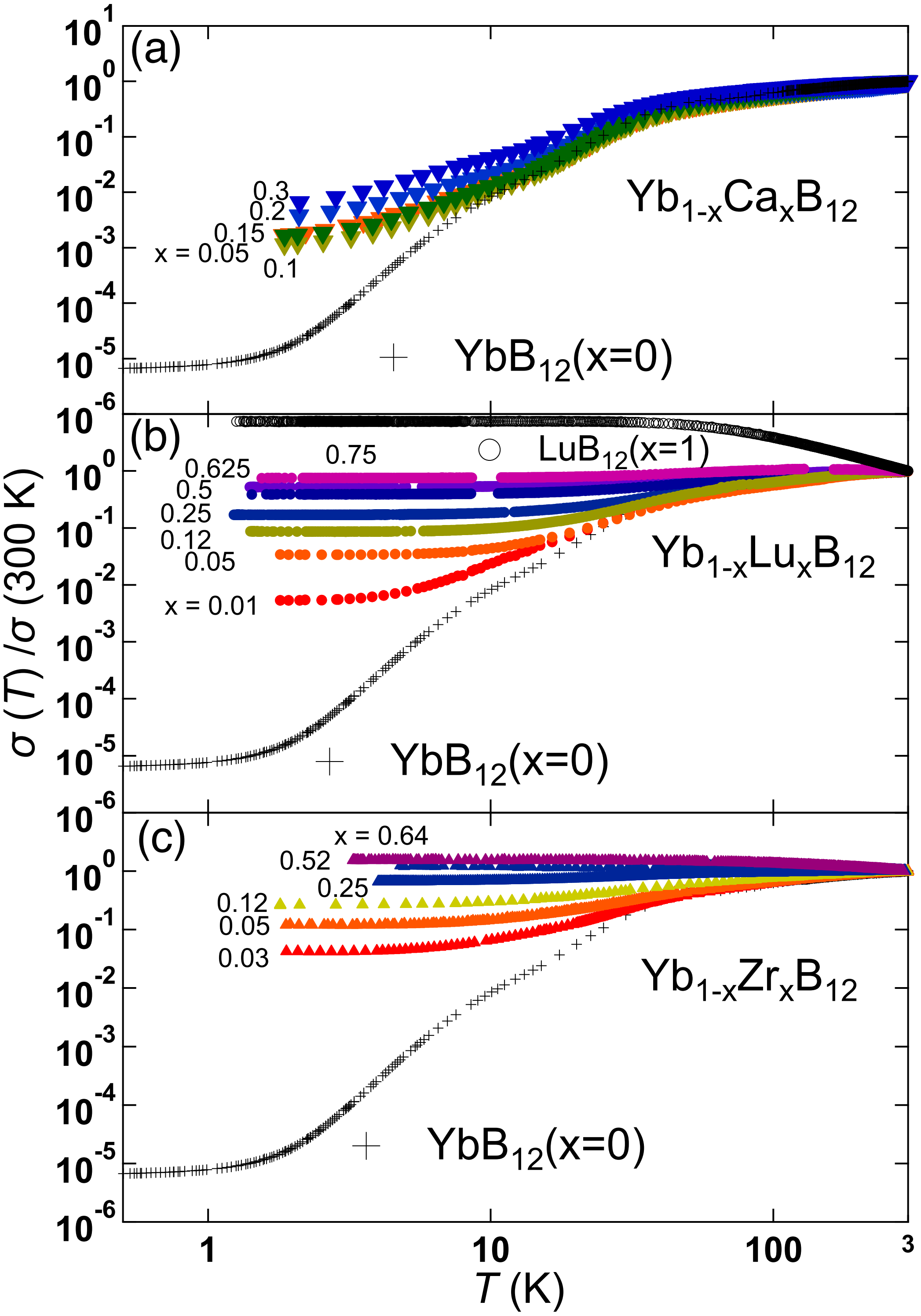

Fig.39: Temperature dependence of ratio of electrical conductivity $\sigma(T)$ / $\sigma(300\text{ K})$ for $\mathrm{Yb}_{1-x}\mathrm{R}_x\mathrm{B}_{12}$ ($\mathrm{R} = \mathrm{Ca}^{2+}$(a), Lu^{3+}(b), and Zr^{4+}(c)). $\sigma(T)$ / $\sigma(300\text{ K})$ of all substituted alloys tends to increase with x.

5.2 Specific heat divided by temperature C/T

The temperature dependence of specific heat divided by temperature C/T of $\mathrm{Yb}_{1-x}\mathrm{R}_x\mathrm{B}_{12}$ ($\mathrm{R} = \mathrm{Ca}^{2+}$, Lu^{3+}, and Zr^{4+}) is shown in Fig. 40. Generally, the spin gap E_g^s is evaluated from the magnetic heat capacity C_{mag}. However, the total heat capacity C is evaluated in this study because the lattice contribution to the heat capacity of $\mathrm{Yb}_{1-x}\mathrm{R}_x\mathrm{B}_{12}$ ($x \neq 0$) cannot be accurately subtracted. For YbB_{12}, the shoulder structure in C/T at 33 K can be interpreted as a Schottky peak, and the spin gap ΔE^s is evaluated to be 70 K[56]. This value is comparable to ΔE_1^c obtained from the electrical resistivity. This evaluation for only YbB_{12} is based on a simple model in which the lattice contribution to the heat capacity is estimated by multiplying the heat capacity of LuB_{12} by a factor to adjust S_{mag} to $0.9R\ln 4$ at 300 K[56].

Similarly to $\sigma(T)$, the nonmagnetic ion substitution effect for C/T can be divided into gradual x dependence in the ΔE_1^c-dominant temperature region ($T_0 < x < 100$ K) and steep x dependence in the ΔE_2^c-dominant temperature region ($T < T_0$). Similar to that in previous studies[56, 55], the shoulder of C/T around 33 K gradually decreases as the Lu concentration increases as shown in Fig. 40(a). The shoulder structure is almost invariant with Ca substitution [Fig. 40(a)], while the Zr-substituted alloys showed an x-sensitive decrease in the shoulder structure compared with the Lu-substituted alloys as shown in Fig. 40(b). This behavior is qualitatively consistent with the gradual collapse of ΔE_1^c with substitution, as seen for $\sigma(T)$. C/T of YbB_{12} shows a second shoulder at 6 K, which is lower than the shoulder at 33 K. In $\mathrm{Yb}_{1-x}\mathrm{R}_x\mathrm{B}_{12}$, the shoulder structure at 6 K disappears and C/T increases as -log$T$ below 10 K. The origin of the second shoulder is unclear. Furthermore, C/T of YbB_{12} shows -log$T$ behavior below 1 K. This temperature is lower than that seen in the substituted alloys.

C/T(2 K) of $\mathrm{Yb}_{1-x}\mathrm{R}_x\mathrm{B}_{12}$ (R = Ca^{2+}, Lu^{3+}, and Zr^{4+}) has a peak around $x = 0.1$ as shown in Fig. 41. I define this substitution rate at the peak of C/T(2 K) as $x_0 = 0.1$. This x-dependent enhancement has been numerically calculated by Mutou using the Kondo lattice model[52, 53]. This peak seems to be due to a combination of dilution of the Yb ion and enhancement by the Kondo impurity band (KIB), which is discussed later.

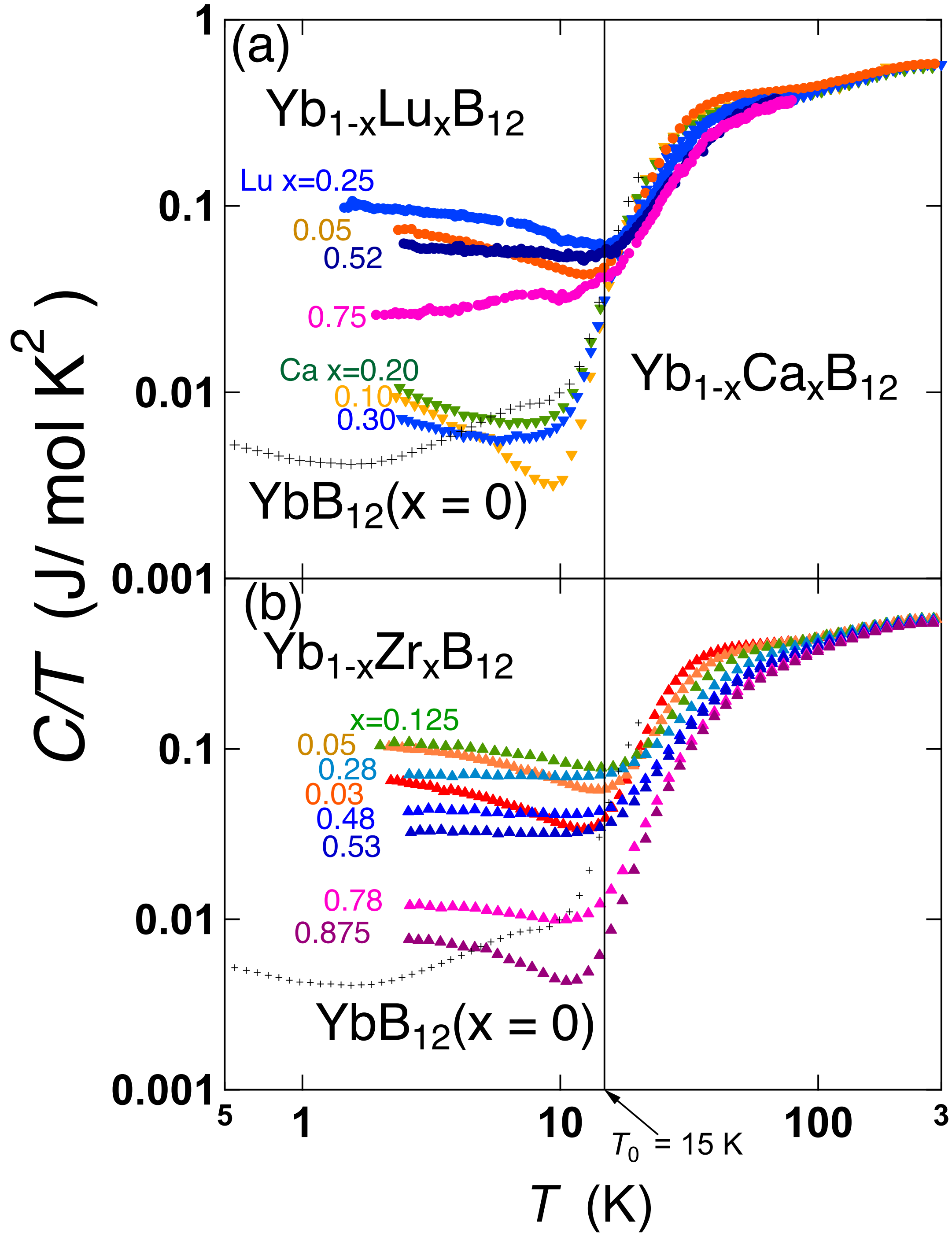

Fig.40: Temperature dependence of specific heat divided by temperature C/T of $\mathrm{Yb}_{1-x}\mathrm{R}_x\mathrm{B}_{12}$ ($\mathrm{R} = \mathrm{Ca}^{2+}$(a), Lu^{3+}(a), and Zr^{4+}(b)). In (a), the data of x = 0.25, 0.52, and 0.75 for R = Lu are from Ref. 56. The shoulder around 33 K corresponds to the formation of ΔE^s and decreases as x increases. T_0 is a special value common to (a) and (b). In the ΔE_2^c-dominant temperature region ($T < T_0$) , C/T's of the samples increase with $x < 0.1$, while C/T's of the samples decrease as x increases for $x > 0.1$.

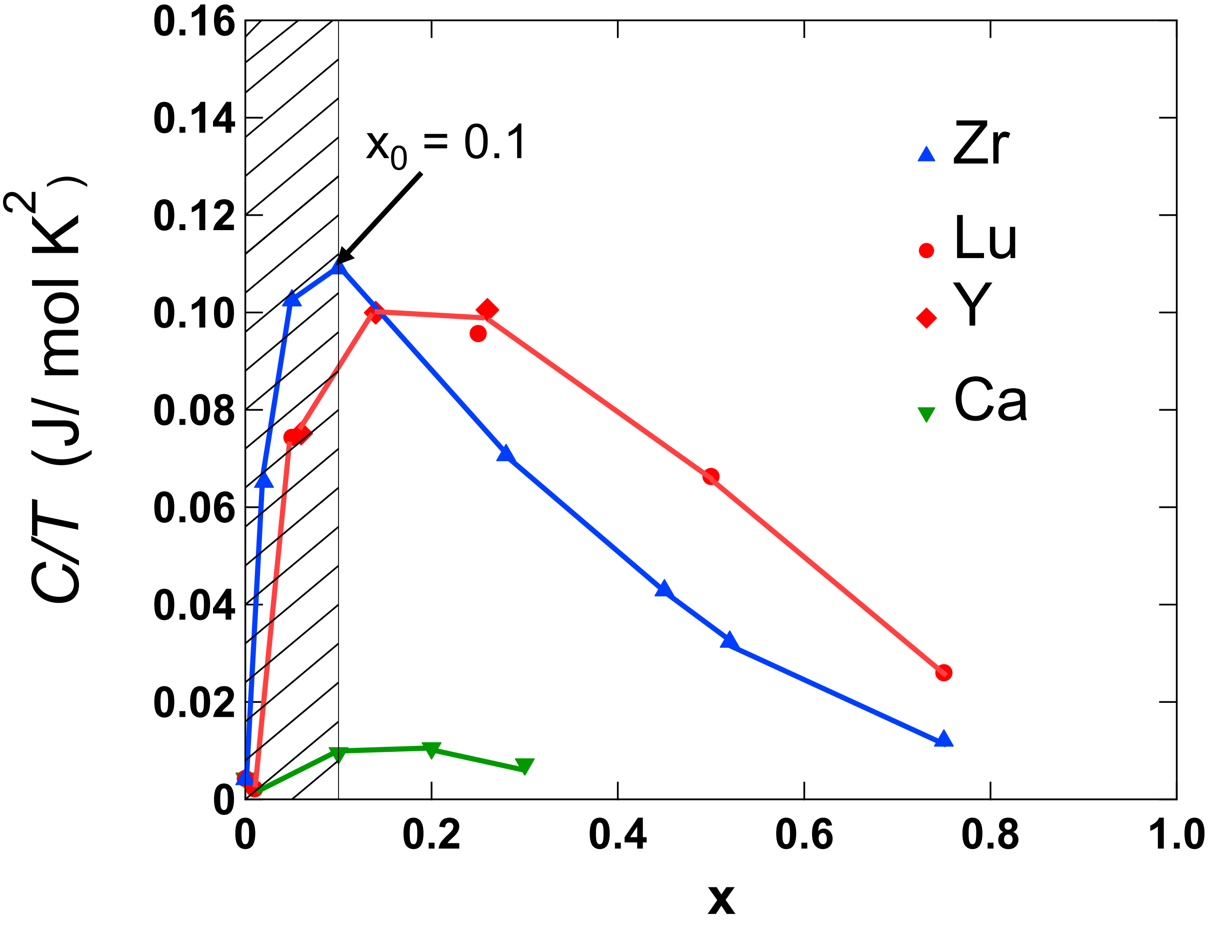

Fig.41: x dependence of C/T at 2 K. $C/T(2\text{ K})$ of $\mathrm{Yb}_{1-x}\mathrm{R}_x\mathrm{B}_{12}$ ($\mathrm{R} = \mathrm{Ca}^{2+}$, Lu^{3+}, Y^{3+}, and Zr^{4+}) shows a peak at around $x_0 = 0.1$. C/T in the ΔE_2^c-dominant temperature region ($T < T_0$) is enhanced for $x < 0.1$ by the formation of the Kondo impurity band (KIB) state, as seen for $\sigma\,(T)$, which is discussed later.

5.3 Magnetic susceptibility χ

In Fig. 42, the magnetic susceptibility χ of $\mathrm{Yb}_{1-x}\mathrm{R}_x\mathrm{B}_{12}$ ($\mathrm{R} = \mathrm{Ca}^{2+}$, Lu^{3+}, and Zr^{4+}) is shown as a function of T, where the data for $x = 0$ shows $\chi\,(T)$ of a single crystal of YbB_{12}. $\chi\,(T)$ of YbB_{12} behaves according to the Curie–Weiss law above 250 K, decreases to $1\,/\,3$ of the peak value at 80 K due to energy gap formation, and finally becomes almost constant below 20 K. This constant value has been considered to be associated with the Van Vleck susceptibility. In the case of nonmagnetic ion substitution, Yb ion dilution and screening effects induced by surplus conduction electrons appear in the x dependence of $\chi\,(300\,\mathrm{K})$ of $\mathrm{Yb}_{1-x}\mathrm{R}_x\mathrm{B}_{12}$. In the trivalent Lu-substituted alloy, the absolute value decreases with the dilution of Yb as shown in Fig. 42(b). $\chi\,(300\,\mathrm{K})$ of the tetravalent Zr-substituted alloy [Fig. 42(c)] decreases more rapidly than that of the Lu-substituted alloy. On the other hand, for the divalent Ca-substituted alloy, $\chi\,(300\,\mathrm{K})$ per Yb is almost constant. In previous reports for R = Lu and Zr, I showed that T_χ^{max} , the peak temperature of $\chi\,(T)$, increases with x and the valence of the substituted ions for $x > 0.5$[59, 60]. As mentioned for electrical conductivity $\sigma\,(T)$, the conduction of the samples is metallic in the Lu-substituted ($x > 0.5$) and the Zr-substituted ($x > 0.25$) systems. In particular, the increase in T_χ^{max} is greater in the tetravalent Zr-substituted ($x = 0.89$, $T_\chi^{max} = 230$ K) system than in the trivalent Lu-substituted ($x = 0.875$, $T_\chi^{max} = 110$ K) and Y-substituted ($x = 0.89$, $T_\chi^{max} = 90$ K)[60] systems. T_χ^{max} increases linearly with x in the Yb dilute region ($x > 0.5$), and extrapolation from the high-x region to $x = 0$ gives $T_\chi^{max} = 25$ K[60]. This suggests that if YbB_{12} does not become a Kondo insulator, T_χ^{max} may be about 25 K. In the Kondo impurity model with degeneracy of ground state $N = 4$, T_K is proportional to $3\,T_\chi^{max}$[62], and in the Yb dilute region, T_K may increase owing to the collapse of the coherence of the Kondo singlet. Similarly to C/T, $\chi\,(T)$ also increases with decreasing temperature below 20 K. The x dependence of $\chi(2\,\mathrm{K})$ also shows a peak around x_0 as shown in Fig. 43. $C/T(2\ \mathrm{K})$ of the Ca alloy, which is considered to have a small number of carriers, is one order of magnitude smaller than that of the Lu-substituted and Zr-substituted systems, but $\chi(2\,\mathrm{K})$ is comparable to that of the Lu-substituted and Zr-substituted alloys.

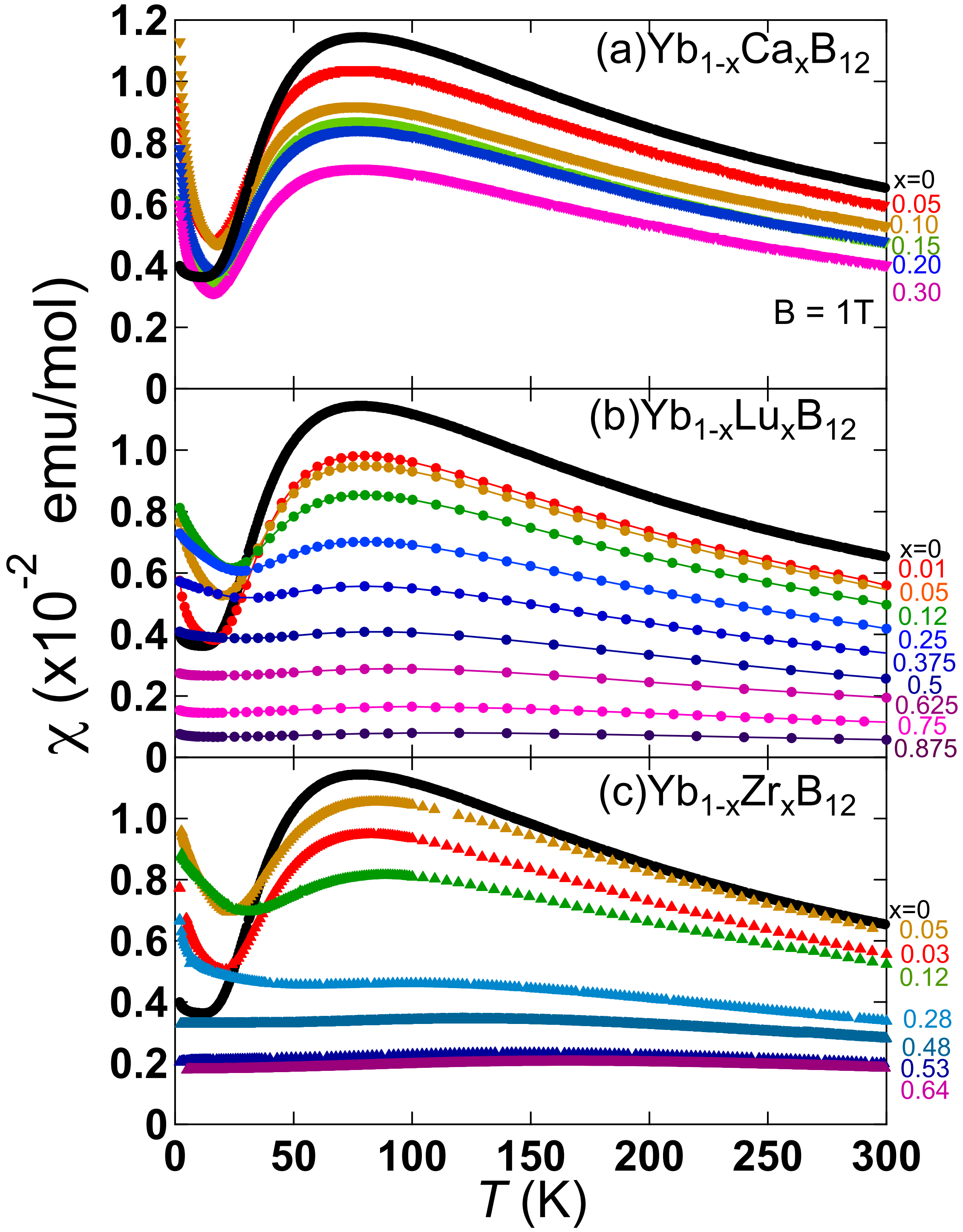

Fig.42: Magnetic susceptibility $\chi\,(T)$ of $\mathrm{Yb}_{1-x}\mathrm{R}_x\mathrm{B}_{12}$ (R $=$ Ca^{2+}(a), Lu^{3+}(b), and Zr^{4+}(c)). $\chi\,(T)$ was measured by a SQUID magnetometer to investigate the nonmagnetic substitution effect of YbB_{12}. All measurements were performed at 1 T. The decreasing trend of $\chi\,(T)$ with Yb dilution is indicated by absolute values at 300 K. Peak temperature T_{χ}^{max} tends to increase with increasing x for $x > 0.5$ and shows Curie–Weiss-like temperature dependence below 20 K.

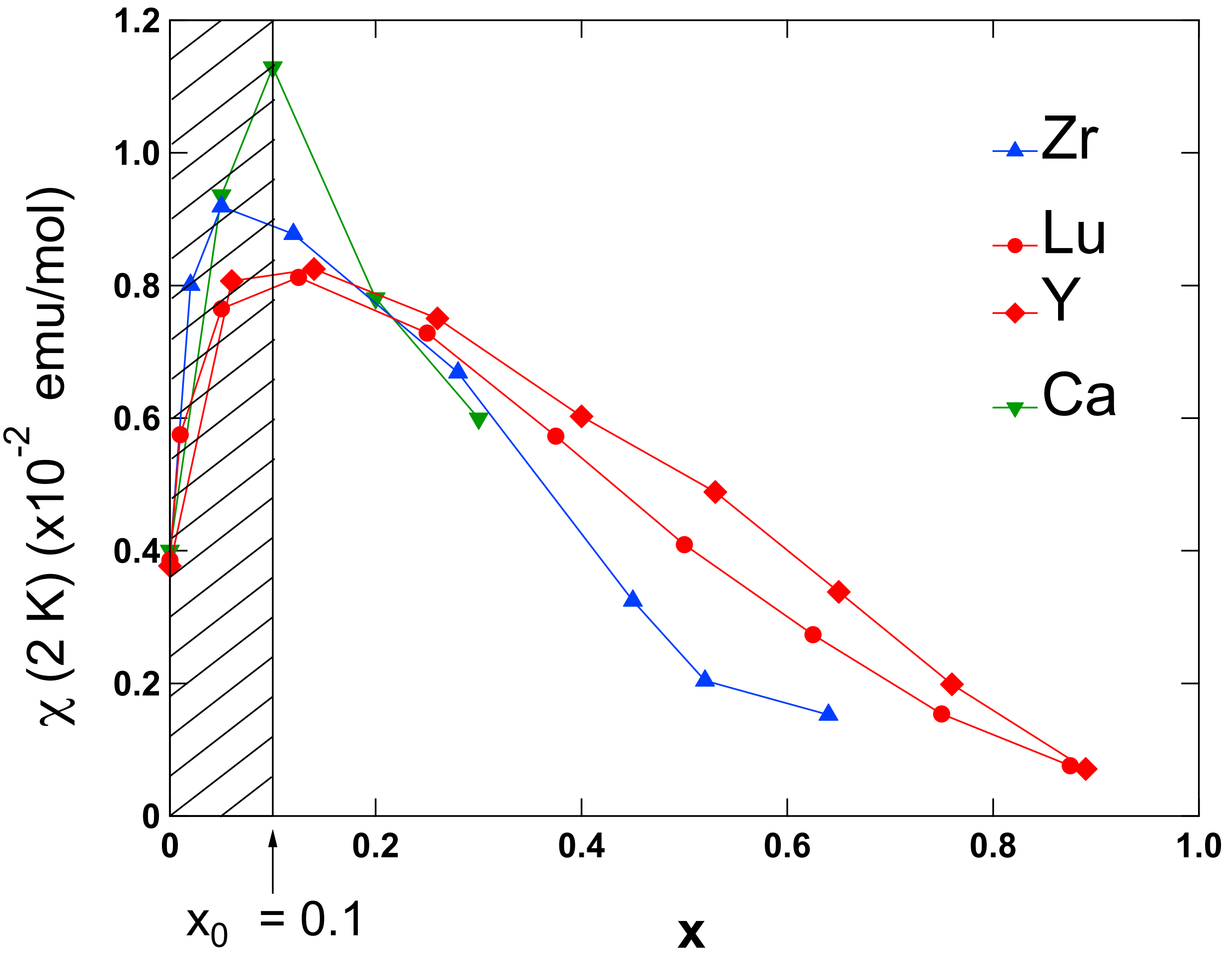

Fig.43: x dependence of $\chi(2\,\mathrm{K})$. Despite nonmagnetic ion substitution, $\chi(2\,\mathrm{K})$ of $\mathrm{Yb}_{1-x}\mathrm{R}_x\mathrm{B}_{12}$ ($\mathrm{R} = \mathrm{Ca}^{2+}$, Lu^{3+}, Y^{3+}, and Zr^{4+}) shows a peak near $x = x_0$ as seen for C/T.

6 Discussion

6.1 Enhancement of σ, χ and C/T below $T_0 = 15$ K

In this section, I discuss the sensitive substitution effect in the ΔE_2^c-dominant temperature region ($T < T_0$) and the insensitive one in the ΔE_1^c-dominant region ($T_0 < T$). First, I evaluate these thermally activated energies according to the following equation.

$$\rho = \rho_0 \exp \frac{\Delta E}{T} \tag{33}$$

Taking the logarithm of both sides, I get the following equation. This plot of logarithmic electrical resistivity ρ as a function of $1/T$ is called an Arrhenius plot. If the size of energy gap and the number of conduction carriers do not change, thermal activation energy can be obtained from slope of Arrhenius plot.

$$\log_e \rho = \log_e \rho_0 + \frac{\Delta E}{T} \tag{34}$$

On the other hand, in systems where the thermal activation energy or carrier concentration changes, such as KI, the slope of Arrhenius plot is no longer constant. In this study, I differentiated the Arrhenius plot by $1/T$ and obtained the values at characteristic temperatures, which I define as thermally activated energy. Fig. 44 shows $log_e\rho$ differentiated by $1/T$ of YbB_{12}.

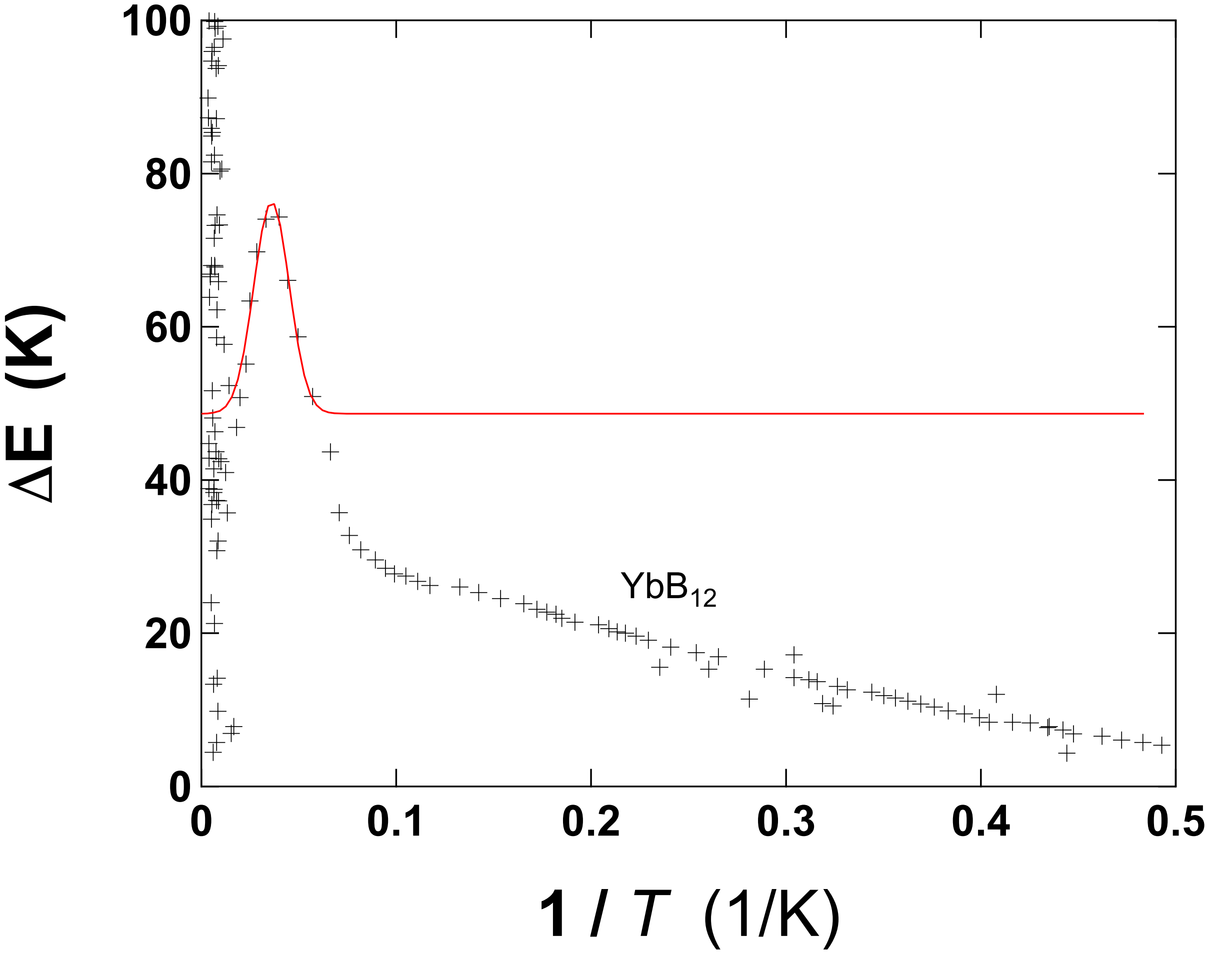

Fig.44: $log_e \rho$ of YbB_{12} differentiated by $1/T$.

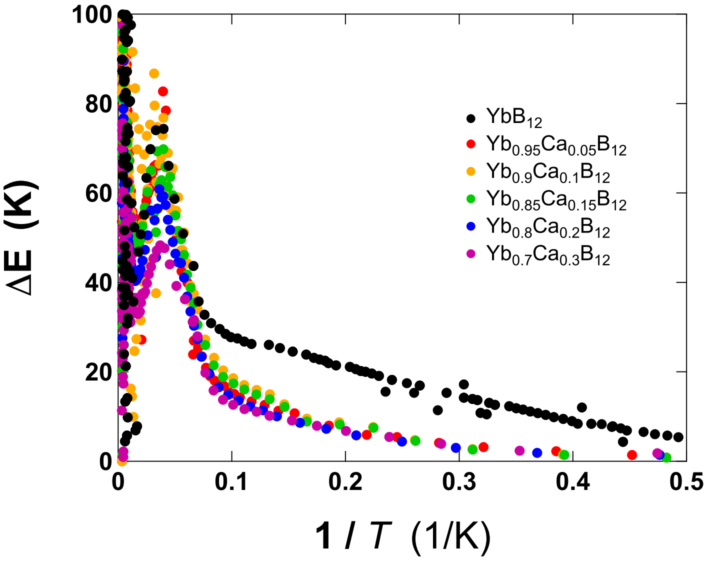

Fig.45: $log_e \rho$ of $Yb_{1-x}Ca_xB_{12}$ differentiated by $1/T$.

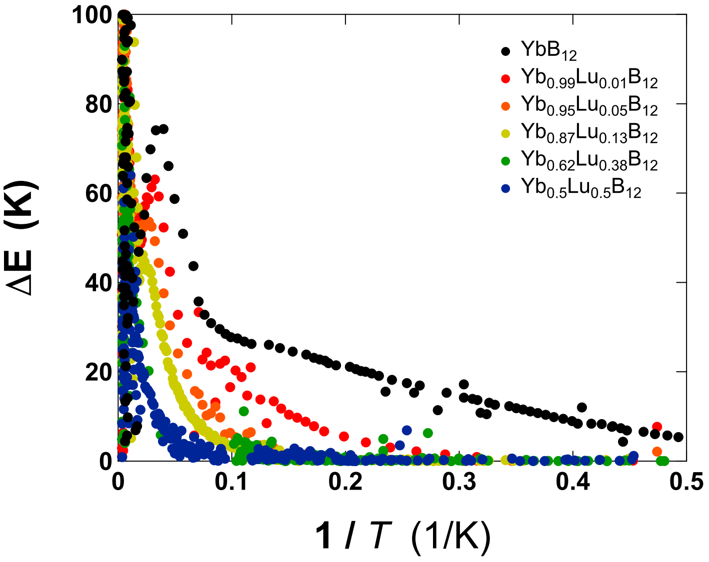

Fig.46: $log_e\rho$ of $\mathrm{Yb}_{1-x}\mathrm{Lu}_x\mathrm{B}_{12}$ differentiated by $1/T$.

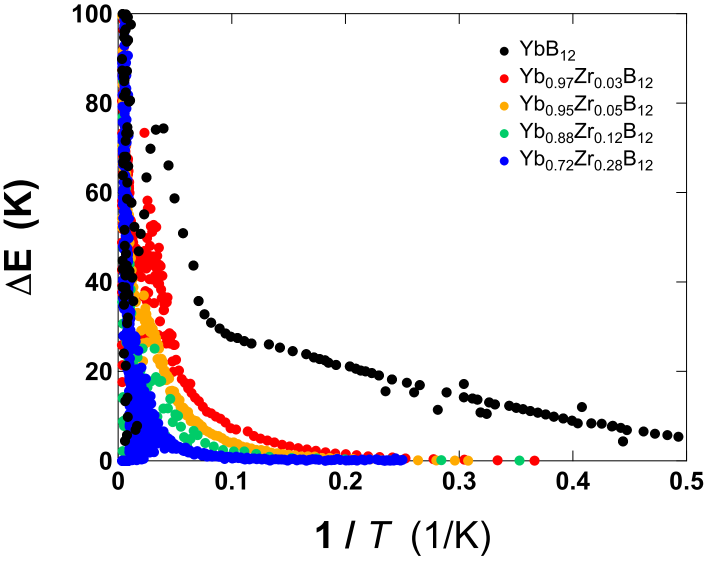

Fig.47: $log_e\rho$ of $\mathrm{Yb}_{1-x}\mathrm{Zr}_x\mathrm{B}_{12}$ differentiated by $1/T$.

By differentiating eq. 34, Fig. 44 shows the thermal activation energy divided by k_B. A clear peak appears near 33 K within ΔE_1^c dominant region ($T_0 < T$), with a peak value of 77 K, which is equal to the past ΔE_1^c value obtained from $\rho\,(T)$ and Hall resistivity $R_{\mathrm{H}}(T)$. The same derivation is applied to $\mathrm{Yb}_{1-x}\mathrm{R}_x\mathrm{B}_{12}$ (Figs. 45, 46, and 47) to obtain ΔE_1^c, as shown in Fig. 48.

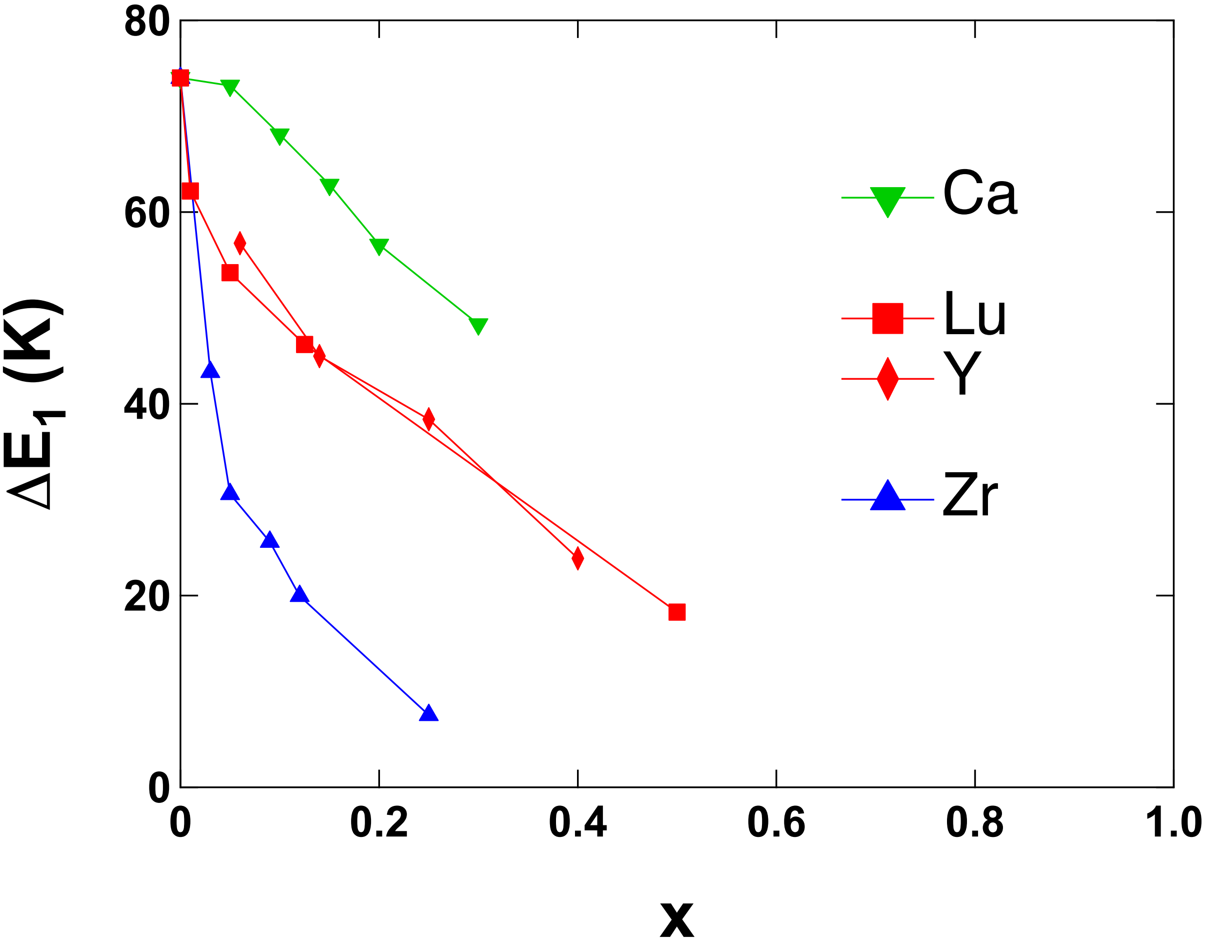

Fig.48: ΔE_1^c vs x obtained from $\rho\,(T)$.

The magnitude of ΔE_1^c varies with valence and shows a linearly decreasing behavior with increasing x. On the other hand, as shown in Fig. 44, $log_e \rho$ does not have a clear peak in the ΔE_2^c region with only a slight plateau near 6 K. Therefore, unlike ΔE_1^c, I plotted the value at 6 K as a function of x in each substitution system in Fig. 49.

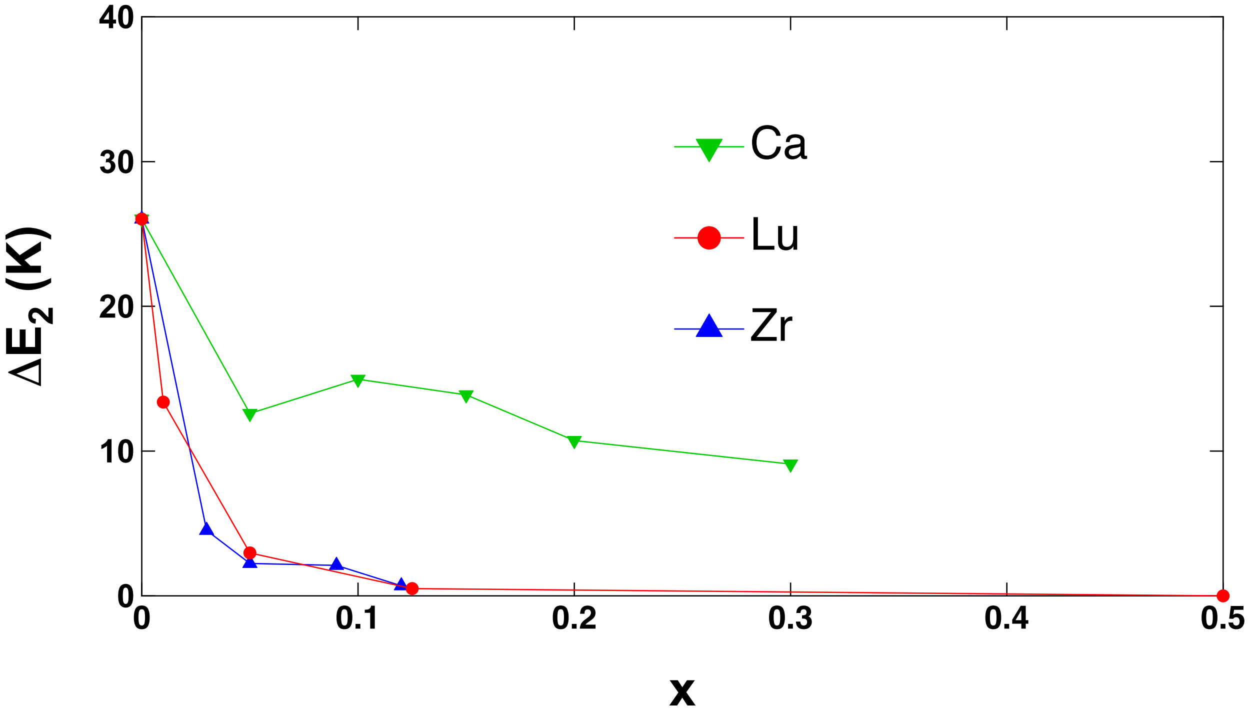

Fig.49: ΔE_2^c vs x obtained from $\rho\,(T)$.

ΔE_2^c obtained by the above method includes the temperature dependence of carrier concentration and mobility, and the substitution rate dependence below 15 K cannot be obtained accurately. For this reason, the following discussion will use the substitution rate dependence of the electrical conductivity $\sigma(2\text{ K})$ / $\sigma(300\text{ K})$.

The behavior of $\sigma(2\text{ K})$ / $\sigma(300\text{ K})$ for each substituted alloy, as shown in Fig. 50, is found to be fairly dependent on the valence of the substituted ion. This ratio up to $x = 0.05$ increases by two orders in magnitude for Ca, by more than three orders for Lu, and by four orders for Zr. On the other hand, for $x > x_0 = 0.1$, $\sigma(2\text{ K})$ / $\sigma(300\text{ K})$ gradually increases for all substituted alloys, regardless of change from semiconducting to metallic in the $x > 0.5$ region. To separate this x dependence of $\sigma(2\text{ K})$ / $\sigma(300\text{ K})$ into contributions of ΔE_1^c and ΔE_2^c, I have plotted the two ratios using bending temperature T_0 in Fig. 51. $\sigma(2\text{ K})$ / $\sigma(15\text{ K})$ [Fig. 51(a)] significantly increases up to $x = x_0$ and saturates at a constant value as x increases for $x > x_0$ for all alloys. Since the temperature region $T < 15$ K is ΔE_2^c-dominant, the x dependence of $\sigma(2\text{ K})$ / $\sigma(15\text{ K})$ is considered to be strongly related to the ΔE_2^c sensitivity to x. This narrow gap ΔE_2^c may collapse owing to the impurity band proposed by Schlottmann, in which the state near ϵ_F is induced by Kondo hole doping as seen for $\sigma(\omega, T)$. Hereafter, I refer to this impurity band as the Kondo impurity band (KIB). Moreover, $\sigma(15\text{ K})$ / $\sigma(300\text{ K})$ [Fig. 51(b)] increases proportionally to x, but each slope increases with the valence of the substituted ion. These increases in $\sigma(15\text{ K})$ / $\sigma(300\text{ K})$ may reflect the quantity of the conduction electrons doped by substituted ions.

The origin of the anomalous behavior of σ, χ, and C/T at low temperatures ($T < T_0$) in the region of $x < x_0$ can be explained by the DOS model in Fig. 52, which takes into account the formation of a KIB. The Kondo energy gap $Eg = 2k_B\Delta E_1 {=} k_BT_K$ should be formed between the lower band ($4f^{13}$ configuration) and ϵ_F owing to the contribution of the Kondo singlet and c-f hybridization. The upper band ($4f^{14}$ configuration), which is the $4f^{14}$ hole band, is located at an energy level slightly higher than ϵ_F. For $0 < x < x_0$ [Fig. 52(b)], a three-band system comprising the KIB and upper and lower band exists. For $x_0 < x < 0.5$ [Fig. 52(c)], the energy gap $2k_B\Delta E_2^c$ between the upper band and ϵ_F collapses with the spread of the KIB, resulting in a finite metallic DOS. Then, the decrease in Yb valence observed in Lu- and Zr-substituted alloys by HAXPES[61] can be explained by the elevation of ϵ_F to the upper band due to carrier doping in the KIB. Also the increases in C/T and χ at low temperatures, as respectively shown in Figs. 41 and 43, seem to be affected by the development of the KIB. In the Kondo lattice system, the enhancement of C/T and χ due to KIB formation near ϵ_F has been suggested by Mutou's numerical and analytical theories[52, 53]. Although numerical calculations suggest only enhancement, the peaks at x_0 for $C/T(2\text{ K})$ and $\chi(2\text{ K})$ seem to appear as a result of the enhancement and dilution of Yb as x increases. Therefore, these anomalous behaviors of σ, χ, and C/T in $\mathrm{Yb}_{1-x}\mathrm{R}_x\mathrm{B}_{12}$ below T_0 can be explained by this three-band model.

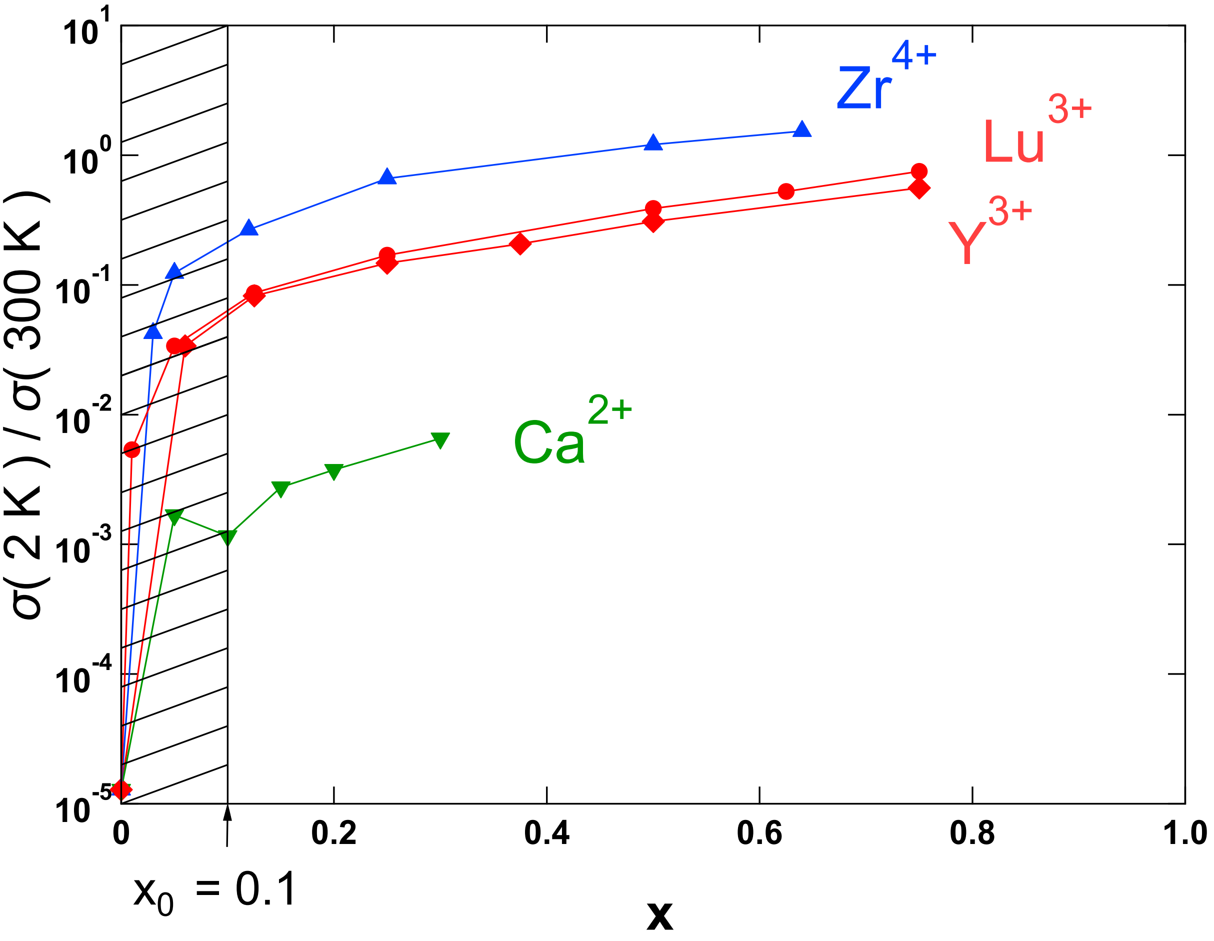

Fig.50: Logarithmic x dependence of $\sigma(2\,\mathrm{K})$ / $\sigma(300\,\mathrm{K})$ plotted for each sample to evaluate the nonmagnetic ion substitution effect on electrical conductivity, as well as those of $\chi(2\,\mathrm{K})$ and C/T (2 K). A steep increase was recognized for $x < x_0$ but this increase gradually becomes flat for $x > x_0$. The steep increase seems to correspond to the creation of the KIB state near ϵ_F.

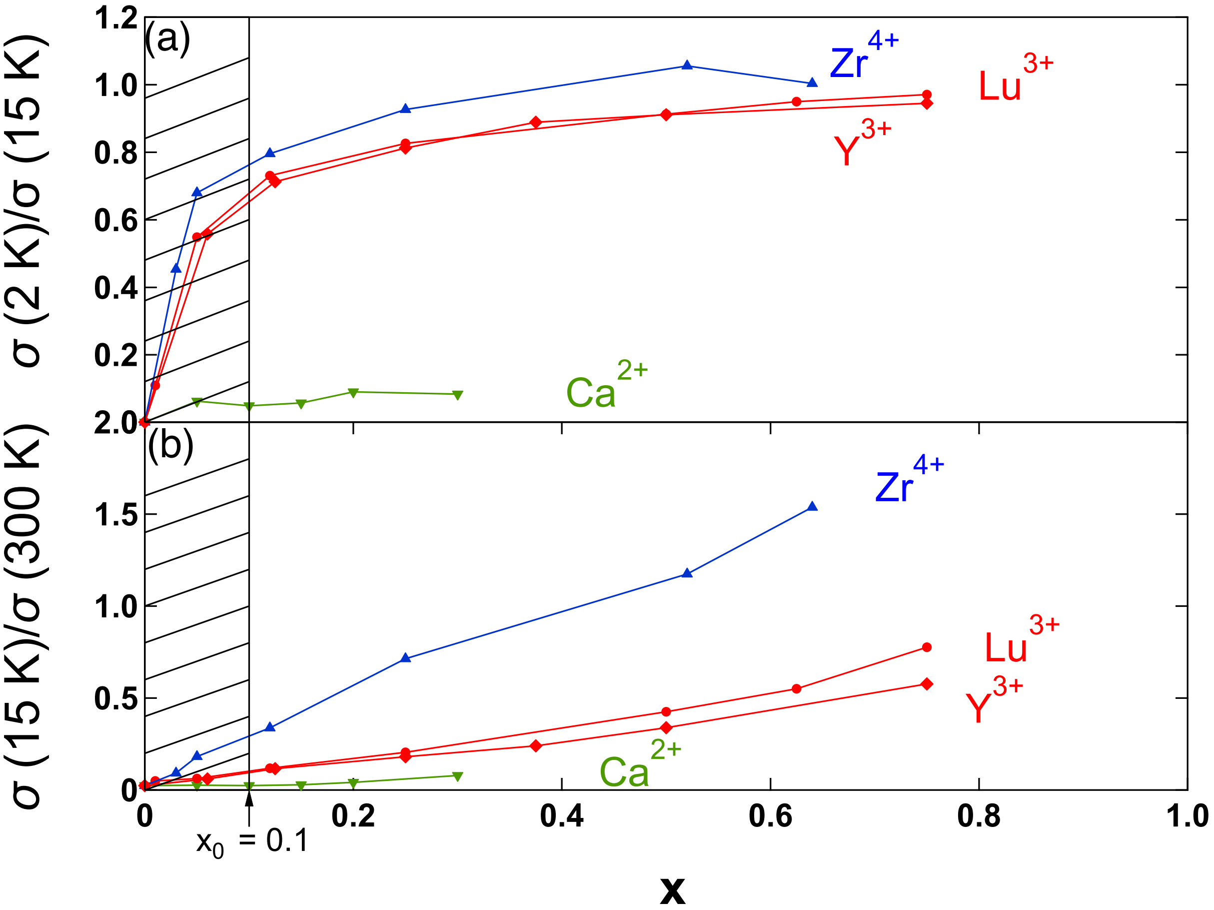

Fig.51: Ratios ($\sigma(2\,\mathrm{K})$ / $\sigma(15\,\mathrm{K})$ (a) and $\sigma(15\,K)$ / $\sigma(300\ \mathrm{K})$ (b)) plotted to evaluate the x dependence of ΔE_2^c and ΔE_1^c. The steep increase in $\sigma(2\,K)$ / $\sigma(300\ \mathrm{K})$ (Fig. 50) is due to the x dependence of $\sigma(2\,K)$ / $\sigma(15\ \mathrm{K})$ (a) (ΔE_2^c-dominant temperature region). On the other hand, $\sigma(15\,K)$ / $\sigma(300\ \mathrm{K})$ (b) is proportional to x and is continuous even near $x = 0.5$, where the conduction changes to metallic.

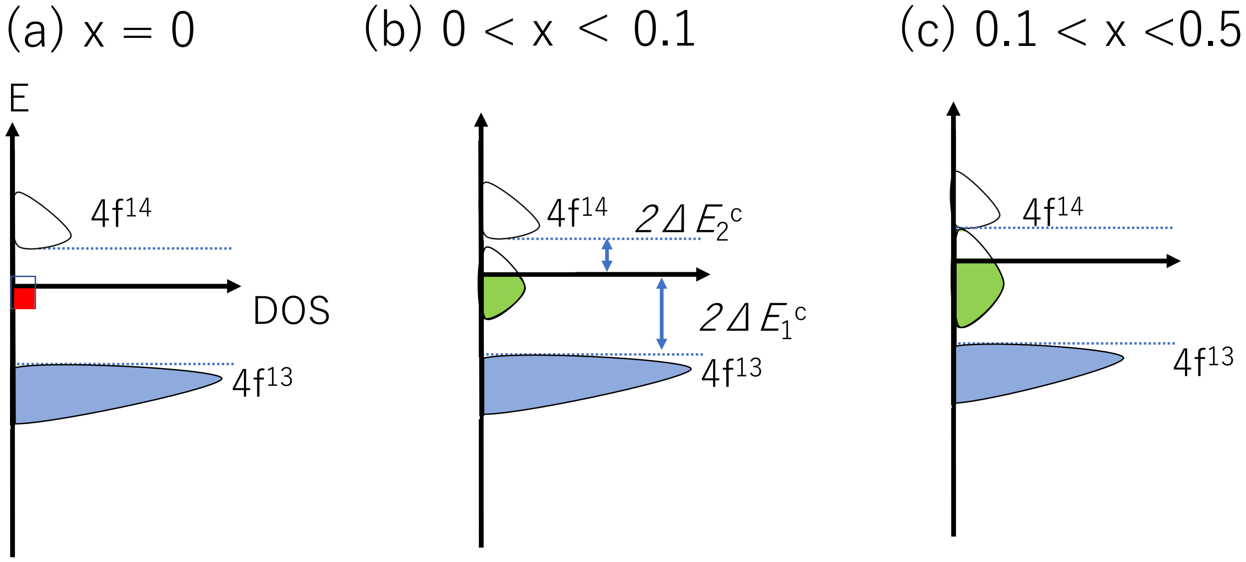

Fig.52: Schematic DOS model of $\mathrm{Yb}_{1-x}\mathrm{R}_x\mathrm{B}_{12}$ with Kondo impurity band (KIB). In (b) and (c), the KIB (green part) due to nonmagnetic ion substitution exists near ϵ_F. The two-step energy gap structure can be explained by three-band model (KIB, $4f^{13}$ and $4f^{14}$ bands). $2\Delta E_2^c$ is a narrow gap between the KIB and the $4f^{14}$ band. The growth of the KIB proportionally to x ($x > 0.5$) fills in $2\Delta E_1^c$ between the KIB and the $4f^{13}$ band. Even in YbB_{12}(a), the two-step energy gap structure can be explained by the existence of a defect-induced in-gap state (red part) that contributes to ρ (T) and the peak of ^{11}B NMR below 15 K.

6.2 Ground state of YbB_{12}

In the previous section, I proposed the two-step energy gap structure ΔE_1^c, ΔE_2^c of $\mathrm{Yb}_{1-x}\mathrm{R}_x\mathrm{B}_{12}$ based on a three-band model composed of the KIB and two $4f$ bands. All the semiconducting samples of $\mathrm{Yb}_{1-x}\mathrm{R}_x\mathrm{B}_{12}$ exhibit a thermally activated gap (ΔE_1^c), but also show KIB-derived conduction with ΔE_2^c for $x < x_0$. On the other hand, even in YbB_{12} without nonmagnetic impurities, there are many phenomena that cannot be explained without an in-gap state, such as convergent conduction below 3 K and the appearance of a 2D Fermi surface[44]. In the following, I will discuss the origin of the in-gap state of YbB_{12}. The NMR result of $^{11}\mathrm{B}$ in YbB_{12} shows a peak at $1/T_1$ vs T below 15 K but no peak at the $^{171}\mathrm{Yb}$ site[31], as mentioned in the introduction. This suggests that there is a relaxation process at an energy lower than the Kondo energy gap $Eg = k_B T_K$, such that there may be an in-gap state near ϵ_F even in pure YbB_{12}. This peak was also seen in the temperature dependence of the $^{11}\mathrm{B}$ site $1/T_1$ of $\mathrm{Yb}_{0.99}\mathrm{Lu}_{0.01}\mathrm{B}_{12}$[35], which has a KIB and ΔE_2^c as in Fig. 52(b). In addition, χ of polycrystalline $\mathrm{Yb}_{1-x}\mathrm{Ca}_x\mathrm{B}_{12}$ is more enhanced than that of single-crystal $\mathrm{Yb}_{1-x}\mathrm{R}_x\mathrm{B}_{12}$ (R = Lu and Zr), suggesting that inhomogeneity[31] and defects[35] also enhance χ. The enhancement of χ at low temperatures seen in $\mathrm{Yb}_{1-x}\mathrm{R}_x\mathrm{B}_{12}$ is also seen in polycrystalline and powdered single-crystal YbB_{12}. From the above consideration, the induced in-gap state should appear with a small amount of impurity, inhomogeneity, or defects.

A remaining question regarding the in-gap state in YbB_{12} is whether this state contributes to quantum oscillation (QO). The reported consistency in the frequency and mass near the boundary field of the IM transition suggests that the same Fermi surface pockets contribute to the QO in both the magnetic-field-induced KM and KI phases [50]. On the other hand, in the KI phase, its frequency and mass are independent of the magnetic field. From the experimental result, I hypothesize that an in-gap state pinned near ϵ_{F} with no spin component may contribute to QO. At present, it is unclear how the defect-induced in-gap state is related to the origin of this QO, in addition to TSS, which should be investigated in more detail.

7 Conclusion

I have investigated nonmagnetic ion substitution effect by measurements of electrical conductivity σ, specific heat divided by temperature C/T, and magnetic susceptibility χ in the Kondo insulator alloys $\mathrm{Yb}_{1-x}\mathrm{R}_x\mathrm{B}_{12}$ ($\mathrm{R} = \mathrm{Ca}^{2+}$, Lu^{3+}, Y^{3+}, and Zr^{4+}). The x dependence of $\sigma(T)$ in the ΔE_1^c- and ΔE_2^c-dominant temperature regions shows that ΔE_1^c is x-insensitive gap and that ΔE_2^c is x-sensitive narrow gap. C/T and χ below 20 K show a maximum enhancement at $x_0 = 0.1$. The enhancement of C/T and χ at $x < x_0$ is qualitatively consistent with that obtained by Mutou's calculation. The x-dependence of $\sigma(2\,\mathrm{K})$ / $\sigma(15\,\mathrm{K})$ also indicates that x_0 is the critical boundary x where ΔE_2^c disappears for all the substituted alloys. On the basis of Schlottmann's impurity model involving Kondo holes, I proposed a three-band model with a Kondo impurity band (KIB) in $\mathrm{Yb}_{1-x}\mathrm{R}_x\mathrm{B}_{12}$ that can explain the x dependence of $\sigma(T)$. The maximum enhancement of C/T and χ at around x_0 is also explained by the growth of the KIB and Yb dilution. Even in YbB_{12}, however, where there is no impurity band due to substitution, the two-step energy gap structure exists. NMR results of YbB_{12} suggest that the enhancement of $1/T_1$ at the $^{11}\mathrm{B}$ site is caused by small amounts of impurities and defects at the Yb site and the inhomogeneity of the sample. Therefore, the three-band model can also be applied to YbB_{12}, supposing that the impurity band is similar to the KIB in the alloy $\mathrm{Yb}_{1-x}\mathrm{R}_x\mathrm{B}_{12}$.

References

[1] Kazuo Ueda, Yoshichika Onuki, *"Omoi denshikei no butsuri"* [Physics of heavy fermion systems] , (*"Shoukabou"*, 1998).

[2] P. W. Anderson, Phys. Rev. **124**, 41 (1961).

[3] J. Kondo, Prog. Theor. Phys. **32**, 37 (1964).

[4] K. Yosida, Phys. Rev. **147**, 223 (1966).

[5] P. W. Anderson, J. Phys. **C3**, 2436 (1970).

[6] K. G. Wilson, Rev. Mod. Phys. **47**, 773 (1975).

[7] A. Sumiyama, Y. Oda, H. Nagano, Y. Onuki, K. Shibutani and T. Komatsubara, J. Phys. Soc. Jpn. **55**, 1294 (1985).

[8] G. R. Stewart, Z. Fisk, J. O. Willis, and J. L. Smith, Phys. Rev. Lett. **52**, 679 (1984).

[9] A. Ler. Dawson, W. R. Datars, J. D. Garrett, and F. S. Razavi, J. Phys.: Condens. Matter **1**, 6817 (1989).

[10] A. Takase, K. Kojima, T. Komatsubara, and T. Kasuya, Solid State Commun. **36**, 461 (1980).

[11] P. Gegenwart, C. Langhammer, C. Geibei, R. Helfrich, M. Lang, G. Sparn, F. Steglich, R. Horn, L. Donnevert, A. Link, and W. Assmus, Phys. Rev. Lett. **81**, 1501 (1998).

[12] J. W. Allen, S. J. Oh, M. B. Maple, and M. S. Torikachvili, Phys. Rev. B **28**, 5347 (1983).

[13] S. Doniach Physica **91B**, 231 (1977).

[14] A. Menth, E. Buehler, and T. H. Geballe, Phys. Rev. Lett. **22**, 295 (1969).

[15] M. Kasaya, F. Iga, K. Negishi, S. Nakai, and T. Kasuya, J. Magn. Magn. Matter. **31-34**, 437 (1983).

[16] H. Okamura, S. Kimura, H. Shinozaki, T. Nanba, F. Iga, N. Shimizu, and T. Takabatake, Physica B **259-261**, 317 (1999).

[17] F. Iga, Y. Takakuwa, T. Takahashi, M. Kasaya, T. Kasuya, and

T. Sagawa, Solid State Commun. **50**, 903 (1984).

[18] M. Kasaya, F. Iga, M. Takigawa, and T. Kasuya, J. Magn. Magn. Mater. **47-48**, 429 (1985).

[19] T. Kasuya, K. Takegahara, T. Fujita, T. Tanaka, and E. Bannai, J. Phys. Colloq. **40**, C5-308 (1979).

[20] T. Kasuya, Europhys. Lett. **26**, 277 (1994).

[21] T. Saso and H. Harima, J. Phys. Soc. Jpn. **72**, 1131 (2003).

[22] N. F. Mott, Philos. Mag. **30**, 403 (1974).

[23] F. Iga, N. Shimizu, and T. Takabatake, J. Magn. Magn. Mater. **177-181**, 337 (1998).

[24] T. Susaki, A. Sekiyama, K. Kobayashi, T. Mizokawa, A. Fujimori, M. Tsunekawa, T. Muro, T. Matsushita, S. Suga, H. Ishii, T. Hanyu, A. Kimura, H. Namatame, M. Taniguchi, T. Miyahara, F. Iga, M. Kasaya, and H. Harima, Phys. Rev. Lett. **77**, 4269 (1996).

[25] T. Susaki, Y. Takeda, M. Arita, K. Mamiya, A. Fujimori, K. Shimada, H. Namatame, M. Taniguchi, N. Shimizu, F. Iga, and T. Kasuya, Phys. Rev. Lett. **82**, 992 (1999).

[26] E. Nefeodova, P. Alekseev, J.-M. Mignot, V. Lazukov, I. Sadikov, Y. B. Paderno, N. Y. Shitsevalova, and R. Eccleston, Phys. Rev. B **60**, 13507 (1999).

[27] F. Iga, A. Bouvet, L. Regnault, T. Takabatake, A. Hiess, and T. Kasuya, J. Phys. Chem. Solids **60**, 1193 (1999).

[28] P. A. Alekseev, J.-M. Mignot, K. S. Nemkovski, E. V. Nefeodova, N. Y. Shitsevalova, Y. B. Paderno, R. I. Bewley, R. S. Eccleston, E. S. Clementyev, V. N. Lazukov, I. P. Sadikov, and N. N. Tiden, . Phys.: Condens. Matter **16**, 2631 (2004).

[29] J. M. Mignot, P. A. Alekseev, K. Nemkovski, L.-P. Regnault, F. Iga, and T. Takabatake, Phys. Rev. Lett. **94**, 247204 (2005).

[30] K. Nemkovski, J.-M. Mignot, P. Alekseev, A. Ivanov, E. Nefeodova, A. Rybina, L.-P. Regnault, F. Iga, and T. Takabatake, Phys. Rev. Lett. **99**, 137204 (2007).

[31] K. Ikushima, Y. Kato, M. Takigawa, F. Iga, S. Hiura, and T. Takabatake, Physica B **281-282**, 274 (2000).

[32] K. Sugiyama, F. Iga, M. Kasuya, T. Kasuya, and M. Date, J. Phys. Soc. Jpn. **57**, 3946 (1988).

[33] F. Iga, K. Suga, K. Takeda, S. Michimura, K. Murakami, T. Takabatake, and K. Kindo, J. Phys.: Conf. Ser. **200**, 012064 (2010).

[34] T. T. Terashima, A. Ikeda, Y. H. Matsuda, A. Kondo, K. Kindo, and F. Iga, J. Phys. Soc. Jpn. **86**, 054710 (2017).

[35] N. Shishiuchi, Y. Koto, O. M. Vyaselev, M. Takigawa, S. Hiura, F. Iga, and T. Takabatake, J. Phys. Chem. Solids **63**, 1231 (2002).

[36] T. Kasuya, M. Kasaya, K. Takegahara, F. Iga, B. Liu, and N. Kobayashi, J. Less-Common Met. **127**, 337 (1987).

[37] T. Saso and H. Harima J. Phys. Soc. Jpn. **72**, 1131 (2002).

[38] F. Lu, J. Zhao, H. Weng, Z. Fang, and X. Dai, Phys. Rev. Lett. **110**, 096401 (2013).

[39] V. Alexandrov, M. Dzero, and P. Coleman, Phys. Rev. Lett. **111**, 226403 (2013).

[40] H. Weng, J. Zhao, Z. Wang, Z. Fang, and X. Dai, Phys. Rev. Lett. **112**, 016403 (2014).

[41] J. C. Y. Teo, L. Fu, and C. L. Kane, Phys. Rev. B **78**, 04526 (2008).

[42] P. Syers, D. Kim, M. S. Fuhrer, and J. Paglione, Phys. Rev. Lett. **114**, 096601 (2015).

[43] N. Xu, P. K. Biswas, J. H. Dil, R. S. Dhaka, G. Landolt, S. Muff, C. E. Matt, X. Shi, N. C. Plumb, M. Radović, E. Pomjakushina, K. Conder, A. Amato, S. V. Borisenko, R. Yu, H. M. Weng, Z. Fang, X. Dai, J. Mesot, H. Ding, and M. Shi, Nat. Commun. **5**, 4566 (2014).

[44] K. Hagiwara, Y. Ohtsubo, M. Matsunami, S. Ideta, K. Tanaka, H. Miyazaki, J. E. Rault, P. Le Févre, F. Bertran, A. Taleb-Ibrahimi, R. Yukawa, M. Kobayashi, K. Horiba, H. Kumigashira, K. Sumida,

T. Okuda, F. Iga, and S. Kimura, Nat. Commun. **7**, 12690 (2016).

[45] G. Li, Z. Xiang, F. Yu, T. Asaba, B. Lawson, P. Cai, C. Tinsman, A. Berkley, S. Wolgast, Y. S. Eo, D. J. Kim, C. Kurdak, J. W. Allen, K. Sun, X. H. Chen, Y. Y. Wang, Z. Fisk, and L. Li, Science **346**, 1208 (2014).

[46] B. S. Tan, Y. T. Hsu, B. Zeng, M. C. Hatnean, N. Harrison, Z. Zhu, M. Hartstein, M. Kiourlappou, A. Srivastava, M. D. Johannes, T. P. Murphy, J. H. Park, L. Balicas, G. G. Lonzarich, G. Balakrishnan, and S. E. Sebastian, Science **349**, 287 (2015).

[47] H. Liu, M. Hartstein, G. J. Wallace, A. J. Davies, M, C. Hatnean, M. D. Johannes, N. Shitsevalova, G. Balakrishman, and S. E. Sebastian, J. Phys.: Condens. Matter **30**, 16LT01 (2018).

[48] Z. Xiang, Y. Kasahara, T. Asaba, B. Lawson, C. Tinsman, L. Chen, K. Sugimoto, S. Kawaguchi, Y. Sato, G. Li, S. Yao, Y. L. Chen, F. Iga, J. Singleton, Y. Matsuda, and L. Li, Science **362**, 65 (2018).

[49] Y. Sato, Z. Xiang, Y. Kasahara, T. Taniguchi, S. Kasahara, L. Chen, T. Asaba, C. Tinsman, H. Murayama, O. Tanaka, Y. Mizukami, T. Shibauchi, F. Iga, J. Singleton, L. Li, and Y. Matsuda, Nat. Phys. **15**, 954 (2019).

[50] Z. Xiang, L. Chen, K. Chen, C. Tinsman, Y. Sato, T. Asaba, H. Lu, Y. Kasahara, M. Jaime, F. Balakirev, F. Iga, Y. Matsuda, J. Singleton, and L. Li, Nat. Phys. **17**, 788 (2021).

[51] P. Schlottmann, Phys. Rev. B **46**, 998 (1992).

[52] T. Mutou, Phys. Rev. B **62**, 15589 (2000).

[53] T. Mutou, Phys. Rev. B **64**, 165103 (2001).

[54] F. Iga, M. Kasaya, and T. Kasuya, J. Magn. Magn. Mater. **52**, 279 (1985).

[55] F. Iga, S. Hiura, J. Klijn, N. Shimizu, T. Takabatake, M. Ito, Y. Matsumoto, F. Masaki, T. Suzuki, and T. Fujita, Physica B **259-261**, 312 (1999).

[56] F. Iga, M. Kasaya, and T. Kasuya, J. Magn. Magn. Mater. **76-77**, 156 (1988).

[57] H. Okamura, T. Inaoka, S. Kimura, T. Nanba, F. Iga, S. Hiura, J. Kleijn, and T. Takabatake, Physica B **281-282**, 280 (2000).

[58] H. Okamura, M. Matsunami, T. Inaoka, T. Nanba, S. Kimura, F. Iga, S. Hiura, J. Klijn, and T. Takabatake, Phys. Rev. B **62**, R13265(R) (2000).

[59] K. Hayashi, K. Ishii, F. Iga, T. Noguchi, T. Takabatake, A. Kondo, and K. Kindo, JPS Conf. Proc. **3**, 011050 (2014).

[60] F. Iga, K. Yokomichi, W. Matsuhra, H. Nakayama, A. Kondo, K. Kindo, and H. Yoshizawa, AIP Adv. **8**, 101335 (2018).

[61] A. Rousuli, H. Sato, F. Iga, K. Hayashi, K. Ishii, T. Wada, T. Nagasaki, K. Mimura, H. Anzai, K. Ichiki, S. Ueda, A. Kondo, K. Kindo, T. Takabatake, K. Shimada, H. Namatame, and M. Taniguchi, J. Phys.: Condens. Matter **29**, 265601 (2007).

[62] V. T. Rajan, Phys. Rev. Lett. **51**, 308 (1983).

Published works

(1) Wataru Matsuhra, Naoki Takahashi, Kensuke Yamada, Mizuto Kadowaki, and Fumitoshi Iga,

"Development of In-Gap State and Related Collapse of Two-Step Energy Gap Structure by Nonmagnetic Ion Substitution in Kondo Insulator YbB_{12}",

Journal of the Physical Society of Japan, **90**, 124705 (2021).

(2) W. Matsuhra, K. Yokomichi, W. Hirano, S. Kikuchi, N. Uematsu, H. Nakayama, A. Kondo, K. Kindo, and F. Iga,

"Divalent ion substitution effect on Yb-site in Kondo insulator YbB_{12}", AIP Advances, **8**, 101329 (2018).

(3) F. Iga, K. Yokomichi, W. Matsuhra, H. Nakayama, A. Kondo, K. Kindo, and H. Yoshizawa,

"Non-magnetic element substitution effect in Kondo insulator YbB_{12} and exotic surface effect in this alloy system",

AIP Advances, **8**, 101335 (2018).

(4) S. Uechi, K. Ohoyama, Y. Fukumoto, Y. Kanazawa, N. Happo, M. Harada, Y. Inamura, K. Oikawa, W. Matsuhra, F. Iga, A. K. R. Ang, and K. Hayashi,

"Behavior of Sm in the boron-cage of Sm-doped RB_6 (R=Yb,La) observed by multiple-wavelength neutron holography",

Phys. Rev. B **102**, 054104 (2020).

Acknowledgements

This research has been made possible by cooperation of many people, and I would like to thank them for their assistance. First of all, I would like to express my sincere gratitude to my supervisor, Professor Fumitoshi Iga. Prof. Iga has been my mentor for six years since I was assigned to his laboratory. He taught me many things, including knowledge of condensed matter physics, guidance on equipment and methods for sample preparation using TSFZ method and high-pressure synthesis, and skills in logical thinking. Prof. Iga gave me many important life skills. I would like to express gratitude to him again.

I would like to thank Prof. Keitaro Kuwahara, Prof. Makoto Yokoyama, Prof. Chihiro Sekine, and Associate Prof. Takehito Nakano for teaching me research methods and basic knowledge about experiments.

Dr. Nobumasa Nishiyama, formerly of Tokyo Institute of Technology, taught me the basic techniques and essence of the experiments of high-pressure synthesis. I would like to express my sincere gratitude to him.

I am grateful to the facilities of the institute for solid state physics (ISSP) of the University of Tokyo for electrical resistivity, magnetic susceptibility, and specific heat measurements. I would like to express my sincere gratitude to Prof. Koichi Kanamichi and Prof. Akira Matsuo of Kanamichi Lab. I am also grateful to Dr. Akihiro Kondo, who taught us how to use PPMS and MPMS.

I would like to express my sincere thanks to Prof. Yoshiaki Hara of Ibaraki College of Technology for his cooperation in taking Laue photographs for the evaluation of crystallinity. I am deeply grateful to him.

I am deeply grateful to senior members of Iga laboratory who prepared some of the samples used in the research and allowed me to use them for the measurements. I would also like to express my gratitude to the junior

members of the Iga and Nakano laboratories for their help in managing the laboratory. I would like to express my gratitude to them.

Finally, I would like to express my gratitude to my family, including my grandparents, for their support my research life.